Indentation Size Effect: Analysis of Underlying Mechanisms in (001) oriented Strontium Titanate Single Crystal via Chemical Etching and EBSD

Vom Fachbereich Material- und Geowissenschaften

der Technischen Universität Darmstadt

zur Erlangung des Grades

eines Doktors der Ingenieurwissenschaften

(Dr.-Ing.)

genehmigte Dissertation von

Farhan Javaid, M.Sc.

aus Lahore, Pakistan

Hauptberichterstatter: Prof. Dr. Karsten Durst

Nebenberichterstatter: Prof. Dr. Jürgen Rödel

Tag der Einreichung: 13.02.2017

Tag der mündlichen Prüfung: 16.03.2017

Darmstadt 2017

D17

„Gedruckt mit Unterstützung des Deutschen Akademischen Austauschdienstes“

Erklärung zur Dissertation

Hiermit versichere ich, die vorliegende Dissertation ohne Hilfe Dritter nur mit den angegebenen Quellen und Hilfsmitteln angefertigt zu haben. Alle Stellen, die aus Quellen entnommen wurden, sind als solche kenntlich gemacht. Diese Arbeit hat in gleicher oder ähnlicher Form noch keiner Prüfungsbehörde vorgelegn.

Darmstadt, den 13 Februar 2017

_____

Farhan Javaid

Acknowledgements

First of all, I would like to express my deepest gratitude to my mentor **Prof. Dr. Karsten Durst**, *Head of Physical Metallurgy Department, Institute of Materials Science, TU Darmstadt,* for giving me an opportunity to work as a Ph.D. candidate under his supervision and suggesting the idea of this project. Without his kind encouragement and creative support, it would not have been possible to accomplish this great task. It is a great honor to work under his supervision. I would also like to thank my other committee members for their time and inputs.

During the course of this work, I was financially supported by the **Deutscher Akademischer Austauschdienst** (DAAD), Bonn, Germany. I would like to express my special thanks to DAAD for all financial support.

I would like to express my deepest thanks to **Dr. Enrico Bruder, Dr. Hamad-ur-Rehman** and **Dr. Kurt E. Johanns**, for helpful technical discussions and valuable advices on the several occasions. I would also like to thank **Dr. Alexander Stukowski** of *Material Modelling Division, TU Darmstadt,* for conducting MD simulations and **Dr. Eric Patterson** of *NAW, TU Darmstadt,* for providing the STO single crystals.

I am extremely thankful to all of my **colleagues** from *PhM, TU Darmstadt,* for creating a great friendly working environment, their technical support and helps over the year.

Finally, I owe a deep sense of gratitude to **my parents** and **wife**, for their constant encouragement throughout my research period, especially when nothing seems to work.

Abstract

Many crystalline materials exhibit an indentation size effect (ISE), i.e., an intrinsic increase in hardness with decreasing indentation depths during indentation with geometrically self-similar indenters such as pyramids and cone. During indentation testing, the material underneath the indenter is heavily deformed, introducing strain gradients in the materials, causing high local dislocation densities. For better understanding the small-scale mechanical properties, in the present work, the 3D dislocation structure evolution around and underneath the spherical and Berkovich indentations have been resolved for the first time in (001) oriented strontium titanate (STO) single crystal at room temperature via a Sequential Polishing and Etching Technique (SPET). The Scanning Electron Microscopy (SEM) and Electron Back Scatter Diffraction (EBSD) were used to analyze the dislocation microstructures at various depths below the surface.

The indentation data combined with dislocation etch-pit technique revealed that the incipient plasticity (manifested as sudden indenter displacement burst) was strongly influenced by pre-existing dislocations. Etching revealed a well-defined asterisk-shaped etch-pit symmetry around the residual impressions, aligned along the <100> and <110> directions, which evolved step-by-step by increasing indentation load. SPET obtained cross-sections confirmed the presence of a high dislocation density region below the indentations. At larger polishing depths, a dislocation free region surrounded by box-shaped dislocation etch-pits pattern was observed. From dislocation etch-pits shape and tracking of dislocation etch-pit pile-ups, it was found that the slip along {110} planes is more favorable underneath the indentations.

The dislocation etch-pits were digitized for calculating the dislocation densities at multiple depths with subsequent high-resolution electron backscatter diffraction (HR–EBSD) measurements at each polishing depth. The dislocation density quantified from etch-pit analysis includes both Statistically Stored Dislocations (SSDs) and (Geometrically Necessary Dislocations) GNDs, whereas HR-EBSD provides only the minimum GND density necessary to generate the measured orientation distribution. Both HR-EBSD and etch pit analysis show

for each normalized radius a higher dislocation density at smaller loads. This result qualitatively validates the assumption in the Nix-Gao model that lower indentation depths result in higher GND densities.

Furthermore, elevated temperature (350 °C) Berkovich nanoindentation experiments were performed on (001) oriented STO to analyze the influence of temperature on the ISE and the dislocation structure around the residual impression. It was found that STO exhibits an ISE, which was strongly reduced at 350 °C compared to 25 °C. At 25 °C, dislocation pile-ups were found shorter as compared to 350 °C. This also correlates with the smaller size effects at 350 °C. Peach-Koehler forces and the elastic-plastic indentation stress field were used to model the influence of the lattice frictional stress on the dislocation pile-ups. Based on an equilibrium position of the outermost dislocations, an average lattice frictional stresses were calculated to be 89 MPa and 46 MPa at 25 °C and 350 °C, respectively.

Table of Contents

List of Acronyms

Abbreviation	Description
AFM	Atomic Force Microscopy
APB	Anti-Phase Boundary
BCC	Body Centered Cubic
CMSG	Conventional Mechanisms-based Strain Gradient
CPFEM	Crystal Plasticity Finite Element Modeling
CSM	Continuous Stiffness Measurement
DBDT	Ductile-to-Brittle-to-Ductile Transition
EBSD	Electron Back Scatter Diffraction
ECCI	Electron Channeling Contrast Imaging
FCC	Face Centered Cubic
FIB	Focused Ion Beam
GB	Grain Boundary
GNDs	Geometrically Necessary Dislocations
HR-EBSD	High Resolution Electron Back Scatter Diffraction
ISE	Indentation Size Effect
KAM	Kernel Average Misorientation
LC	Load Control
LD	Load Displacement
MAE	Mean Angular Error

Abbreviation	Description
MD	Molecular Dynamics
PID	Proportional Integral Differential
RFDA	Resonant Frequency and Damping Amplifier
ROI	Region of Interest
SC	Simple Cubic
SEM	Scanning Electron Microscopy
SPET	Sequential Polishing and Etching Technique
SSDs	Statistically Stored Dislocations
STO	Strontium Titanate
TEM	Transmission Electron Microscopy

List of Symbols

Symbol	Description
P	Applied load
τ_a	Applied shear stress
b	Burgers vector
h^*	Characteristic indentation length scale
h_c	Contact depth
a	Contact radius
S	Contact stiffness
τ_o	Critical resolved shear stress
ε_o	Dielectric constant
ρ	Dislocation density
τ_d	Dislocation-dislocation interaction shear stresses
σ	Flow stress
τ_{fr}	Fracture stress
K_{IC}	Fracture toughness
τ_{im}	Image shear stresses
h	Indentation depth
τ_f	Lattice frictional stress
H_o	Macroscopic hardness

Symbol	Description
P_{max}	Maximum applied load
h_{max}	Maximum indentation depth
τ_{max}	Maximum shear stress
ν	Poisson's ratio
$P_{pop\text{-}in}$	Pop-in load
A	Projected area of contact at maximum load
r	Radial distance from the center of the indent to dislocation position
F	Scaling factor
f	Storage volume of the geometrically necessary dislocations
$3D$	Three-dimensional
R	Tip radius
T	Temperature
E	Young's Modulus

List of Figures

List of Tables

Chapter 1 Introduction

Strontium titanate ($SrTiO_3$), henceforth referred to as STO, is an optically transparent perovskite oxide ceramic material, which has been studied for decades because of its remarkable properties, like high dielectric constant, high chemical and thermal stability [1-2]. These noteworthy properties make STO a prime candidate for different technological applications include the following: as a substrate for wide range of materials including high-temperature superconductors [3], dielectric materials in capacitors, for producing different microelectronic hetero-structures [1], as anodes in fuel cells [4]. Recently, it has been demonstrated that dislocations can have a strong effect on the electrical properties of ceramic materials [5-6]. Inducing dislocations by plastic deformation can potentially provide a strategy to modify the charge carrier transport and / or ionic surface exchange kinetics in solid oxides [7-8]. In the case of STO, which is a prototypical perovskite oxide ceramic [9], the transport of oxygen along dislocations is a current center of attention [10-11] due to its potential implementation as resistive switching memory [12-13]. The dislocations are believed to act as nanoscale filamentary paths for transport of oxygen ions, more rapidly than the regular STO lattice [13-15]. Exploiting such effects in technological applications, thus requires a sound understanding of dislocation behavior at all length scales.

The mechanical behavior of STO has been studied extensively using uniaxial compression testing techniques for a wide range of temperature regimes due to its exceptional stable cubic symmetry above 105.5 K [16-18]. In contrast to other ceramics, single crystal STO can be plastically deformed under ambient condition up to a maximum plastic strain of 9% and shows an unusual ductile-to-brittle-to-ductile (DBDT) transition, irrespective of compression axis orientation [18-20]. This DBDT transition is divided into three regimes (A, B and C) corresponding to the temperature range of ~113 – 1053 K, ~1053 – 1503 K and ~1503 – 1873 K [21]. Taeri et al. [22] reported that for the <100> compression axes, slip occurs along $\langle 110 \rangle \{110\}$ system at low and high temperatures. However, for compression axis other than <100>, slip occurs along $\langle 110 \rangle \{110\}$ system at low temperatures, whereas, at high temperatures $\langle 100 \rangle \{110\}$ system dominates. Recently, Patterson et al. [23] reported the temperature dependence of dislocation density in (001) STO single crystal during uniaxial compression testing using ex-situ X-ray diffraction rocking curve technique.

In contrast to these comprehensive bulk single crystal plasticity behaviors of STO, studied via uniaxial compression testing, little is known about the small-scale behavior in this perovskite material. Matsunaga et al. [24] conducted Vickers micro-indentations using ~500 mN in (001) STO single crystal at room temperature and identified <110>{110} slip system. Later on, Yang et al. [25] performed Vickers micro-indentations on STO (001) single crystal and reported a secondary slip system, $\langle 110\rangle\{001\}$ in addition to the primary $\langle 110\rangle\{1\bar{1}0\}$ system, which is typically active during uniaxial compression testing. Recently, Kondo et al. [26] reported only $\langle 110\rangle\{1\bar{1}0\}$ type slip system during in-situ Transmission Electron Microscopy (TEM) nanoindentation experiments in (001) STO single crystal. Such discrepancies show that our knowledge of dislocation structure evolution at small scales and details of dislocation based nanoplasticity in this perovskite material is still very limited. Since STO is considered as a model system to study extended defect structures in perovskite oxide materials and their effect on the ionic and electronic transport properties, a comprehensive analysis of dislocation structure at the local-scale is necessary. Such analyses are potentially interesting for tailoring the local ionic conductivity and to study the phenomenon like indentation size effect (ISE), which is more pronounced at the local-scale and still missing in the literature.

Nanoindentation in conjunction with advanced characterization techniques like Scanning Electron Microcopy (SEM) based techniques including Electron Back Scattered Diffraction (EBSD) and Electron Channeling Contrast Imaging (ECCI), Atomic Force Microscopy (AFM) and TEM, emerged as powerful tools to study the small-scale deformation mechanisms in a variety of materials. For example, Durst et al. [27] quantified the dislocation etch-pits for different indentation loads using AFM and studied the ISE behavior in the CaF_2 single crystal. Bahr et al. [28] applied chemical etching technique on Tungsten single crystal to examine the onset of plasticity during nanoindentation as a function of pre-existing dislocation densities by using Vickers indentation. Tromas et al. [29] used a similar etching technique along with AFM to study the dislocation structure and the effect of pre-existing dislocations on incipient plasticity in (001) MgO single crystal. ECCI also proves to be an ideal nondestructive technique for revealing and quantification of dislocation structure in bulk and at the local-scale. Kamaladasa et al. [30] implemented the ECCI to analyze the extended defects such as dislocation loops and sub-surface dislocations parallel to the surface in bulk (001) oriented STO. Kumar et al. [31] used ECCI to analyze the dislocation structure in Wurtzite

materials. Recently, Zhang et al. [32] used ECCI to study the dislocation patterns around nano-indents and quantified the dislocation densities in TWIP steel.

Over the last two decades, indentation along with EBSD have been conducted to study the local deformation mechanisms including indentation size effect [33-34]. The model presented by Nix and Gao [35], which is built on the concept of Geometrically Necessary Dislocations (GNDs) has been widely used in the literature to understand the ISE behavior. However, the physical significance of the Nix-Gao model is still under debate [36] and validation further requires direct experimental evidence based on dislocation structures at various length scales. The conventional EBSD techniques used the Nye's framework based on the Hough transform analysis to determine the GND densities. Demir et al. [34] used Conventional EBSD Hough based analysis to measure the GND densities and investigate the ISE using 1 μm spherical indenter tip. They reported that the GND density does not increase with decreasing indentation depth, but rather drops. Qiao et al. [37] modified the Nix-Gao model, including tip rounding effect and showed that indenter tip bluntness can cause the reduction in dislocation densities at lower indentation depths. Therefore, in Demir et al. [34] work, a drop in GND density at lower indentation depth was observed. Recently, Wilkinson et al. have developed the cross-correlation based analysis of EBSD patterns (named as HR-EBSD), which allows to measure elastic strains and lattice rotations at a sensitivity of about 10^{-4} [38-39]. This cross-correlation based technique has been successfully employed to study the strain state and lattice rotation gradient at local scales in a wide range of materials [40].

1.1 Objectives and Statement of Work

Due to the stable cubic symmetry and ductility of STO, it is considered as a model system to study extended defect structures in perovskite oxide materials and their effect on the ionic and electronic transport properties [41]. Despite of aforementioned experimental local-scale studies and comprehensive uniaxial testing on bulk single crystal plasticity of STO, our knowledge of dislocation structure evolution at small scales and details of dislocation based nanoplasticity in STO is still very limited. The existing indentation experiments have mostly been conducted at high loads using pyramidal indenter geometries, where the plastic zone is already fully developed and cannot provide insights into local dislocation arrangements and mechanisms (from incipient plasticity to a fully developed plastic zone) in this perovskite material. Moreover, none of the indentation studies discuss the ISE behavior in STO, which is

more pronounced at the local-scale. Surprisingly, STO exhibits very high macroscopic indentation hardness of ~ 9.5 GPa [3], which is unexpected for a material having a yield strength of only ~ 120 MPa [23]. The reason for such a large discrepancy is still an open question. The knowledge of the dislocation structure at different length scales and the size of the plastic zone are of key importance to understand these missing details and potentially interesting for tailoring the local ionic conductivity in this model perovskite material. Therefore, the aim of the present thesis is to study the 3D dislocation structure evolution (around and below the indentations) at local scales in (001) STO single crystal and to analyze the underlying mechanisms.

To accomplish this task, a novel approach, combining 3D dislocation etch-pit analysis along with HR-EBSD is used here. The spherical and Berkovich indentations are performed at various length scales to investigate the dislocation structure evolution in the regime A. The sequential polishing and etching technique (SPET) is used to reveal the dislocation etch-pit structure at various sub-surface depths using SEM, EBSD and confocal laser microscopy. The SPET obtained cross-section provide complete sets of dislocation etch-pit patterns. From the dislocation etch-pit shape and by tracing the dislocation pile-ups, the slip along $\langle 110 \rangle \{110\}$ systems are found to be more favorable for both Berkovich and spherical indentations. The experimental observations along with derived hypotheses on the local defect structure and evolution are corroborated by Molecular Dynamic (MD) spherical indentation simulations, which are performed by Alexander Stukowski in collaboration with Materials Modelling Division of TU Darmstadt.

The HR-EBSD analysis conducted on SPET obtained cross-sections can provide a complete set of GNDs distribution along with elastic strain fields (around and underneath the indentations), which are not feasible with Focused Ion Beam (FIB) based EBSD and TEM analyses. Furthermore, the dislocation densities are quantified from etch-pits and HR-EBSD data obtained on SPET obtained cross-sections. With these independent measurements of dislocations, a direct evidence for the physical basis of indentation size effect is reported for the first time in STO.

Chapter 2 Fundamentals and Review of Relevant Literature

2.1 Strontium Titanate

2.1.1 Crystal Structure

Strontium titanate is an oxide ceramic material, which crystallizes in the ABO_3 cubic perovskite structure with a space group of $Pm\bar{3}m$ at room temperature. In simplest and highest symmetry cubic phase, eight strontium (Sr) atoms lie at the cube corners, six oxygen (O) atoms sit at the center of each face and one titanium (Ti) atom sits in the center of the cube as illustrated schematically in Fig. 2.1.1.

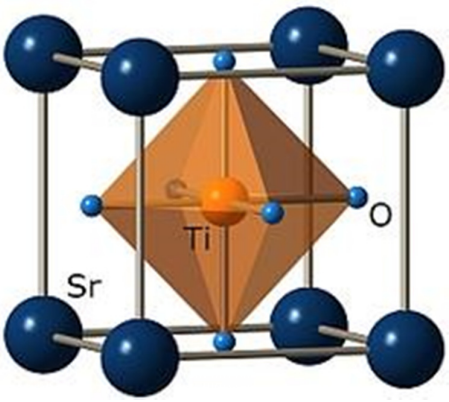

Fig. 2.1.1: Atomic structure of STO at room temperature [42]

Within the TiO_6 octahedra, a hybridization of the O-*2p* states with the Ti-*3d* states results in a distinct covalent bonding, while Sr^{+2} and O^{-2} ions exhibit ionic bonding character, which leads to a mixed ionic-covalent bonding properties [43]. Such chemical bonding nature of STO consequences to a distinctive structure, which makes it a model electronic material. In the cubic state, the lattice parameter of STO is 0.3905 nm. The summary of the other physical properties of STO is given in Table 2.1.1.

The STO retain its cubic symmetry in a wide range of temperature regime, i.e., from room temperature to its melting point. It undergoes a phase transformation from cubic to tetragonal phase at ~ 105.5 K and at ~ 65 K from tetragonal to the orthorhombic structure [16-17]. The remarkable stable cubic structure symmetry of STO in a wide range of

temperature range makes it an excellently suited perovskite material for the study of mechanical properties.

Table 2.1.1: Physical properties of strontium titanate at room temperature

Properties	Value
Melting Point	2080 °C
Atomic density	5.12 g/cm^3
Mohs hardness	6
Dielectric Constant (ε_o)	300
Thermal conductivity	12 W/m.K
Coefficient of thermal expansion	9.4 x 10^{-6}
Refractive index	2.31 – 2.38

2.2 Nanoindentation

2.2.1 Background

The indentation testing has been commonly used to determine the hardness of materials. The indentation hardness can be defined as: "the measure of resistance to permanent local deformation in a material". The indentation technique has its origins in the Mohs' hardness scale of mineral hardness of 1822, in which materials are ranked according to the ability of one material to leave a permanent scratch on another material visibly. The mineral Talc is assigned the minimum value of "1" and diamond is assigned the maximum value of "10" on the scale. Later on, the traditional hardness testing, i.e., Brinell, Rockwell, Vickers and Knoop are developed in which a known load is applied to press a hard tip (usually made of diamond, carbides or stainless steel) into a material and removed after some holding time. The residual impression is measured usually via microscope and hardness is calculated from the following formula:

$$H = \frac{P_{max}}{A} \qquad \textit{(Eq. 2.2.1)}$$

Where P_{max} is the maximum applied load and A is the projected area at maximum load.

Nanoindentation (also known as Depth-Sensing Indentation or Instrumented Indentation Testing) is the development of the traditional hardness testing technique to determine the local properties of the very small volume of material in a more precise and accurate manner. The major difference between the traditional hardness testing and nanoindentation is that the force and penetration are measured during the entire indentation experiment. In traditional hardness testing, the residual impression is measured by optical microscopy at only one applied force.

From the past two decades, Nanoindentation is a widely used technique for studying the local deformation behavior and nano / micro-scale mechanical properties like elastic modulus, hardness, strain-hardening, cracking, phase transformations, creep, fracture toughness, and energy absorption in a wide range of materials, based on elastic contact theory and load – displacement (LD) data. In recent years, high-temperature nanoindentation has developed significantly and many commercial state of the art nanoindenters with high-temperature capabilities are available, e.g., Nanoindenter G200 (Keysight Technologies, USA) equipped with Surface GmbH laser heater, InSEM (Nanomechanics Inc.) etc. These nanoindenters are equipped with fully automated methods including partially loading/unloading and continuous stiffness measurement (CSM) method. The popularity of these nanoindentation systems is certainly due to an automatic data collection and analysis, which is facilitated by the breakthrough of the Oliver – Pharr method [44]. This method allows to extract the mechanical properties directly from the LD curves. An exemplary LD curve along with important parameter used in the Oliver – Pharr analysis is shown in Fig. 2.2.1.

The basic assumptions of this method are:

1. Deformation upon unloading is purely elastic.
2. The compliance of the specimen and the indenter tip can combined as spring in series, e.g.,

$$\frac{1}{E_r} = \frac{1-\nu_s^2}{E_s} + \frac{1-\nu_i^2}{E_i}, \qquad \textit{(Eq. 2.2.2)}$$

where E_r is reduced modulus, E is Young's modulus, ν is the Poisson's ratio and subscripts 'i' and 's' refer to indenter and the specimen, respectively.

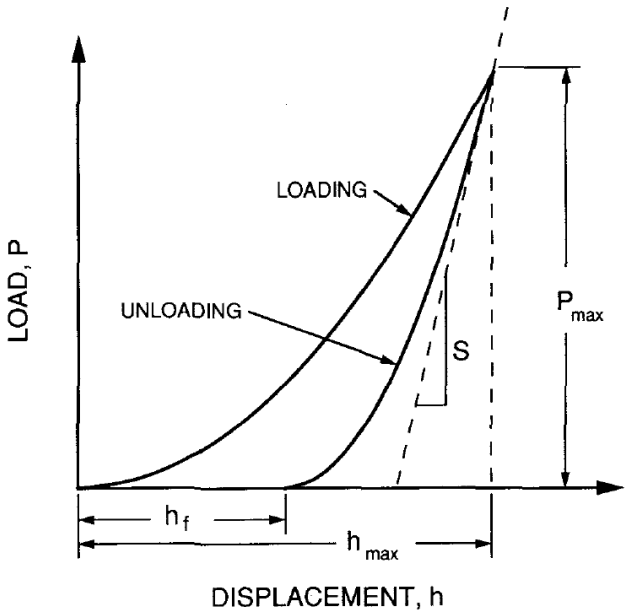

Fig. 2.2.1: An exemplary indentation load – displacement curve along with important parameters used in the Oliver-Pharr analysis [44]

3. The contact can be modeled via an analytical model of contact between rigid indenter of defined shape using following Sneddon's relation [45]:

$$S = \frac{2}{\sqrt{\pi}} E_r \sqrt{A}, \qquad \textit{(Eq. 2.2.3)}$$

where S is the contact stiffness. The projected area at peak load (A) can be calculated from the following relation:

$$A = f\,(h_c), \qquad \textit{(Eq. 2.2.4)}$$

where h_c is the contact depth and the exact form of this function is called "Area Function", which depends on the geometry of the indenter. The most commonly used indenter geometry is a Berkovich diamond indenter. The Berkovich indenter has three-sided pyramid geometry, which has about the same aspect ratio as of four-sided Vickers pyramid indenter.

Fig. 2.2.2 shows an illustration of a section through an indentation showing different quantities used in the Oliver – Pharr analysis:

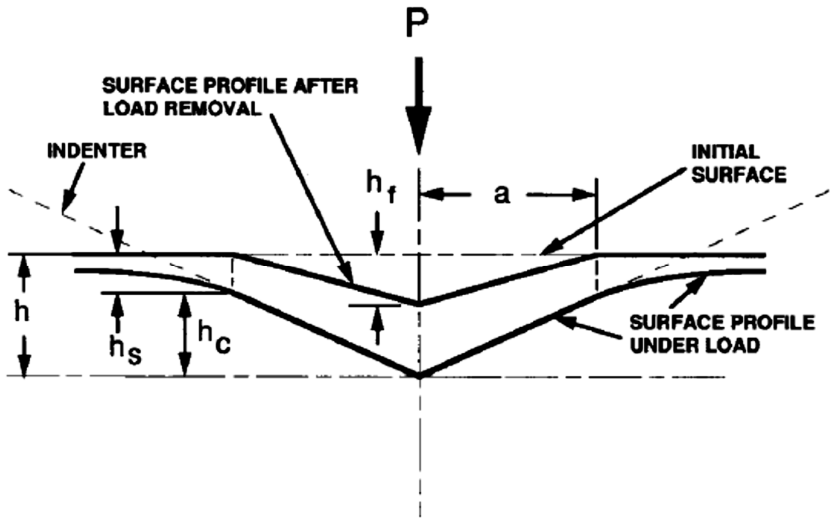

Fig. 2.2.2: A schematic of the indentation geometry at maximum load and after unloading along with important parameters used in the Oliver – Pharr analysis [44]

For an ideal Berkovich indenter geometry, the area function is given by

$$A = 24.56\, h_c^2 \qquad \textit{(Eq. 2.2.5)}$$

If the indentation depth is greater than 2 microns, then Eq. 2.2.5 can be used to calculate contact area, because, at this scale, the difference between the ideal and real geometry is negligible. If the total indentation depth is less than 2 microns, the rounding at the apex of the indenter must be considered and the real contact area is then given by [44]:

$$A = 24.56\, h_c^2 + C_1 h_c^1 + C_2 h_c^{1/2} + C_3 h_c^{1/4} + \ldots\ldots\ldots\ldots\ldots\ldots\ldots\ldots + C_8 h_c^{\frac{1}{128}}, \qquad \textit{(Eq. 2.2.6)}$$

where C_1 to C_8 are the constants, which are determined empirically by indenting a known material usually fused silica. This process is often called "*Area Function Calibration*". For other simple indenter geometries (sphere, cone, flat punch) another form of area function can be used and available easily in the literature [46]. The contact depth (h_c) is further calculated as:

$$h_c = h_{max} - \varepsilon \frac{P_{max}}{S}, \qquad \textit{(Eq. 2.2.7)}$$

where ε = 0.72, 0.75 and 1 for cone, sphere and flat-punch geometries, respectively. The contact stiffness *S* is determined by fitting the LD curve data obtained during unloading to an expression of the form following a power law:

$$P = B(h - h_f)^m, \qquad \textit{(Eq. 2.2.8)}$$

where *B*, *m* and h_f are determined by a least square fitting procedure. So, knowing the contact stiffness from unloading segment of LD curve, the hardness can be calculated from Eq. 2.2.4 and 2.2.1.

2.2.2 Incipient Plasticity and Pop-in Events

During nanoindentation test, the continuous measurement of force and penetration enable to identify the different events occurring within the material. One of such widely discussed events observed in many materials is known as "pop-in" and appears as a sudden displacement burst in nanoindentation LD curve [47-48] as shown in Fig. 2.2.3.

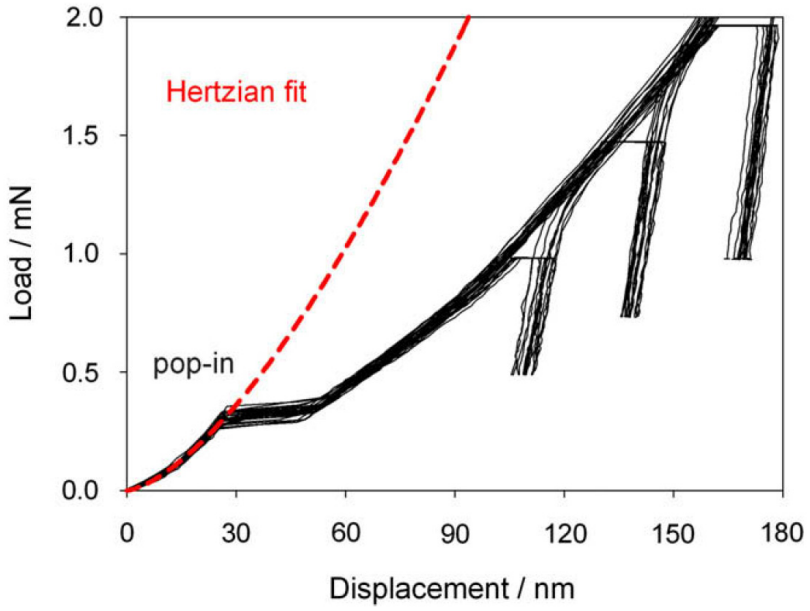

Fig. 2.2.3: Load - displacement data showing first pop-in event in (111) oriented CaF_2 [27]

This pop-in event depicts the elastic to plastic transition of a material associated with dislocation activities like homogeneous dislocation nucleation, source activation etc. [49-51]. The indenter tips are not ideally sharp and rounding at the apex of the indenter can be

considered as spherical. Therefore, the Hertzian contact model [52] can be used to fit the initial part of the LD curve to obtain valuable data like tip radius as per the following relation:

$$P = \frac{4}{3} E_r \sqrt{R}\, h^{3/2}, \qquad \textit{(Eq. 2.2.9)}$$

where R is the tip radius and h is the indentation depth. The origin of pop-in has been intensively studied by many authors and the pop-in may be induced by other factors such as the breaking of surface oxide layer, the phase transition in amorphous alloys and film delamination [28-29,53]. If the first pop-in event occurs at the initiation of homogeneous dislocation nucleation, the maximum shear stress (τ_{max}) at this first pop-in event is generally found to be close to the theoretical shear strength of material. The τ_{max} is frequently determined from the Hertzian elastic contact theory using $\tau_{max} = 0.31 p_o$ [54], Where

$$p_o = \sqrt[3]{\frac{6P_{(pop-in)}E_r^2}{\pi^3 R^2}}, \qquad \textit{(Eq. 2.2.10)}$$

here $P_{(pop\text{-}in)}$ is the load at first pop-in event and R is the tip radius.

The homogeneous nucleation of dislocations at incipient plasticity or first pop-in event is still under debate. The effect of pre-existing dislocations on the incipient plasticity have been discussed in many studies. The different approaches like dislocation density gradients, different percentages of pre-deformation have been used to explain the effect of pre-existing dislocations on the incipient plasticity. Bahr et al. [28] first used the micro-indentation in tungsten specimen to generate dislocation density gradients around the micro-imprints. They then performed the nanoindentation test in the vicinity of micro-indentation and found an increase in pop-in load with increasing distance from the center of the micro-imprints. Lodes et al. [55] used a similar approach on single crystal CaF_2 along with molecular dynamics (MD) simulations. They etched the CaF_2 after first Berkovich micro-imprints to reveal the plastic zone / dislocation gradient around the residual impression and then performed nanoindentation as depicted in the inset region of Fig. 2.2.4a. From experimental and simulation evidence they concluded that the large density of pre-existing dislocations lowers the pop-in load or even causes it to disappear as shown by fore-displacement curves in Fig. 2.2.4b

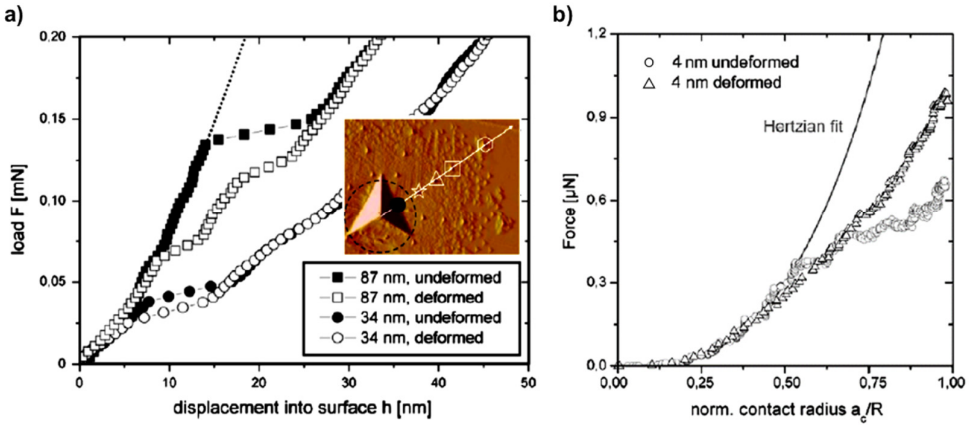

Fig. 2.2.4: Pop-in behavior of un-deformed and deformed CaF_2 (111) during Nanoindentation (a) experimental using 87 nm and 34 nm tip radii (b) MD simulation using 4 nm tip radius [55]

Phani et al. [56] and Bei et al. [57] studied the effect of pre-existing dislocations using pre-strained Mo fibers and micro-pillars, respectively. They observed a scattering in the pop-in load for intermediate pre-strain specimens (4%) and found that the as-grown fiber and micro-pillars yield at higher strengths close to the theoretical shear strength while the pre-strained fibers and micro-pillars yield at considerably lower stresses. Although the micro-indentations / pre-straining the testing specimens are good ways to create the pre-existing dislocations, but these approaches also have some drawbacks. For example, the dislocation structure around the micro-imprint is very complex, which leads to large heterogeneities. Moreover, the surface topography around the indent may not be suitable for accurate measurement due to the high plastic deformation. Recently, Montagne et al. [29] studied the influence of pre-existing dislocations on the pop-in phenomenon in MgO single crystal using ball indentation. They used a nano-etching technique along with AFM, which enables to distinguish between the individual pre-existing dislocation etch-pits and the dislocation etch-pits generated from the indentations. They found that for 10 mN and 20 mN loads, the indentations performed close to the pre-existing etch-pits undergo the plastic deformation and a clear pop-in observed in LD curve. However, the indentations conducted in the dislocation free region lead to an elastic contact and no pop-in was observed in the LD curve as shown in Fig. 2.2.5.

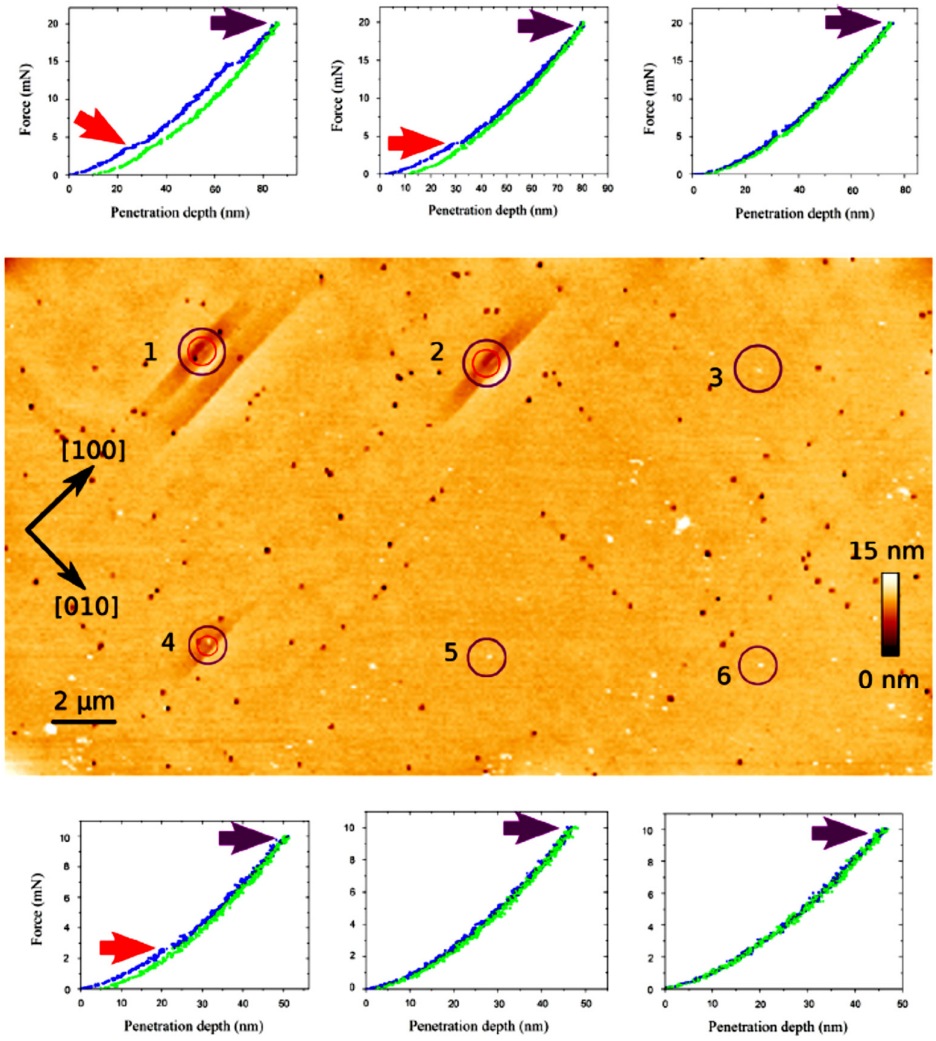

Fig. 2.2.5: AFM image showing six indented areas with their respective LD curves. The pits in the image represent the pre-existing dislocations left from the cleavage process [29]

Moreover, they reported a significant scattering in the pop-in load for a particular pre-existing dislocation density as illustrated in Fig. 2.2.6.

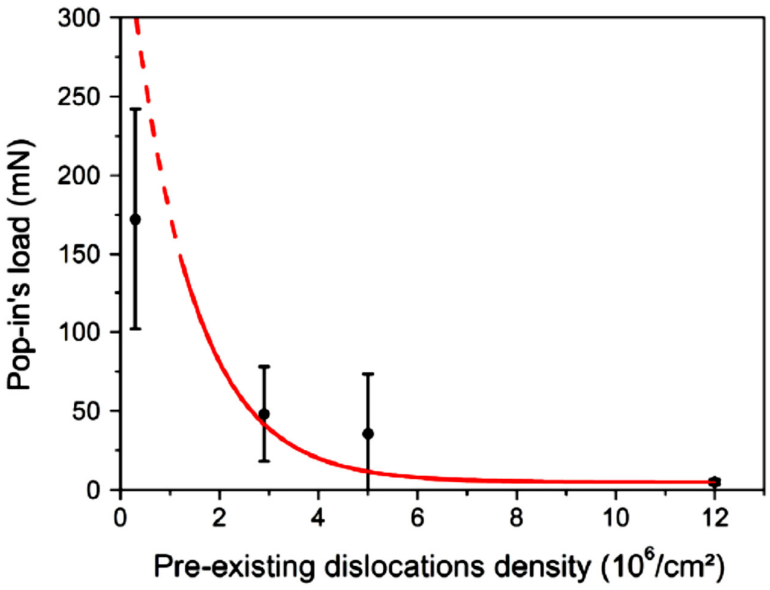

Fig. 2.2.6: Influence of pre-existing dislocations on pop-in load [29]

In the presence of pre-existing dislocations, one would probably expect the dislocation source activation. However, they reported more paradoxical observations concluding that the dislocations nucleated during the pop-in are totally independent of the pre-existing dislocations. They suggested that this paradox can be explained by the fact that the pre-existing dislocations are gliding during the indentation test due to the indenter stress field. This displacement leads to slip lines formation below the contact area, which likely to modify the surface pressure distribution and thus induce local stress concentration. Moreover, they suggested that another possibility can be related to dynamic effects. Despite of some discrepancies, all of these experimental and simulation experiments unanimously confirmed that the pre-existing dislocations lower the first pop-in load. However, further experimentations are required to explain these mechanisms in detail.

In addition to that first pop-in event depicting the incipient plasticity, some materials show multiple pop-in events in the loading part of the LD curve as shown schematically for an indentation performed close to grain boundary (GB) in Fig. 2.2.7.

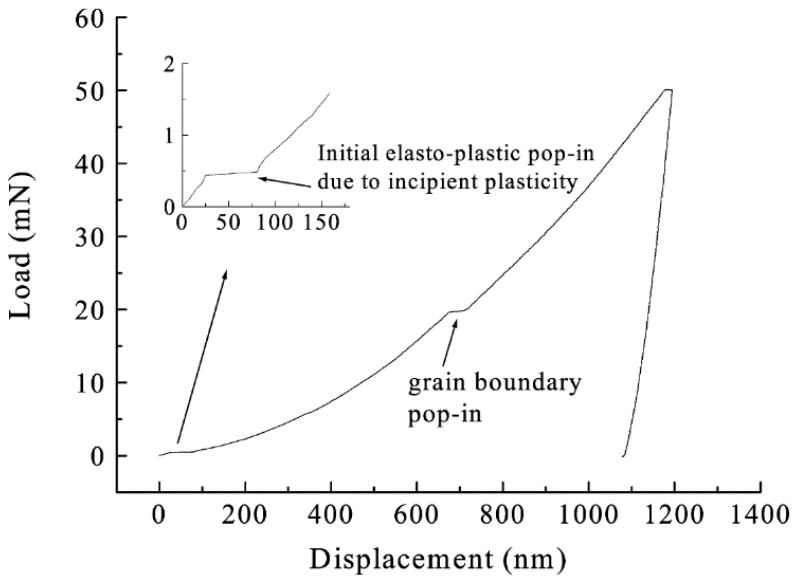

Fig. 2.2.7: The load-displacement curve showing initial and secondary pop-in event due to grain boundary [58]

In the literature, the occurrences of these multiple pop-in events have been related to different logics. One of these possibilities is the formation of dislocation bands parallel to specific crystallographic planes. For example, Bradby et al. [59] reported the multiple discontinuities in GaN epilayers nanoindentation LD curves and related this behavior with multiple slip bands revealed by TEM as shown in Fig. 2.2.8.

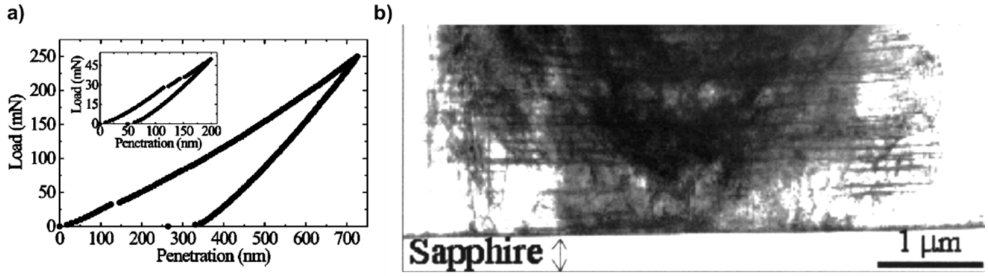

Fig. 2.2.8: a) Typical LD curve for max. load of 250 mN showing a pop-in event. Inset: LD curve for max. load of 50 mN showing multiple pop-in events at 28 mN and 34 mN, (b) Bright-field XTEM image of spherical indent in GaN at max. load of 250 mN [59]

The pores and / micro-cracks below the indentation may also cause the multiple pop-in events in the ceramics [60]. The pressure-induced phase transformations have also been observed during nanoindentation, which leads to multiple pop-in events in materials like silicon and metastable austenite [61-62]. The indentations performed close to the GB can also lead to the multiple pop-in events (Fig. 2.2.7), which might relate to slip transmission across the GB [58,63]. The multiple pop-in events are also very common to observe in bulk metallic glasses

and quasi-crystals and the possible mechanisms involved the discrete emission of shear bands at or below critical load as well as critical loading rate [64-65].

In short, pop-in events can occur frequently in many materials and these events are extremely sensitive to nanoscale events like homogeneous and / or heterogeneous dislocation nucleation and the movement of these dislocations is specific and / or across preferential planes, phase transformation and applied load. The mechanisms of pop-in events in metals, glass, ceramics, composites and biomaterials are certainly different and require a comprehensive research to understand these mechanisms in detail. STO also shows multiple pop-in events in nanoindentation LD curve and its origin is studied in the present work via observation of dislocation structure around the residual impression.

2.2.3 Indentation Size Effect

The indentation size effect (ISE) is among one of several size effects on strength for which "smaller is stronger". It can be defined as "the increase in hardness with decreasing indentation depths through the use of geometrically self-similar indenters such as pyramids and cone". The physical origins of ISE are generally believed to lie in strain gradients produced underneath the indentation [66]. For most of the materials, ISE is more pronounced at the depths of less than 1 μm. A classic example of ISE data is that of McElhaney et al. [67] which is frequently cited in the literature, is shown in Fig. 2.2.9.

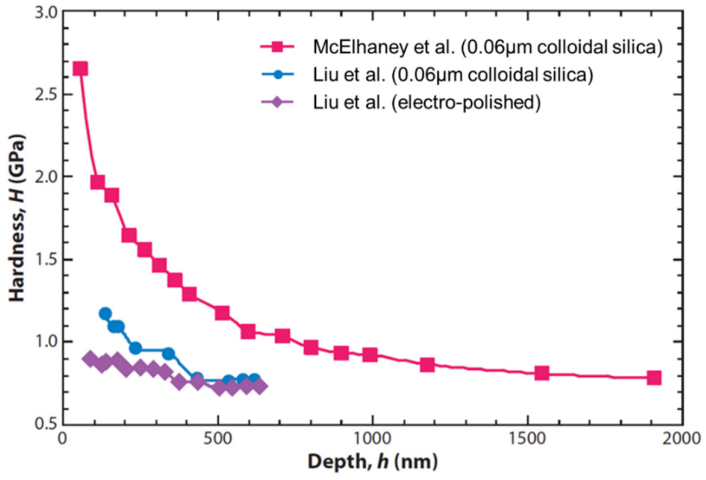

Fig. 2.2.9: Hardness vs depth plot for (111) Cu single crystals obtained in nanoindentation experiments [66]

In that work, they conducted the Berkovich nanoindentation experiments on (111) Cu single crystal and observed a significant increase in hardness at depths below few micrometers.

However, the later studies suggest that the surface preparation plays a vital role to study such small scale phenomenon. Liu et al. [68] studied the ISE on (111) Cu single crystal using two different specimen preparation approaches. In the first approach, the specimens were prepared in the same way as by McElhaney et al., i.e., standard grinding followed by 20 min of polishing with 0.06 μm silica suspension, which is often recommended to prepare high-quality, relatively damage-free surface. However, even using similar surface preparation protocol, Liu et al. observed significant smaller indentation size effect as shown in Fig. 2.2.9. In the second approach, Liu et al. prepared the (111) Cu single crystal surface via electro-polishing, which even further reduced the magnitude of ISE. The exact reason for this discrepancy is not clear yet, but may be related to the difference in the grinding process (inadequate removal of damage from the early part of grinding) and / or initial dislocation structure in the crystal. Moreover, in the case of higher pre-existing dislocation densities, ISE can completely disappear. Therefore, surface preparation is extremely important to study ISE and data reporting should be carefully examined.

To understand the ISE, many mechanistic models have been proposed in the literature. However, the model presented by Nix and Gao [35], which is built on the concept of geometrically necessary dislocations (GNDs) has been widely used to study the ISE behavior. According to the Nix-Gao model, the GNDs are the dislocations that must be present near the indentations to accommodate the volume of material displaced by the indenter at the surface. In the Nix-Gao model, the indenter is assumed to be a rigid cone whose self-similar geometry is defined by an angle θ and the indentation is accommodated by circular loops of GNDs with Burgers vector normal to the surface, as shown schematically in Fig. 2.2.10.

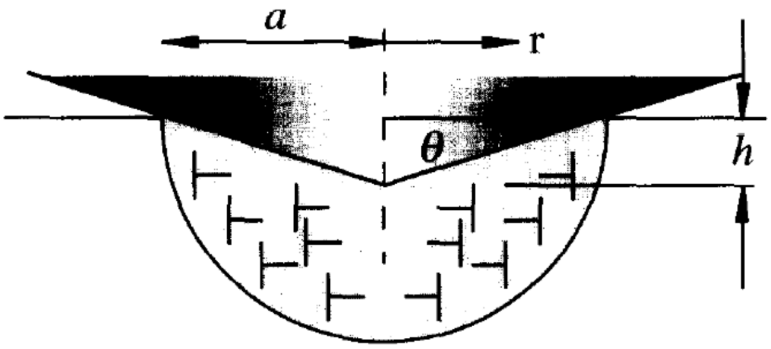

Fig. 2.2.10: GNDs created by a rigid conical indentation. The dislocation structure is idealized as circular dislocation loop [35]

The flow stress 'σ' is related to the total dislocation density 'ρ_t' through the Taylor relation:

$$\sigma = \sqrt{3}\,\alpha G b \sqrt{\rho_t}\,, \qquad \textit{(Eq. 2.2.11)}$$

where α is constant, G is the shear modulus and b is the Burgers vector. This relation can be combined with the Tabor relation, $H = 3\sigma$, to relate the hardness H and flow stress 'σ'. Furthermore, the total dislocation density 'ρ_t' is assumed to be the simple mathematical sum of the density of GND and SSD. i.e., $\rho_t = \rho_{GND} + \rho_{SSD}$. Hence the relation between hardness and dislocation density is expressed as:

$$H = 3\sigma = 3\sqrt{3}\,\alpha G b \sqrt{\rho_{GND} + \rho_{SSD}} \qquad \textit{(Eq. 2.2.12)}$$

From Fig. 2.2.10, the simple geometric consideration, then led to GND density as follows:

$$\rho_{GND} = \frac{3}{2}\,\frac{tan^2\theta}{bh} \qquad \textit{(Eq. 2.2.13)}$$

This relation contains the essential physics of ISE i.e., the GND density is inversely proportional to the depth and rise dramatically when the contact is small. Combining Eq. 2.12 and 2.13 leads to:

$$\frac{H}{H_0} = \sqrt{1 + \frac{h^*}{h}}, \qquad \textit{(Eq. 2.2.14)}$$

where

$$H_0 = 3\sqrt{3}\,\alpha G b \sqrt{\rho_t}\,, \qquad \textit{(Eq. 2.2.15)}$$

represents the macroscopic hardness that would arise from the SSD alone in the absence of any GND and

$$h^* = \frac{81}{2}\,b\alpha^2\,tan^2\theta\,\left(\frac{G}{H_0}\right)^2\,, \qquad \textit{(Eq. 2.2.16)}$$

is the length that characterizes the depth dependence of hardness. The characteristic length scale h^* is not constant for a given material and indenter geometry. Rather, it depends

on both material parameters (b and ρ_{SSDs}) and geometric parameter (θ). The Eq. 2.14 can be re-write as:

$$H^2 = H_o^2 \left(1 + \frac{h^*}{h}\right), \qquad \textit{(Eq. 2.2.17)}$$

which implies that a plot of H^2 versus *1/h* should be linear. The intercept at hardness axis gives H_o and slope of the line provide h^*. Nix and Gao applied the model to classical Cu data of McElhaney et al. and observed a remarkable linearity of these data sets as shown in Fig. 2.2.11. This linearity of the data has been taken as the primary evidence for the Nix-Gao mechanisms. Therefore, plotting H^2 versus 1/h is considered as the primary test for any geometrically self-similar (like pyramids and cones) indentation experimental data, which shows an ISE behavior.

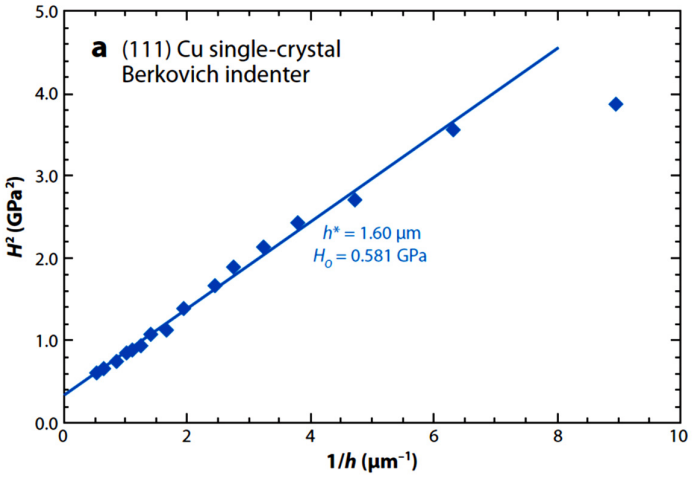

Fig. 2.2.11: A plot of H^2 versus 1/h for (111) Cu data of McElhaney et al. [66]

For spherical indenter geometries, the ISE is not manifested through the depth of penetration, but rather through the radius of the sphere. Swadener et al. [69] demonstrated this behavior by conducting indentation experiments on Iridium (Ir) alloy specimens using different spherical indenter radii ranging from 14 μm to 1600 μm and represented the Hardness as a function of contact radius, a, normalized with respect to the indenter radius, *R*, as shown in Fig. 2.2.12.

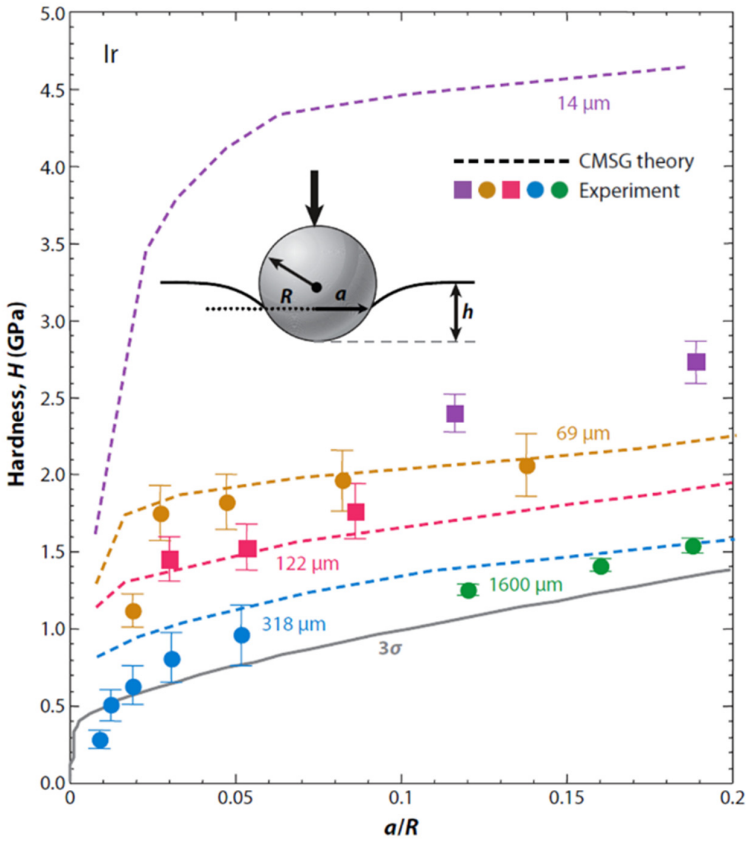

Fig. 2.2.12: The ISE for spherical indenters in Ir alloy using different indenter radii ranging from 14 µm to 1600 µm [66]

The data clearly show higher hardness for smaller sphere radii. The spherical indenter is not self-similar geometry, therefore, the strain induced in the material increases with depth and so the hardness also increases if the material work hardens. Thus, the depth dependency of hardness for spherical indenters is a result of classical work-hardening effect. In Fig. 2.2.12, the dashed lines reflect the prediction of finite element model that incorporate the strain gradient plasticity effects, which is are based on the theory of CMSG (Conventional Mechanisms-based Strain Gradient Plasticity) [70-71]. The experimental results and model predictions are in good agreement for the large sphere, but for the smallest sphere (R = 14 µm), the model significantly overestimates the hardness, which indicates a breakdown in the Nix-Gao mechanism for very small spheres [69,72]. The curve at the bottom of the plot labeled as 3σ is the prediction of the hardness based on the tensile test data by applying Tabor's method [73]. For the large indenter radii, the hardness is roughly consistent with the Tabor prediction, but the smaller indenters produce higher hardness and shift the curve up due to ISE. Hence,

along with geometrically self-similar indenters, ISE in spheres can also be mechanistically understood by the Nix-Gao mechanisms.

Despite of widespread application of the Nix-Gao model, it has several shortcomings. One of this limitation which received a great attention is the assumption that all the GNDs are accommodated in a hemisphere, namely plastic zone, with a radius equal to the contact impression. However, Swadener et al. [69] argued that with similar sign GNDs and constraining those in a small volume would result in large mutually repulsive forces that tend to spread them outward to occupy the large volume. Hence, the relationship between ρ_{GND} and *1/h* expect to breakdown at some small scale and it would overestimate the hardness for very shallow pyramidal indentations or indentations made with very small sphere because the real GND densities would be smaller. That's why in Fig. 2.2.12, for small 14 μm spherical indentations modelling data, the hardness prediction was too high. Feng and Nix [74] also showed that the storage volume of the GNDs in MgO is much bigger than the contact radius and they apply a correction to the Nix-Gao model for smaller indentation depths.

Durst et al. [75] used a different approach to determine the storage volume of dislocations by assuming that the radius of the hemisphere in the Nix-Gao model is not necessarily equal to the contact radius, but scales with it by a material dependent factor, *f*. Hence the Nix-Gao model can be modified as:

$$\rho_{GND} = \frac{\lambda}{V} = \frac{\frac{\pi h a_c}{b}}{\frac{2}{3}\pi a_{PZ}^3} = \frac{3}{2}\frac{h a_c}{b f^3 a_c^3} = \frac{3}{2}\frac{1}{f^3}\frac{\tan^2\theta}{bh}, \qquad \textit{(Eq. 2.2.18)}$$

here the radius of the plastic zone is approximated by $a_{PZ} \approx f a_c$ and *f* is the storage volume of dislocations, which can be estimated by fitting experimental data or conventional FEM of the size of the plastic zone. The Fig. 2.2.13 shows an axisymmetric geometry of a Berkovich indenter contacting an elastic-plastic material.

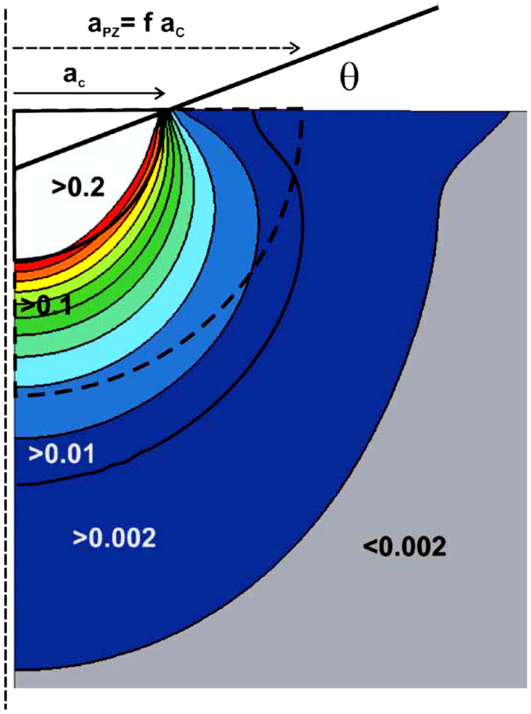

Fig. 2.2.13: FEM simulation: Axisymmetric geometry of Berkovich indenter contacting an elastic - plastic material [75]

The extension of the plastic zone is shown for $f = 1$ (solid line), which yields the length scale given by the Nix-Gao model and $f = 1.9$ (dotted line) yields the length scale accounting bigger size of the plastic zone. This modified Nix-Gao model is applied to several materials (metal, alloys, ceramics, and solid-solutions) and f value, usually, falls in the range of 1.5 to 2.5 [27, 75-78]. An exemplary experimental ISE data using the partial load-control and CSM method in (100) Ni single crystal with modified Nix-Gao model fittings is shown in Fig. 2.2.14.

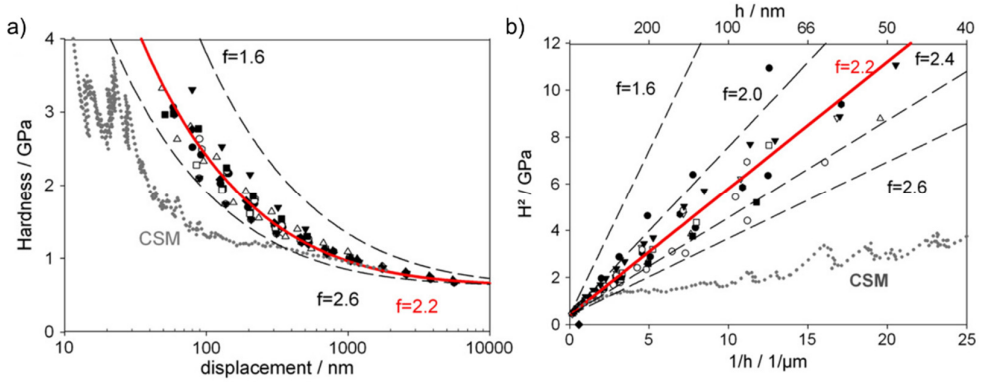

Fig. 2.2.14: ISE in (111) oriented Ni from CSM and partial loading and unloading indentation test. (a) Hardness as a function of depth with corresponding model size effect (solid lines), (b) corresponding Nix-Gao plot for all data [76]

This particular example explained the sensitivity of parameter *f* for the fitting. The experimental data are fitted for different values of *f* and it became obvious that most of the data lie in the range of $2.0 < f < 2.4$, where 2.2 gives the best fit for Ni. Moreover, the CSM data yield the size effect in the Nix-Gao plot, but a clear deviation from linear behavior can be seen at smaller indentation depth. It might be related to the fact that during harmonic loading of the sample, the tip loses contact at smaller loads [79]. However, the exact reason for this is still unclear, therefore, for smaller indentation depths, researchers preferred to use standard loading and partial unloading method.

The phenomenon like dislocation source activity, cross-slip etc. are significantly temperature dependent. The small changes in temperature could lead to significant changes in the details of ISE. Until now, very limited literature is available describing the temperature dependence of ISE. Recently, Franke et al. [80] reported preliminary observations of ISE in Cu at room temperature, 150 °C and 250 °C. They used modified Nix-Gao model to fit their experimental data and found a significant decrease in ISE and h^* with increasing temperature as shown in Fig. 2.2.15.

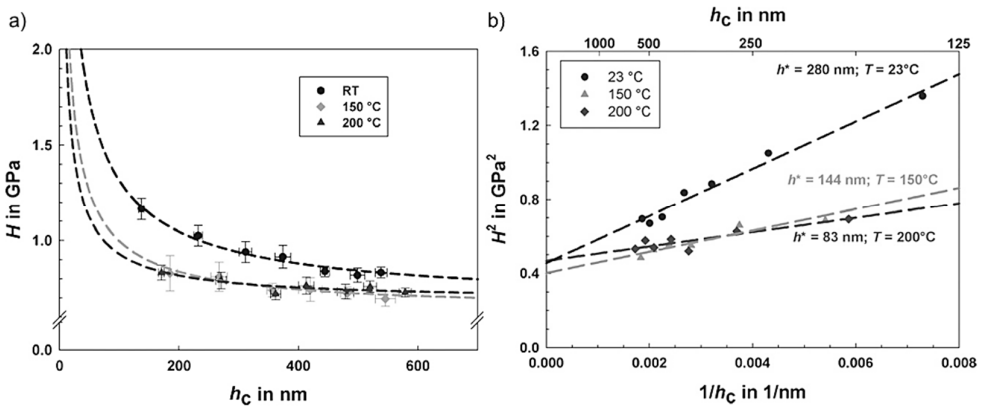

Fig. 2.2.15: Room temperature, 150 °C and 200 °C nanoindentation data on Cu single crystal with dotted lines indicating best fit from modified Nix-Gao Model (a) Hardness as a function of displacement (b) Nix-Gao plot of ISE [80]

They explain the significance of h^* using modified Nix-Gao model. The hardness as a function of indentation depth can be given by:

$$H = H_{fric} + MC\alpha Gb\sqrt{\rho_{SSD} + \rho_{GND}}, \qquad \textit{(Eq. 2.2.19)}$$

where H_{fric} is the frictional hardness, M is the Taylor factor and α is a constant. Considering $H_{fric} = 0$ and by comparison Eq. 2.18 and 2.19, suggest that:

$$H_o = MC\alpha Gb\rho_{SSD}^{1/2}, \qquad \textit{(Eq. 2.2.20)}$$

and

$$h^* = \frac{3}{2}\frac{1}{f^3}\frac{\tan\theta}{b}\frac{1}{\rho_{SSD}} \qquad \textit{(Eq. 2.2.21)}$$

This is very important relation explaining the dependency of h^* with respect to the storage volume of GNDs, f, and ρ_{SSD}, since Burgers vector b and indenter angle θ are constant parameters. Using this theoretical framework, Franke et al., reported that the decrease in characteristic length scale with an increase in temperature may be due to either increase of f or ρ_{SSD} or both. Kong et al. [81] performed nanoindentation experiments in the temperature range from 293 K to 353 K in SnAgCu lead-free BGA solder joints and also observed the decrease in h^* with the increase in temperature. Lee et al. [82] conducted the cryogenic nanoindentation experiments on [001] oriented face-centered cubic (FCC) {Aluminum (Al) & Gold (Au)} and body-centered cubic (BCC) {Tungsten (W) and Niobium (Nb)} single crystals and studied the

ISE at 160, 230 and 298 K. They reported that with a decrease in temperature from 298 to 160 K, for BCC metals, Nb and W, macroscopic hardness, H_o, increased by 107 % and 24 %, respectively. However, for FCC specimens (Al and Au), they did not observe significant changes in H_o which might be related to the intrinsic lattice resistance of BCC metals with a reduction in temperature. Moreover, they found a significant dependency of h^* on temperature. In all of these cryogenic and elevated indentation experimental results, a strong temperature dependency on h^* has been reported, which can only be understood in a theoretical framework. The Nix-Gao model does not explicitly take into account the thermal effects, so other physical explanations for h^* and H_o of temperature dependency are also possible. Despite of the aforementioned limitations of the Nix-Gao model, it has been widely accepted along with its modified versions to mechanistically understand the ISE in a wide range of material and temperature regimes.

2.3 Microstructural Observation Techniques

In order to establish the mechanistic origin of ISE, knowledge of the dislocation structure at different length scales and the size of the plastic zone are of key importance. Unfortunately, the observation of dislocation microstructures at such a small scale is not easy due to the complexity of the techniques required to image the dislocations at the submicron scale. Till now, the studies conducted to experimentally explore the 3D dislocation structure around and underneath the indentations are very limited, but a number of interesting observations are emerging. The advanced characterization techniques like EBSD in high-resolution scanning electron microscopes [32], TEM [25-26], Etching technique equipped AFM / SEM [27-29], and X-ray diffraction at synchrotron X-ray sources [83-84] have proven most useful to image the dislocation microstructure at various length scales and understanding local deformation mechanisms. In the present work, the dislocation microstructural observations have been made using chemical etching technique (equipped with SEM and confocal laser microscopy) and HR-EBSD techniques. Therefore, only these techniques along with relevant literature will be reviewed in proceeding section 2.3.1 and 2.3.2.

2.3.1 Chemical Etching Technique

The chemical etching technique has been widely used to reveal the dislocations at various length scales. It involves preferentially etching of a material, which makes the defects (e.g., dislocations, stacking faults) intersecting the surface visible by a small groove or pit known as "*Etch-pit*". Finding an etching solution or etchant that dissolves the defect region of

material much more quickly than the perfect region is the trickiest part. The theories of etching do not predict the composition of selective etchant for a material. The etchant or a crystal can only be chosen by trial and error basis, if it's not available in the literature. The formation of dislocation etch-pit arises mainly from the strain field associated with a dislocation and / or impurities segregated at the dislocation. The strain field and / or impurities produced a surface potential between the site of dislocation and the nearby perfect crystal, which causes a different etching rate.

The visible, sharp and contrasting shape of etch-pits can provide a valuable information about the nature of dislocation and crystal surface. Amelinckx [85], Gilman and Johnston [86] were the first to demonstrate the orientation of the dislocation line with respect to the surface from the shape of etch-pit in rock-salt crystals, which shows pyramidal shaped etch-pits for (100) surface. The logic toward which is the shift of the central deepest point of the etch-pit provide the indication of dislocation inclination with respect to the surface, as shown schematically in Fig. 2.3.1.

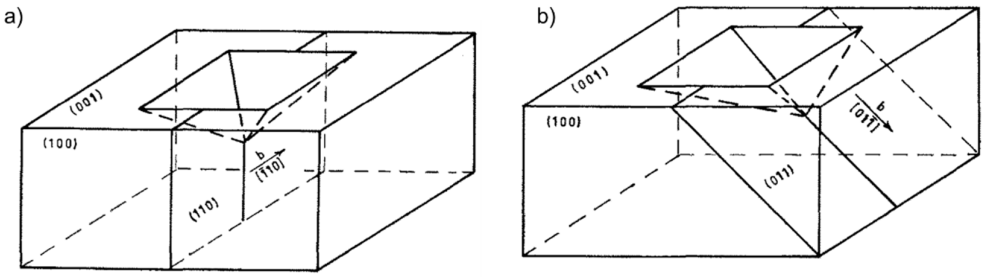

Fig. 2.3.1: Effect of inclination of dislocation line on shape of etch-pit, (a) Dislocation line is normal to the surface (symmetrical etch-pit), (b) Dislocation line is oblique to the surface (asymmetrical etch-pit) [87]

From the crystal symmetry and the known glide planes of (001) NaCl, they further demonstrate that the centered deepest point etch-pits (referred as symmetrical etch-pits) are edge dislocations with the dislocation lines perpendicular to the surface, whereas, the off-centered etch-pits (named as asymmetrical etch-pits) are screw in nature with dislocation lines lying on the planes 45° to the surface. The etch-pit shape produced by the edge and screw dislocation in NaCl labelled as A and B, respectively, are shown in Fig. 2.3.2.

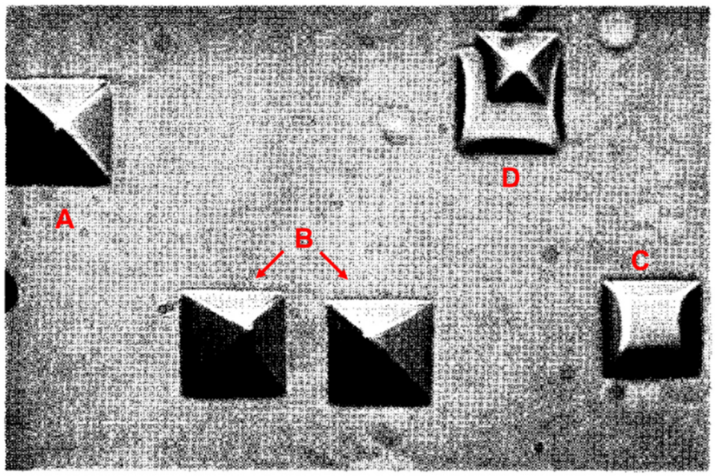

Fig. 2.3.2: Etch-pit shapes produced during etching of the NaCl single crystal (at 800X) [87]

Along with symmetrical and asymmetrical etch-pits, flat-bottomed etch-pits (labelled as C and D) in Fig. 2.3.2 can be seen clearly. During etching the (001) surface, an etch-pit remains pyramidal only if the dislocation line remains at its bottom. If for any reason the dislocation which is being etched disappears or moves (indicated as C and D in Fig. 2.3.2, respectively), the etch-pit does not etch deeper, but grows laterally to form a "Flat-bottomed" shape [87]. Gilman et al. [86] in their classical work on (001) oriented LiF observed that the etch-pits corresponding to edge dislocations were found to be much deeper compared to inclined screw dislocations, although the widths of all the etch-pits were the same. However, Nadgornyi et al. [88] and Sangwal et al. [89] in their work on (001) oriented NaCl and MgO, respectively, found that the etch-pits formed at edge dislocations are larger by 20% than those at screw dislocations. Patel et al. [90] reported the importance of etchant to reveal the edge or screw dislocations for (110) oriented $BaSO_4$ crystals. They found that concentrated HCl reveals etch-pits only at edge dislocations, while conc. H_2SO_4 along with KOH melt reveals both edge and screw dislocations. These discrepancies show that the evaluation of edge or screw nature of dislocation, alone from etch-pit shape is not sufficient.

The chemical etching technique along with AFM, TEM and / or SEM proved to be a powerful tool for analyzing the dislocation structure, activated slip system and studying the ISE behavior. Lu et al. [91] identified α, β and γ type of dislocation etch-pits with inversed trapezoidal, triangular and mixed shape using SEM analysis in GaN epilayers etched by molten KOH as shown in Fig. 2.3.3A.

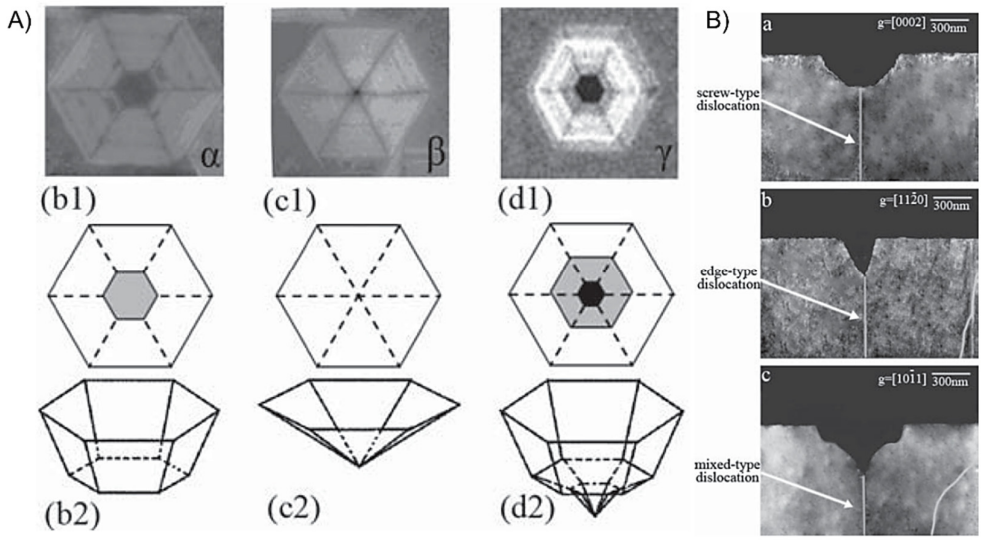

Fig. 2.3.3: (A) SEM images of α, β, and γ type etch-pits along with 2D and 3D schematics, (B) Cross-sectional TEM images of (a) α type, (b) β type, and (c) γ type etch-pit, respectively. [91]

From the further TEM analysis, they confirmed the screw, edge and the mixed character of α, β and γ type etch-pits, respectively (Fig. 2.3.3B).

2.3.1.1 Revealing Dislocation Structure after Indentations via Chemical Etching

Chemical etching has been used widely to study the dislocation structure around the indentations in a wide range of materials [92]. To study the dislocation structure below the indentations, researchers also used sequential polishing and etching technique. For example, Sadrabadi et al. [27] used sequential polishing, etching and imaging technique to reveal the dislocation structure around and underneath the indentations for 1 mN and 5 mN in (111) oriented CaF_2 as shown in Fig. 2.3.4.

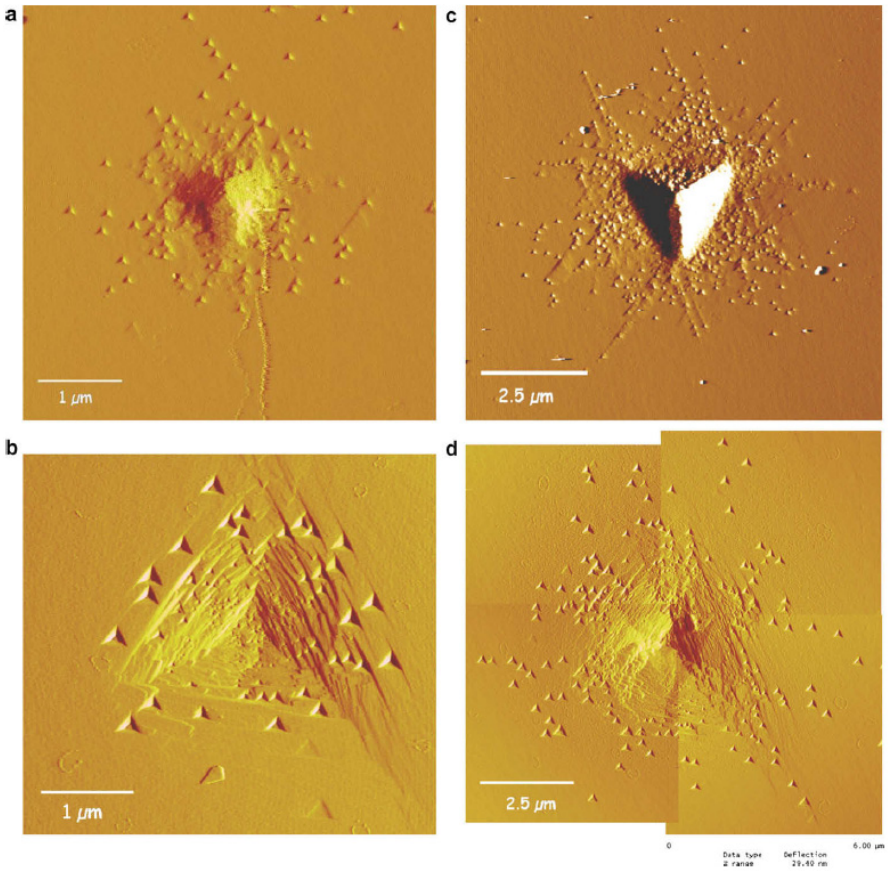

Fig. 2.3.4: AFM deflection mode images of indentations with a load of (a) 1 mN and (c) 5 mN before (a and c) and after polishing (b and d) [27]

They observed three-folded symmetry of etch-pits in (111) oriented CaF_2. At the surface, inside contact area no etch-pits are visible (Fig. 2.3.4 a & c), however, after polishing inside contact area, dislocation can be easily identified. For polished indentations, they reported a clear dislocation structure observation with a dislocation spacing below 50 nm. They quantified the dislocations for 1 mN and 5 mN indentations load at indentation depths of 110 nm and 300 nm, respectively, and estimated the dislocation densities as high as ~ 5 x 10^{+14} m^{-2} (Fig. 2.3.5). At these particular depths, they reported ~3 times higher dislocation densities for 1 mN compared to 5 mN. Moreover, the increase in dislocation density was, according to the Taylor dislocation hardening with a hardness increase by a factor of 1.73.

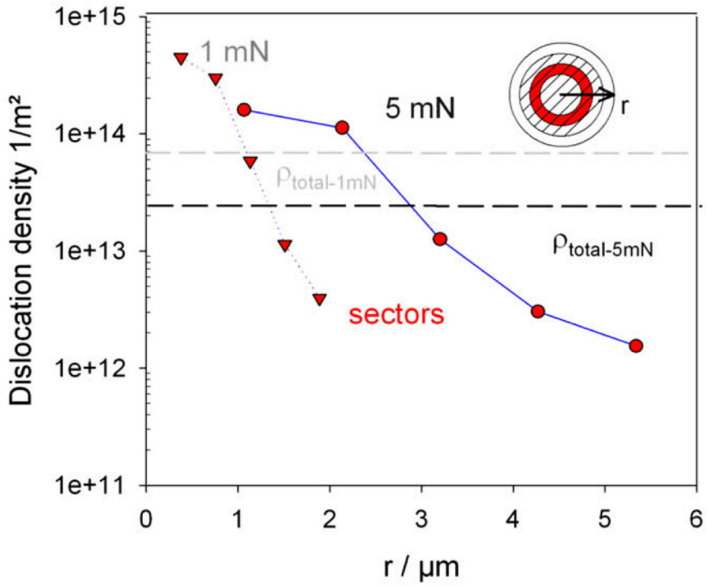

Fig. 2.3.5: Analysis of dislocation structure around 1 mN and 5 mN indentations: Shown is the total dislocation density as well as dislocation density in different sectors [27]

They further applied the modified Nix-Gao model to the measured dislocation densities by considering high frictional stress in CaF_2. However, without considering frictional stress in ISE modelling, the dislocation densities were found to be ~ 10 times higher compared to the measured values. Tromas et al. [29] used the similar etching technique named as "nano-etching" to study the dislocation structure and the effect of pre-existing dislocations on pop-in in (001) MgO single crystal. They further applied nano-etching technique to investigate the dislocation pile-up nucleated on {110} planes, after low-load spherical indentation [93] as shown in Fig. 2.3.6.

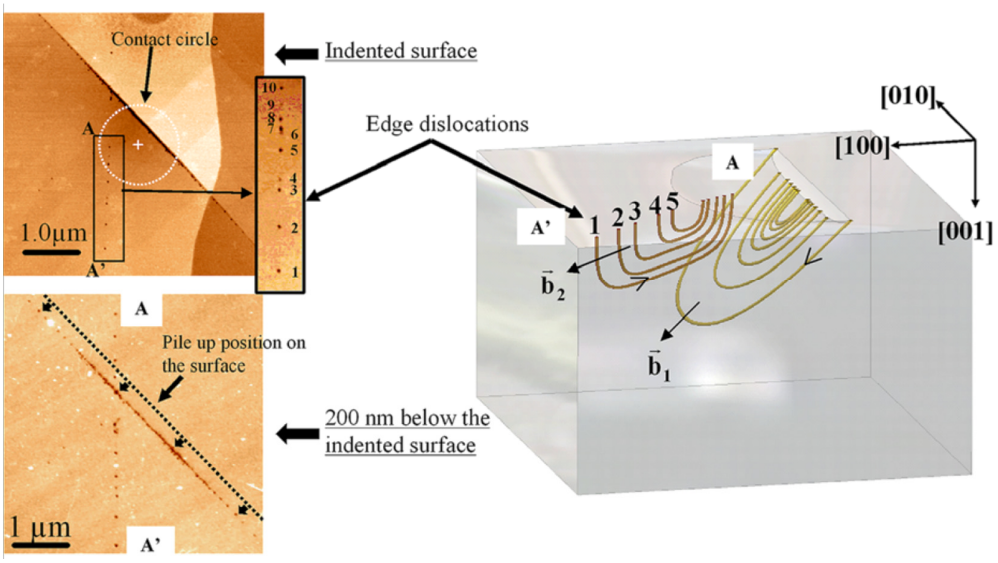

Fig. 2.3.6: Nano-etching patterns obtained around spherical indentation stopped after first pop-in at surface and after polishing at depth of 200 nm relative to the initial surface along with schematic of dislocation loops [93]

These dislocation pile-ups nucleated along six <110>{110} slip systems. Two of six planes were perpendicular to the (001) surface and four were inclined to 45° from the cleavage plane. From quantitative analysis of these dislocation pile-ups, they proposed a model for the estimation of frictional stress. This model was based upon the calculation of Peach-Koehler force induced by the pile-ups and the spherical indenter stress field, which has been used to determine the equilibrium positions of dislocations in these pile-ups. The unloading during indentation results in a dislocation spacing which is representative of the balance between the frictional stress, dislocation-dislocation interaction and residual stress field of the indenter. In the case of equilibrium, shear stresses acting on dislocations in such a pile-up are given by:

$$\tau_a - \tau_f + \tau_d + \tau_{im} = 0, \qquad \textit{(Eq. 2.3.1)}$$

here, τ_a is the applied shear stress from the indentation, τ_f is the lattice frictional stress, τ_d are dislocation-dislocation interaction stresses, and τ_{im} are image stresses. The shear stress resulting from dislocation stress field interactions, τ_d, is given by [94]:

$$\tau_d = \frac{Gb}{2\pi}\sum_{i\neq j}^{N}\frac{A(\psi)}{r_i - r_j}\,, \qquad \textit{(Eq. 2.3.2)}$$

where N is the number of dislocations in the etch-pit arm, b is the Burgers vector, G is the shear modulus, r is the radial distance from the center of the indent to dislocation position

and A(ψ) is equal to 1 for screw dislocations and (1 / 1 - ν) for edge dislocations with Poisson's ratio, ν. They calculated the applied load using Hanson and Johnson model [95]. Moreover, they found that the image stresses along {110} planes are zero and do not modify the positions of dislocations in the pile-ups. Finally, knowing the values of τ_a and τ_d can provide the frictional stress as given:

$$\tau_a(x_i) - \tau_f + \frac{Gb}{2\pi}\sum_{i\neq j}^{N}\frac{A(\psi)}{r_i - r_j} = 0 \qquad \textit{(Eq. 2.3.3)}$$

The lattice frictional stress in MgO was calculated to 65 MPa and 86 MPa for the edge and screw dislocations, respectively. These studies showed that the nanoindentation tests combined with chemical etching and advanced characterization technique like AFM are not only useful to determine the local mechanical properties, but also for the study of elementary mechanisms involved in local plasticity.

2.3.2 EBSD and HR-EBSD

The Electron Backscatter Diffraction (EBSD) also known as Backscatter Kikuchi Diffractions (BKD) is an SEM based technique used to obtain the quantitative microstructural information about the crystallographic nature in a wide range of materials including metals, minerals, semiconductors and ceramic materials. It allows to study individual grain orientation, texture, grain boundary character, grain size and phase identification. Kikuchi et al. [96] in 1928 were the first to observe the diffraction pattern in backscattering mode on a cleavage face of calcite. In 1992, Lassen et al. [97] used the Hough transform [98] to identify the Kikuchi bands in EBSD patterns, which was a major breakthrough in the utility of this technique. The present state of the art fully automated EBSD systems would not be available without this automatic ability to detect the Kikuchi bands reliably. Experimentally, EBSD is conducted inside a SEM equipped with an EBSD detector, which consists of an electron sensitive screen (phosphor or scintillator). The EBSD detector is placed in front of the specimen, which is tilted ~ 70° to the normal of the incident electron beam as shown schematically in Fig. 2.3.7.

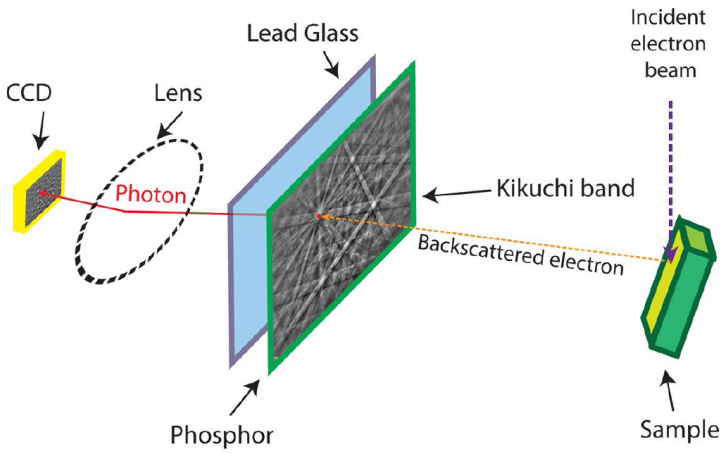

Fig. 2.3.7: Schematic diagram of EBSD pattern formation [99]

The incident beam of electrons is diffracted by the lattice planes in a specimen and forms the EBSD pattern. Each Kikuchi band corresponds to a family of crystallographic planes with the distinct width in a sampled volume and the intersection of bands is known as a pole or zone axis. A digital camera is used to acquire an image of the diffraction pattern formed by the backscattered electrons. Each Kikuchi pattern is indexed by the software using a Hough transform, which is an image processing algorithm to facilitate the detection of lines inside an image. The algorithm converts a line in the image space into a point in Hough space as shown in Fig. 2.3.8.

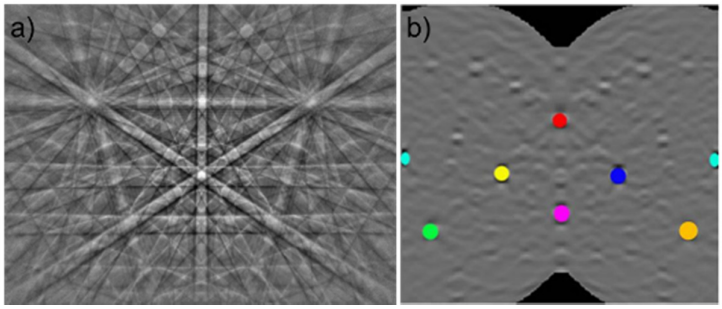

Fig. 2.3.8: EBSD pattern collected from silica (a) along with corresponding Hough transform map (b) [100]

Nanoindentation in conjunction with EBSD, Focused Ion Beam (FIB) milling and corresponding simulations emerged as a powerful tool to reveal the three-dimensional dislocation microstructure at the local scale and understand the underlying deformation mechanisms. For example, Zaafarani et al. [101] used this 3D EBSD technique along with crystal plasticity finite element modeling (CPFEM) to investigate the texture and

microstructure below the nano-indent in Cu single crystals and found significant lattice rotations underneath the indentations as shown in Fig. 2.3.9.

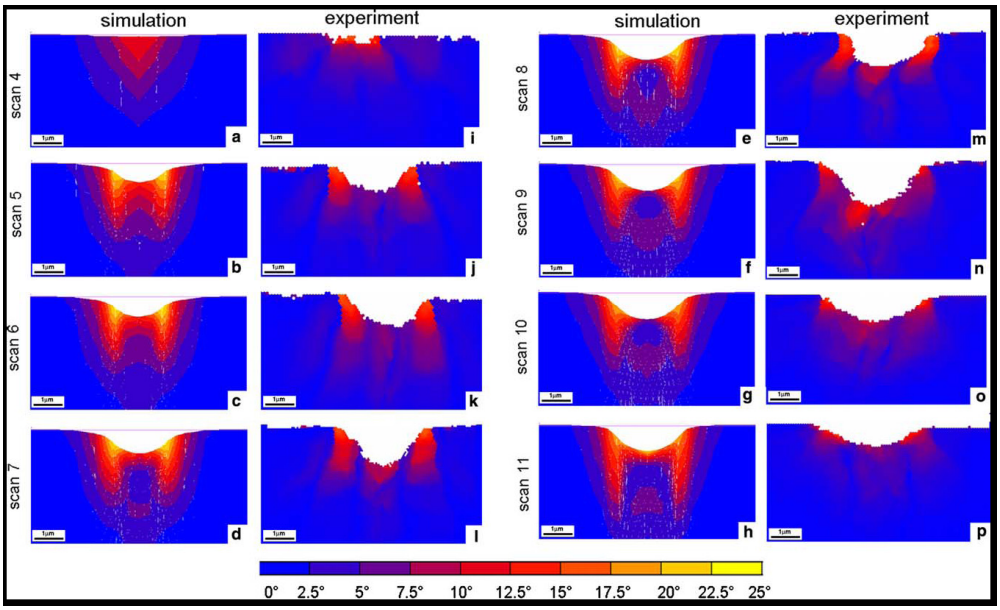

Fig. 2.3.9: Rotation maps for set of successive sections perpendicular to (111) indentation plane with different spacing to the actual indent. Scan 4 is far away from the indenter tip (1567 nm), while scan 10 is close to it (176 nm) [101]

Demir et al. [34] later used EBSD tomography to measure the GNDs below the spherical nanoindentations in Cu single crystals. An exemplary slice at the central cross-section showing GNDs distribution is shown in Fig. 2.3.10.

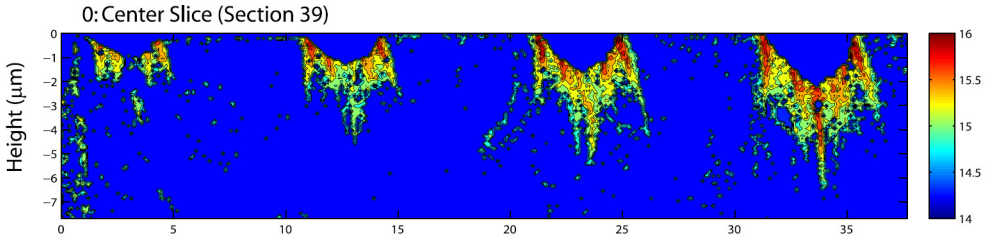

Fig. 2.3.10: GNDs distribution map of four spherical indentations (R = 1 µm) with a maximum load of 4 mN, 6 mN, 8 mN and 10 mN at central slice. GND density is decadic logarithmic scale (m^{-2}) [34]

In that work, GND densities were calculated from the measured rotations using dislocation density tensor which connects lattice curvature to GNDs. The noise level for GNDs map (Fig. 2.3.10) was 10^{14} m^{-2} for a step size of 100 nm. However, there are issues concerning the ability to align correctly the data sets taken after FIB machining, which involved significant

translation and reorientation of the sample. Moreover, if elastic strains were to be included, then account would have to be taken of stress relaxation during the successive removal of material [102]. In the literature, there have been several similar attempts to use the Hough-based analysis of EBSD to provide the orientation gradients and Nye's framework to determine the GND densities. From this conventional Hough-based EBSD measurements, the absolute accuracy of ~ 2° [40] and relative orientation misorientation can be determined to a sensitivity of ~ 0.5° [103], which is less sensitive to determine the GND density and leads to problems like a higher noise level that mask many important features in the dislocation structure.

Recently, Wilkinson et al. have developed the cross-correlation-based analysis of EBSD patterns (named as HR-EBSD), which allows to measure elastic strains and lattice rotations at a sensitivity of about 10^{-4} [39]. In the HR-EBSD analysis, the first step is to save all EBSD patterns at the full resolution of the CCD camera to obtain the highest strain sensitivity during a regular EBSD scan. HR-EBSD measures the shift in the position of zone axes and other features in the EBSD pattern (caused by elastic strains or lattice rotation) between a reference pattern (usually from a strain free region) and the region of interest (ROI), which are the patterns in the data set (i.e., line scan or map) as illustrated in Fig. 2.3.11. The cross-correlation functions are used to determine these shifts via Fourier domain, which applies a bandpass filter and removes high-frequency noise along with low-frequency background intensity variations. The software automatically repeats the cross-correlation between the reference patterns and all ROI, which used to calculate the elastic strains and lattice rotation changes.

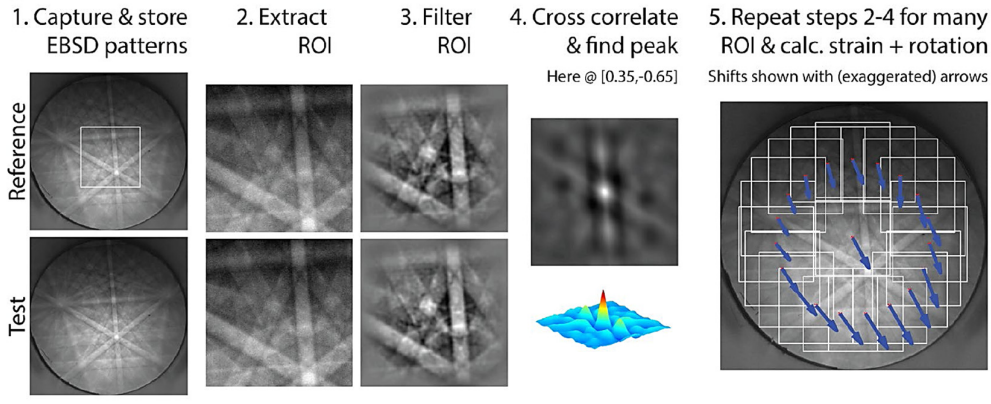

Fig. 2.3.11: Schematic outline of high-resolution cross-correlation based analysis [40]

This cross-correlation based technique has been successfully employed to study the strain state and lattice rotation gradient in a wide range of materials, which demonstrate its

potency to use in a variety of applications, e.g., analysis of strain state ahead of micro-crack in germanium, measurement of elastic strains in brittle materials [104-105], evolution of residual plastic strain in rolled titanium and measurement of lattice rotation gradient / elastic strains in the locally deformed materials (e.g. indents) [102-106]. Fig. 2.3.12 shows an analysis of lattice rotation and strains around an indentation impression in (001) oriented silicon. The peak height and mean angular error (MAE) maps describe the quality of cross-correlation results (Fig. 2.3.12A).

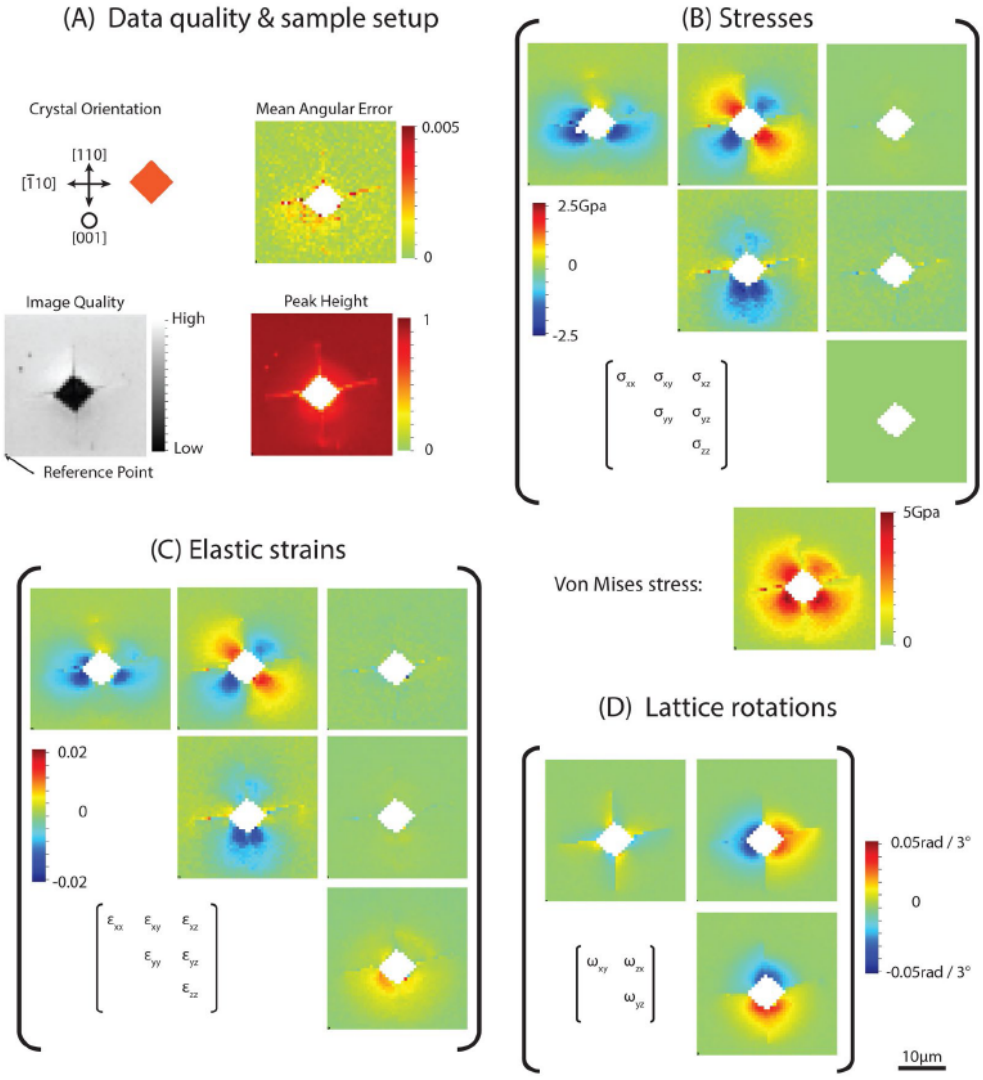

Fig. 2.3.12: Analysis of deformation around an indentation impression in Silicon [40]

The peak height is normalized to "1" for autocorrelation and decreases to zero for poor correlation. The lower value of peak height (typically < 0.3) indicates a poor measurement and should be discarded. MAE describes the difference between the best-fit solutions, from using

more than four ROIs, with the measurements of a pattern shift at each ROI. A MAE value larger than the measured strain or lattice rotation depicts an improper measurement and should not be considered for further evaluation. Fig. 2.3.12 (B and C) shows the elastic stresses and strains measured using Hook's law. The failure stress for silicon is ~ 7 GPa, so, the reported magnitude of stresses seems reasonable. Fig. 2.3.12D illustrate the lattice rotation around the residual impressions with some discontinuity due to the presence of cracks in <110> direction. Wilkinson et al. [107] measured the GND density distribution near the 500 nm deep Berkovich indent in a large grained Fe sample using HR-EBSD and compared it with conventional Hough-based EBSD measurements as shown in Fig. 2.3.13.

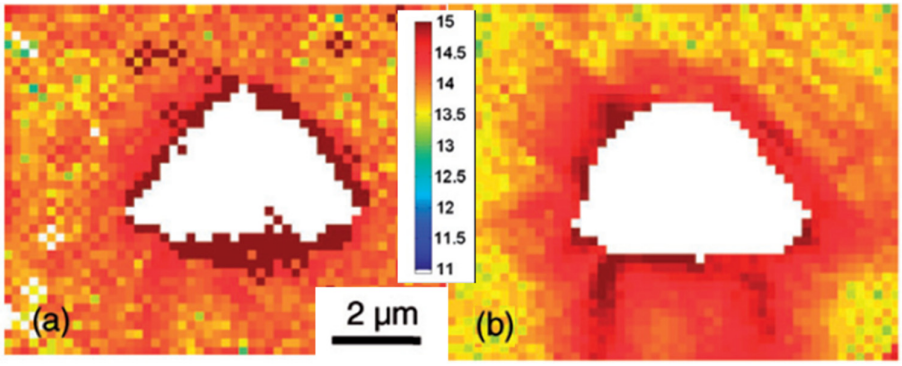

Fig. 2.3.13: GND density distribution map around the indent, (a) Hough-based rotation fields (b) Cross-correlation based rotational fields [107]

Fig. 2.3.13 (a) shows the GNDs distribution map obtained using Hough-based analysis of lattice rotation field. Due to the high noise level (~ 2 x 10^{14} m^{-2}), the GNDs distribution around the residual impression is difficult to recognize. On the other hand, the cross-correlation based analysis (Fig. 2.3.13 b), exhibit a reduced noise level (~ 2 x 10^{12} m^{-2}) and allow to discern the obvious GND structure. He et al. [108] also used HR-EBSD along with nanoindentation to determine the residual elastic stress-strain fields and GNDs distribution around nano-indentation made in α and β phase of TA15 titanium alloy. Recently, Vaudin et al. [109] analyzed the surface uplift surrounding wedge shape indentations in (001) Si using HR-EBSD and AFM. They found remarkable quantitative agreement between both techniques when the derivative of the AFM height field was compared with EBSD displacement gradient tensor. Moreover, it confirms the ability of cross-correlation based EBSD analysis to determine the displacement gradient tensor coefficient with a precision of 10^{-4}.

Despite of these aforementioned HR-EBSD studies equipped with nanoindentation experiments, the potential of this unique combination is further extended in the present work

using sequential polishing and etching technique. The HR-EBSD measurements on the cross sections obtained from underneath the indentations using SPET can provide complete sets of information on GNDs distribution and elastic strain fields compared to the FIB based cross-sections, which have a relatively small area for evaluation (Fig. 2.3.10). Moreover, the dislocation quantification of GNDs and dislocation etch-pit maps on SPET obtained cross-sections can provide a better understanding of ISE, which will be discussed in section 4.2.

2.4 Mechanical Behavior of STO

In crystalline material, the dislocation motion is the most important mechanism of plastic deformation. However, deformation of ceramics via dislocations is not extensively studied due to lower mobility of dislocations in ceramics compared to metals. For any application, the knowledge of the mechanical properties like yield strength (depicting elastic to plastic transition of material), ultimate tensile strength (indicating maximum stress a material carries) and fracture toughness (describes the ability of a material containing a crack to resist fracture) are of prime importance for both ceramics and metallic materials. Moreover, the local crystal defects (dislocations, stacking faults) strongly influenced the desired electronic, optical, magnetic and mechanical properties of materials. In single crystalline form, the dislocation studies played an important role in developing an understanding of dislocation theory which can be further used for different applications.

In contrast to other ceramics, STO deformed plastically at room temperature and exhibits very peculiar ductile-to-brittle-to-ductile transition (DBDT) behavior as briefly mentioned in introduction part. Due to its stable cubic structure and unusual DBDT behavior, mechanical properties of this perovskite material have drawn increased interest. Therefore, STO has been studied extensively in a wide range of temperature via uniaxial compression testing. Recently, the small scale properties in STO have become the renewed center of attention in certain electronic fields due to its potential for implementation as a resistive switching memory and filaments of oxygen vacancies which is possibly related to dislocations. However, only a few small-scale behavior studies have been done in STO which will be reviewed in the proceeding sections along with uniaxial compression testing. Since in the present thesis, indentations have been performed in regime A (correspond to the temperature range of room temperature to 1053 K), therefore, the literature review will be focused on the major experimental findings in this regime.

2.4.1 *Bulk Mechanical Behavior of (001) oriented STO*

In the last two decades, the stress – strain behavior of STO under uniaxial compression testing has been extensively studied by several authors. Recently, Patterson et al. [23] reported the temperature-dependent deformation and dislocation density in (001) STO single crystal via uniaxial compression testing and ex-situ X-ray diffraction rocking curve technique. In that work and the present study, the same (001) STO single crystals are used. Therefore, the results from this particular research are most relevant and important. Fig. 2.4.1 illustrate the resulting stress – strain curves for three consecutive 0.4% plastic strain steps resulting in a total of 1 % to 1.1% plastic strain as a function of temperature.

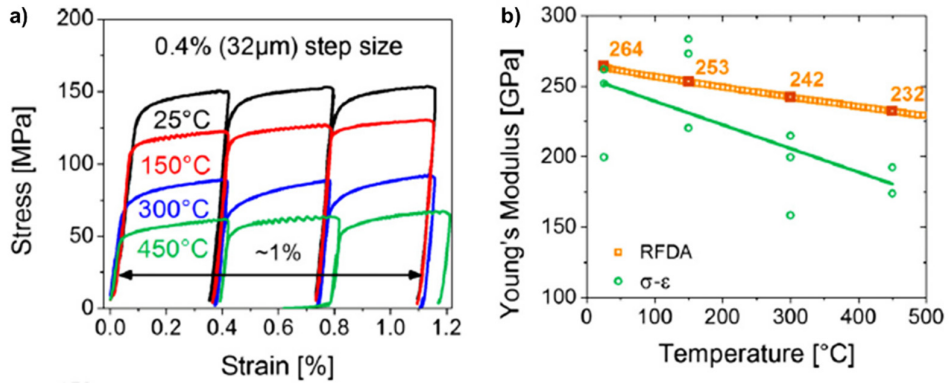

Fig. 2.4.1: Stress – strain curves (a), Young's modulus calculated from stress – strain curves and RFDA measurements (b) for [100] growth direction aligned crystals for ~ 1 % total plastic strain as a function of temperature [23]

With the increase in temperature, the yield strength and Young's modulus decrease significantly, as illustrated in Fig. 2.4.1. The yield strength dropped by a factor of ~ 3 from an average value of 123 MPa at 25 °C to only 46 MPa at 450 ° C. Several other uniaxial compression experimental studies [18-20, 22] show decrease in flow stress with an increase in temperature in regime A. Patterson et al. further measured the average Young's modulus initially from the slope of linear elastic regions and values found to be decreased from 238 to 183 GPa as temperature increased from 25 °C to 450 °C, respectively. They determined Young's modulus additionally via nondestructive resonant frequency and damping amplifier technique (RFDA). The Young's modulus from RFDA technique was determined to be 264 GPa at 25 °C and linearly decreased to 232 GPa at 450 °C, which is ~ 40 – 60 GPa higher than the E values obtained from stress-strain curves (Fig. 2.4.1b). Yang et al. [25] and Bernard et al. [3] determined the elastic modulus ~ 228 GPa from the slope of elastic region and nanoindentation experiments, respectively, which matches well with lower averaged value of

238 GPa measured from similar stress – strain curve slope method. However, the RFDA Young's modulus values were found higher compared to earlier work on elastic properties.

For 1 % deformed specimen, Patterson et al. reported an increase in dislocation density at 300 °C compared to room temperature. Fig. 2.4.2 shows polarized light microscopy images, which revealed a qualitative increase in density and homogeneous distribution of birefringence lines for sample deformed at 300 °C compared to 25 °C.

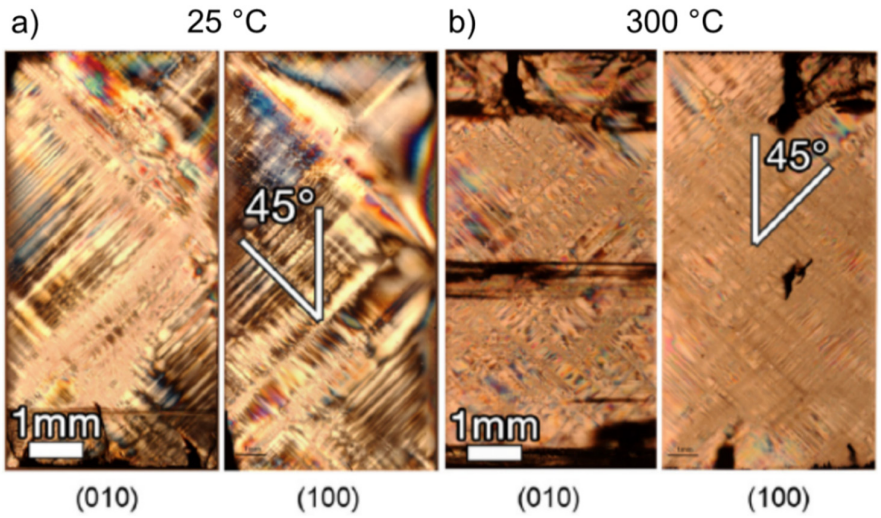

Fig. 2.4.2: Polarized light microscopy images on the polished (010) and (100) faces for samples deformed to 1 % total plastic strain at (a) 25 °C and (b) 200 °C [23]

They further confirmed the increase in dislocation density via nondestructive XRD rocking curve experiments. The dislocation density for 25 °C and 300 °C STO crystals was determined to be 7.9 x 10^{12} m^{-2} and 1.4 x 10^{13} m^{-2}, respectively, which was ~ 4 times higher compared to the specimen deformed at 300 °C. The polarized microscopy images further demonstrate that the $1\bar{1}0$ dislocations glide planes are clearly oriented 45° to the compression direction along <110> directions. These glide planes can be observed by looking through the (010) and (100) faces of crystals, which proved four activated slip systems. For regime A, Taeri et al. [22] also reported the dislocation mobility along four (011), (101), $(1\bar{1}0)$ and $(\bar{1}01)$ planes. Taeri et al. further investigated the plastic behavior of STO for <100>, <110>, <211> and <543> compression axis in the temperature range from room temperature to 1800 K. They found that the STO exhibit a strong anisotropic behavior in regime A, as shown in Fig. 2.4.3.

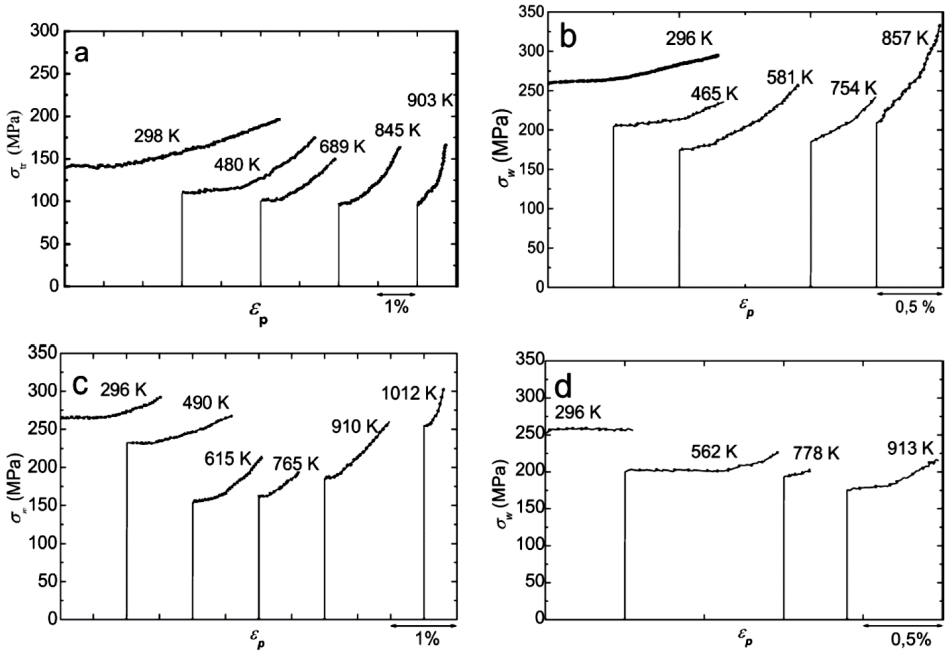

Fig. 2.4.3: Stress – strain curves of samples deformed within regime A, along compression axes (a) <100>, (b) <110>, (c) <211> and (d) <543> [22]

For different investigated orientations in regime A, the surprising, remarkable ductility at room temperature can be observed clearly (Fig. 2.4.3). However, for <100> compression axis, the yield stress is ~ 2 times lower compared to other compression axis at room temperature. For a better physical interpretation of results, a graph of critical resolved shear stress (CRSS) indicated by τ_o and the fracture stress (τ_{fr}) as a function of temperature for different orientation of compression axis is shown in Fig. 2.4.4.

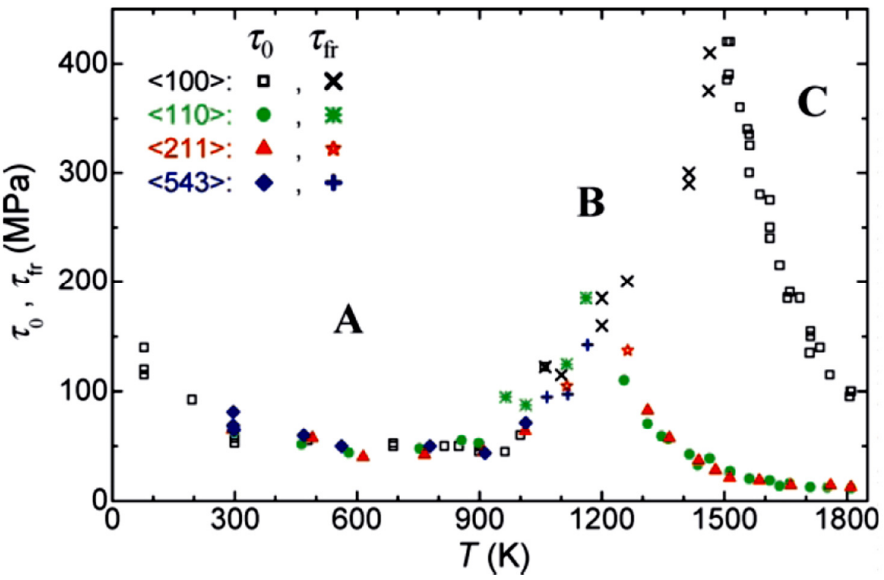

Fig. 2.4.4: Critical resolved shear stress and the fracture stress as a function of temperature for different orientations of the compression axis [22]

Irrespective of the orientation of the compression axis in regime A, the CRSS decreases slowly with increasing temperature up to 600 K where it approaches an almost constant stress value of ~ 50 MPa. In regime B, which depicts the ductile to brittle transition, increase in CRSS and fracture stress can be seen for all orientations of compression axis. However, in Regime C, which depicts the brittle to ductile transition, for <100> specimens, the temperature dependence of CRSS is very strong compared to non-<100> specimen. Gumbsch et al. [19] also performed uniaxial compression testing from room temperature to 1800K for <100> and <110> orientation in STO and found a similar trend of DBDT behavior. Both studies (Teari et al. and Gumbsch et al.) confirmed that for the <100> compression axes, slip occurs along ⟨110⟩{110} system at low and high temperatures. However, for compression axis other than <100>, slip occurs along ⟨110⟩{110} system at low temperatures, whereas, at high temperatures ⟨100⟩{110} system dominates.

The significant ductile behavior of STO in regime A is due to mobility of dislocations with <110> Burgers vector. This Burgers vector has a relatively large value of 5.5Å. The experimental observations [22,110] have also indicated that the <110> dislocations tend to dissociate into two collinear partials separated by a stacking fault, which is assumed to be an antiphase boundary (APB) as indicated by the following reaction:

$$<110> \longrightarrow 1/2<110> + APB + 1/2<110>$$

This dissociation reaction is in accordance with the Frank energy criteria, since it leads to lowering of elastic energy. The high-resolution TEM image illustrating the experimental evidence of dissociation dislocation into two partial dislocations with the APB is shown in Fig. 2.4.5.

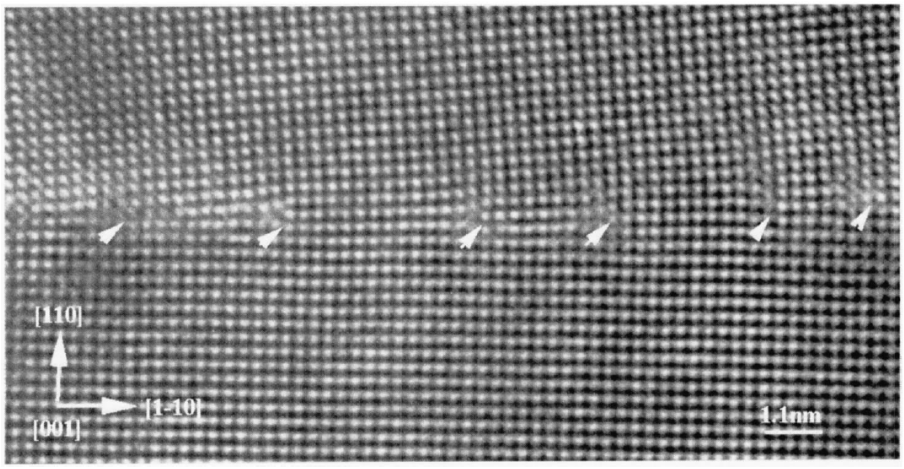

Fig. 2.4.5: HRTEM image illustrating the dissociation of a<110> dislocations into two partials with APB [110]

Castillo-Rodríguez et al. [111] determined the dissociation width between the partial to be 30 – 40 Å. The energetics and structure of this APB have been studied by several authors [112-114] experimentally and theoretically, which attributed a wide range of spectrum value from 0.2 to 1.2 J/m^2. These large APB energies result in very small dissociation distance of 15 – 20 Å, which is significantly smaller than the experimentally obtained HR-TEM observations. This discrepancy between the theoretical and experimental predictions of APB energy remains unanswered for several years. Recently, Hirel et al. [115] performed the atomistic simulation to study the <110> dislocations in STO and resolved this long-standing discrepancy between the theoretical and experimental predictions of APB energy. Hirel et al. modelled the dislocations of screw and edge characters of Burgers vector <110> in STO and show that the screw dislocation dissociated into two collinear partials (Fig. 2.4.6) having a large APB boundary with a quite large 30 – 40 Å dissociation distance, which was in agreement with experimental observations.

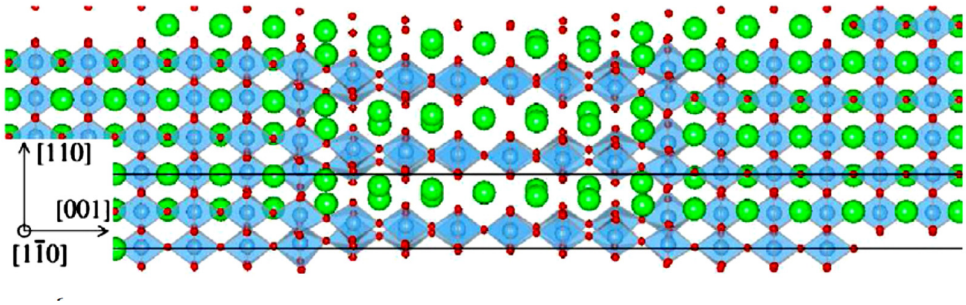

Fig. 2.4.6: The atomic structure of a screw dislocation in STO, the two partial dislocations can be distinguished, but strongly overlapped. The large green spheres are represented as Sr ions, medium dark blue as Ti ions, small red sphere as O ions and TiO_6 octahedra are shown in transparent light blue [115]

They further reported that this surprising result is due to the fact that the partial dislocations minimize their energy by spreading in the glide plane and even overlap, which subsequently increases the overall width of dislocation.

2.4.2 Small Scale Mechanical Behavior of (001) oriented STO

Despite of comprehensive works on bulk single crystal plasticity of STO in a wide range of temperature, using uniaxial compression testing, little is known about the local, small-scale behavior in STO. In the 90s, few TEM studies were conducted at the atomic resolution level to study the dislocation structure at the local scale. Matsunaga et al. [24] conducted Vickers micro-indentations using ~500 mN in (001) STO single crystal at room temperature and identified <110>{110} slip system via TEM analysis. Moreover, in that work, no dislocations with Burgers vector of <100> type were observed.

Nishigaki et al. [116] performed high temperature (900 °C and 1100 °C) spherical indentation experiments on (001) STO single crystal using load ranged from ~ 400 mN to ~ 980 mN via R = 0.6 mm, partially stabilized ZrO_2-Y_2O_3 indenter tip and studied the activated slip systems using TEM analysis. At 900 °C and 1100 °C, they observed all the dislocations with Burgers vector of either <110> or <100> types. Moreover, they reported that both of these types of dislocations were in glide configuration at 900°, whereas, at 1100 °C, <001> dislocations were in the climb configuration along with most of <110> dislocations in glide configuration at 1100 °C.

In early 2000s, after the discovery of unusual DBDT behavior in STO, along with other remarkable properties like stable cubic symmetry above 105.5 K, high dielectric constant and high chemical and thermal stability, made STO a prime candidate for different applications,

e.g., as a substrate with wide range of coating materials including superconductors, dielectric materials in capacitors and for producing different microelectronic heterostructures, which spark new interests in local scale plasticity in STO. Bernard et al. [3] used (001) oriented STO as a substrate for $Pb_{0.9}La_{0.1}TiO_3$ (PLT) and Yttrium Barium Copper Oxide (YBCO) to study the mechanical behavior of ferroelectric thin films on perovskite substrate. Both of coating materials, PLT and YBCO are well-known for their ferroelectric and displaying high-temperature conductivity, respectively. They performed nanoindentation and Vickers micro-indentation experiments to study the local scale mechanical behavior of substrate (STO) and thin films (PLT and YBCO) and reported very valuable results in STO. The Vickers indentations were performed using four loads (150, 300, 500 and 1000 mN). During Vickers indentations, they always observed the cracks propagate along <110> directions and on turning the indenter to 45°, cracks appear at the corners of imprints, whereas at 0° indenter position, the crack appears at random position of imprints as shown in Fig. 2.4.7.

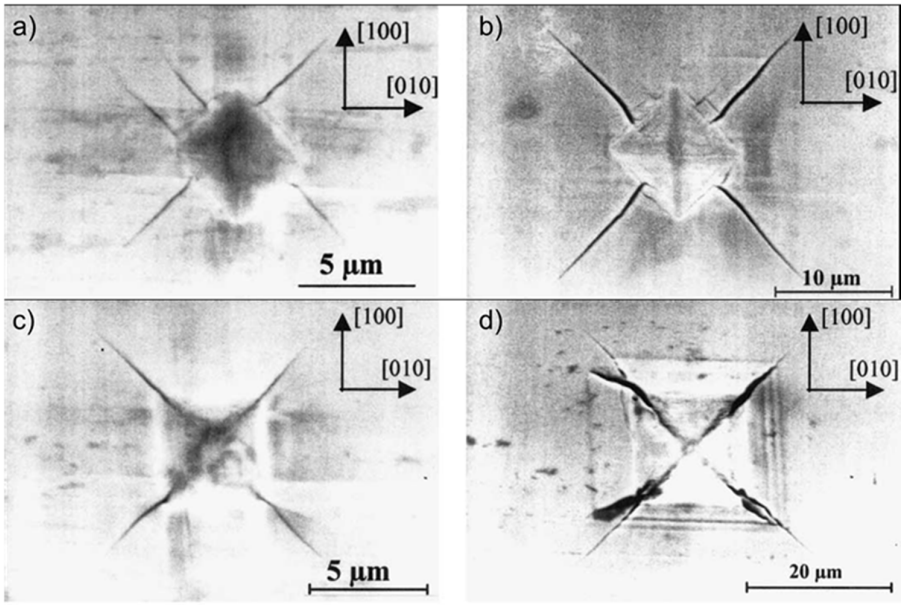

Fig. 2.4.7: Vickers residual impressions on STO: (a) 150 mN, 0° (b) 500 mN, 0° (c) 150 mN, 45° (d) 500 mN, 45° [3]

They calculated the fracture toughness (K_{IC}) STO to be 1 ± 0.1 $MPa.m^{1/2}$ (from the Vickers residual impression and crack length) using Anstis et al. [117] approach. From Vickers micro-indentation experiments, they observed a significant decrease in hardness at higher penetration depths due to cracking as shown in Fig. 2.4.8.

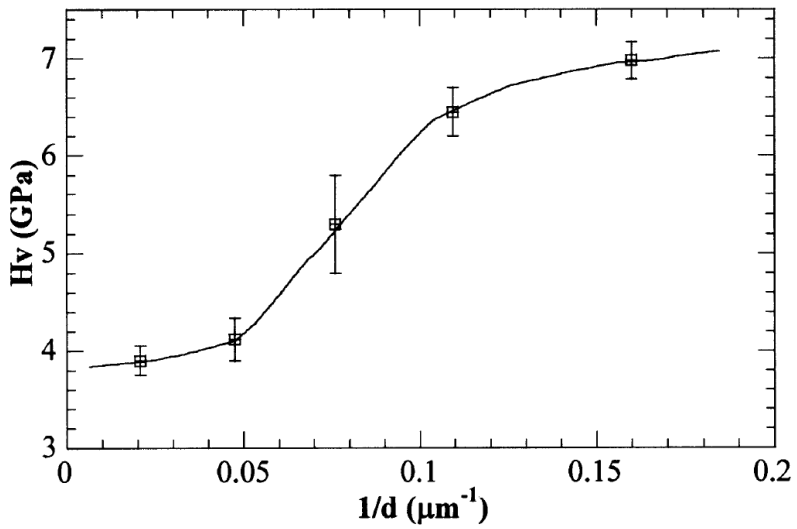

Fig. 2.4.8: Evolution of Vickers micro-hardness in STO single crystal as a function of the load [3]

Bernard et al. suggested that the cracking leads to mechanical relaxation in the material which consequently results in more penetration than expected and the measured hardness is so underestimated. At higher penetration depths, they reported the hardness value of ~ 7.5 GPa. From Berkovich nanoindentation experiments, at lower penetration depths, the hardness and modulus was calculated to be 9.5 ± 1.3 GPa and 225 ± 14 GPa, respectively. Moreover, they observed multiple pop-in events in nanoindentation load-displacement curve as shown in Fig. 2.4.9.

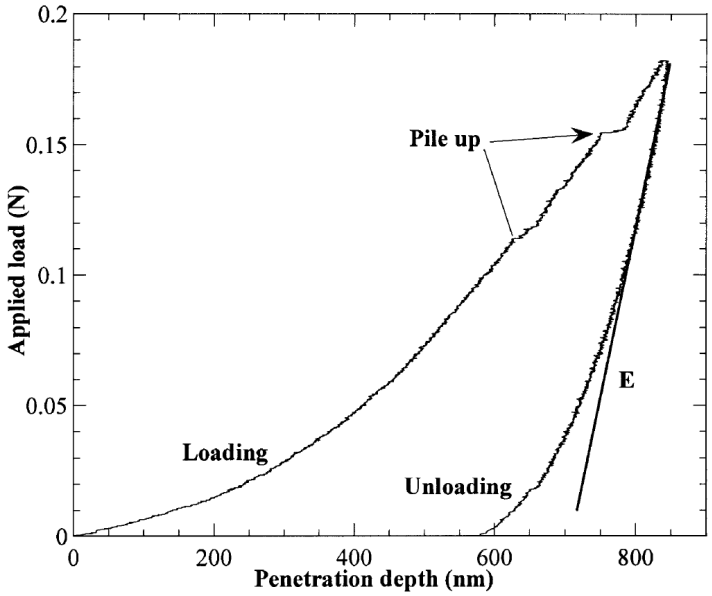

Fig. 2.4.9: Nanoindentation load-displacement curve for (001) STO singly crystal [3]

They relate the occurrence of multiple pop-in events in STO with cracking and observed that the pop-in effect reduced significantly with the superconductor interlayer addition, which shows the better mechanical behavior of PLT/YBCO/CeO_2/STO system. In that work, the nanoindentation data were only evaluated for basic hardness and modulus measurements of the substrate and thin films. Moreover, at smaller indentation depths (i.e., less than 100 nm), where the cracking is absent, the origin of multiple pop-in events still need to study in details.

Yang et al. [25] also studied the activated slip systems and dislocation structure in the vicinity of the crack tip during room temperature Vickers indentation experiments (at maximum load of 100 gf and 1Kgf) in (001) oriented STO single crystal using chemical etching, FIB, SEM and TEM analysis. They reported an additional slip system $\langle 110\rangle\{001\}$ along with the primary slip system $\langle 110\rangle\{1\bar{1}0\}$. This is the only study giving an indication of slip along $\langle 110\rangle\{001\}$ system. Moreover, from TEM analysis they observed (a) the dislocations with edge, screw and mixed character (Fig. 2.4.10a), (b) sessile jogs (D6 in Fig. 2.4.10b), (c) dipole trails, edge, screw and mixed dipoles, (d) decomposition of such dipoles in loops, (e) formation of sub-grain boundaries.

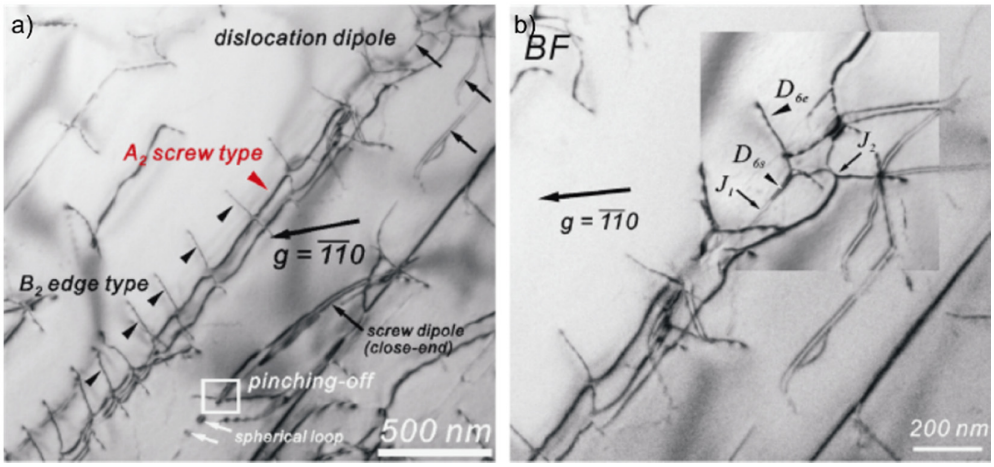

Fig. 2.4.10: Bright-field TEM images (a) screw and edge type dislocation along with dislocations in the framed region forming jogs, (b) screw dipole D6 formed by gliding edge dislocations in its slip plane [25]

Furthermore, TEM analysis on FIB obtained cross-sections close to the crack tip revealed that the dislocations emitted half loops on the (001) planes with a Burgers vector of [011]. They also reported the half-penny crack nature below the indentations and confirmed the fracture toughness of ~ 0.89 MPa.m$^{1/2}$ similar to those calculated by Bernard et al [3].

Recently, Kondo et al. [26], however, reported only ⟨110⟩{1$\bar{1}$0} type slip during in-situ TEM nanoindentation experiments in (001) STO single crystal. Fig. 2.4.11 shows some images captured from the recorded video during nanoindentation experiments under different loading and unloading time intervals. They observed three types of dislocations: Type I, which initially nucleated and propagated in a semi-circle shape and then splits into two segments having ±[100] directions (Fig. 2.4.11a, @14s). Type II and type III dislocations were also nucleated near contact area and moved along [101] and [$\bar{1}$01] directions, respectively (Fig. 2.4.11a, @38 and 57s). Moreover, they clearly observed the annihilation of dislocations of Type I dislocations as shown in Fig. 2.4.11 b.

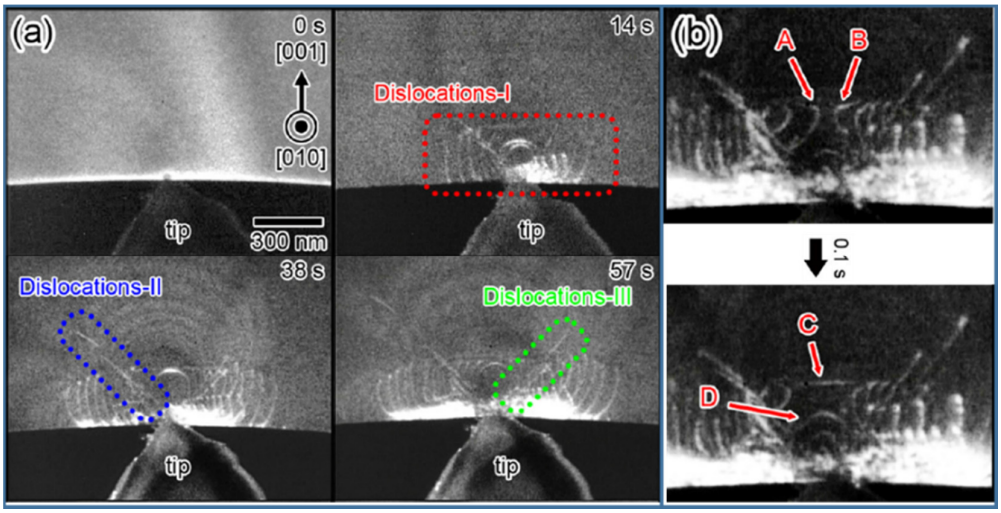

Fig. 2.4.11: Sequential dark-field TEM images captured from the movie recorded during nanoindentation experiments (a) during indenter loading showing Type I, II and III dislocations (b) during indenter unloading showing annihilation of dislocations [26]

The discrepancies in the activated slip system at the local scale and high hardness of 9.5 GPa for a material with a yield stress of ~ 120 MPa (which is still unanswered) show that our knowledge of dislocation structure evolution at small scales and details of dislocation based nanoplasticity in STO is still very limited. Moreover, none of the indentation studies discuss the ISE behavior in STO, which is more pronounced at the local scale. Therefore, in the present work, a comprehensive 3D dislocation structure evolution at local scale have been studied using nanoindentation combined with chemical etching technique, SEM, HR-EBSD and MD simulations.

Chapter 3 Experimental Procedure

3.1 Material

In the present work, un-doped single crystalline (001) oriented STO specimens grown by the Verneuil method were used. The specimens were supplied by Alineason Materials Technology GmbH, Frankfurt am Main, Germany in polished (4-sided) cuboidal form. For room temperature spherical and Berkovich indentations, the specimens dimension were 4 x 4 x 8 mm^3. However, for high-temperature Berkovich indentations, thinner (001) oriented STO single crystals with dimensions of 4 x 2 x 2 mm^3 were used in order to provide a sufficient heating of the surface.

3.2 Estimation of Materials Removal Rate in (001) STO

To study the dislocation structure below the indentation, a desired amount of material should be removed from the surface of the specimen. To estimate the material removal rate of (001) oriented STO, polished and etched STO specimen was first indented and the indentation depth 'h_o' was measured before subsequent polishing using a confocal laser microscope (LEXT 4000, Olympus, Japan) as illustrated in Fig. 3.2.1.

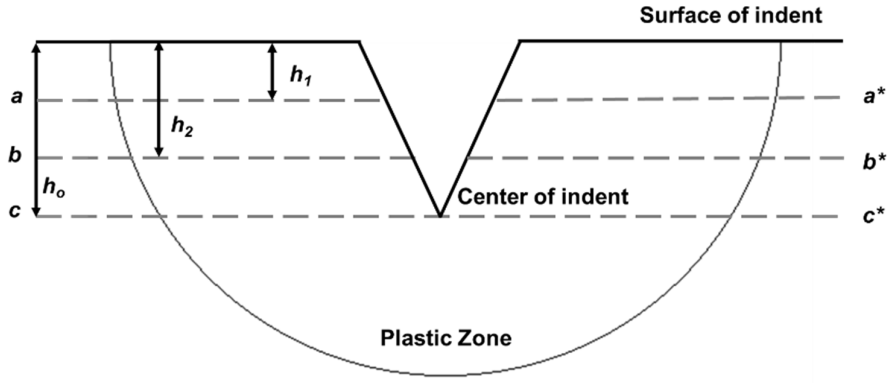

Fig. 3.2.1: Schematic diagram showing different cross-sections along with indentation depths

A vibrational polishing machine from Jean-Wirtz GmbH, Düsseldorf, Germany, was used to remove the required amount of material from the specimen surface via a 40 nm colloidal silica suspension (OPS Struers A/S, Ballerup, Denmark). The STO specimen was polished for

one-hour and the residual impression depth (h_o - h_1) was measured for the same indent, which provides the amount of material removed per hour from the surface of the specimen to cross-section a-a* (Fig. 3.2.1). The specimen was further polished for another hour and the remaining depth (h_o – h_2) was measured at cross-section b-b*. The polishing rate was determined by averaging the amount of material removed per hour. Multiple reference indents were used to confirm the removal rate. The Fig. 3.2.2 shows two 200 gf Vickers indentations performed on the same etched (001) oriented STO single crystal via Zwick micro-hardness tester.

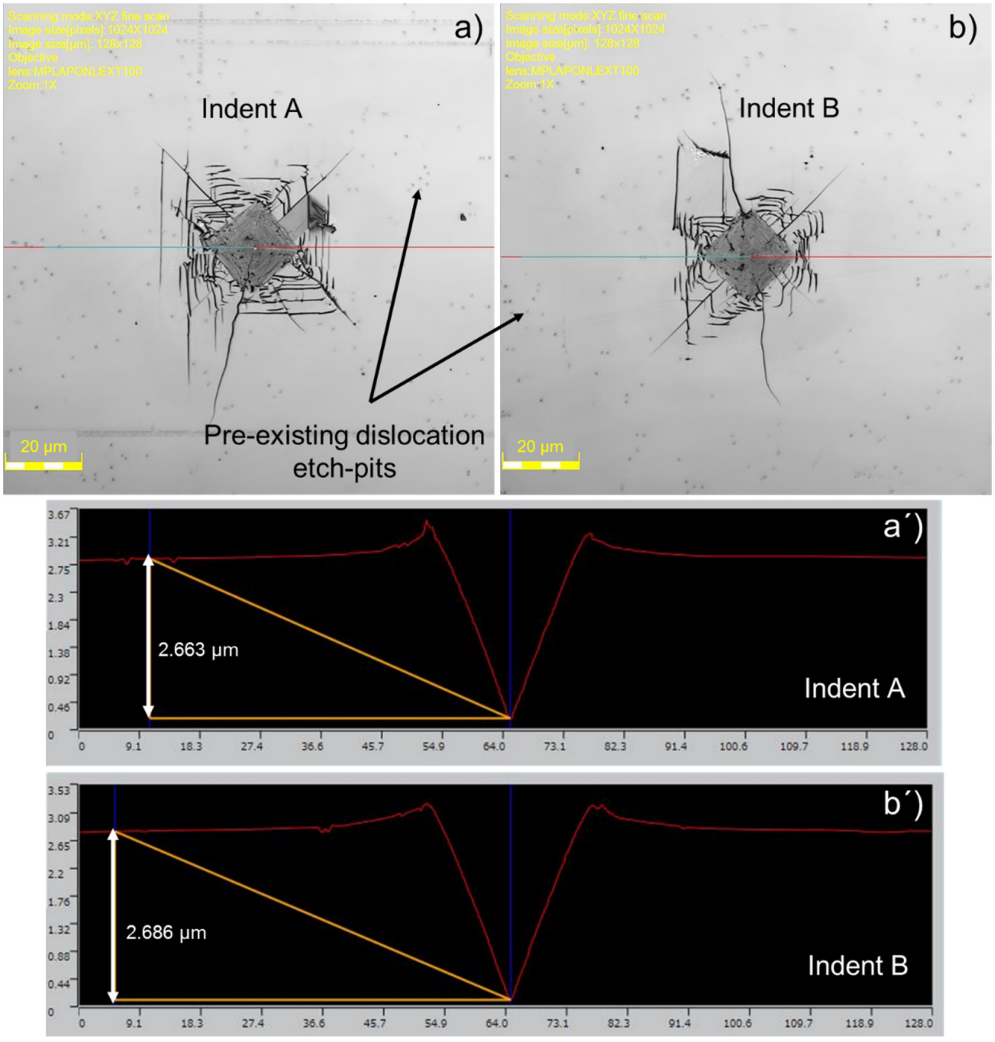

Fig. 3.2.2: 200 gf Vickers indentations along with representative indentation depths before polishing

For Vickers indentations ‘A’ and ‘B’, the indentation depths before polishing (h_o) was measured to be 2.663 µm and 2.686 µm, respectively. The Vickers indentations were polished for one-hour using OPS vibrational polishing and the indentation depths for polished Vickers indents were measured via confocal laser microscope as shown in Fig. 3.2.3.

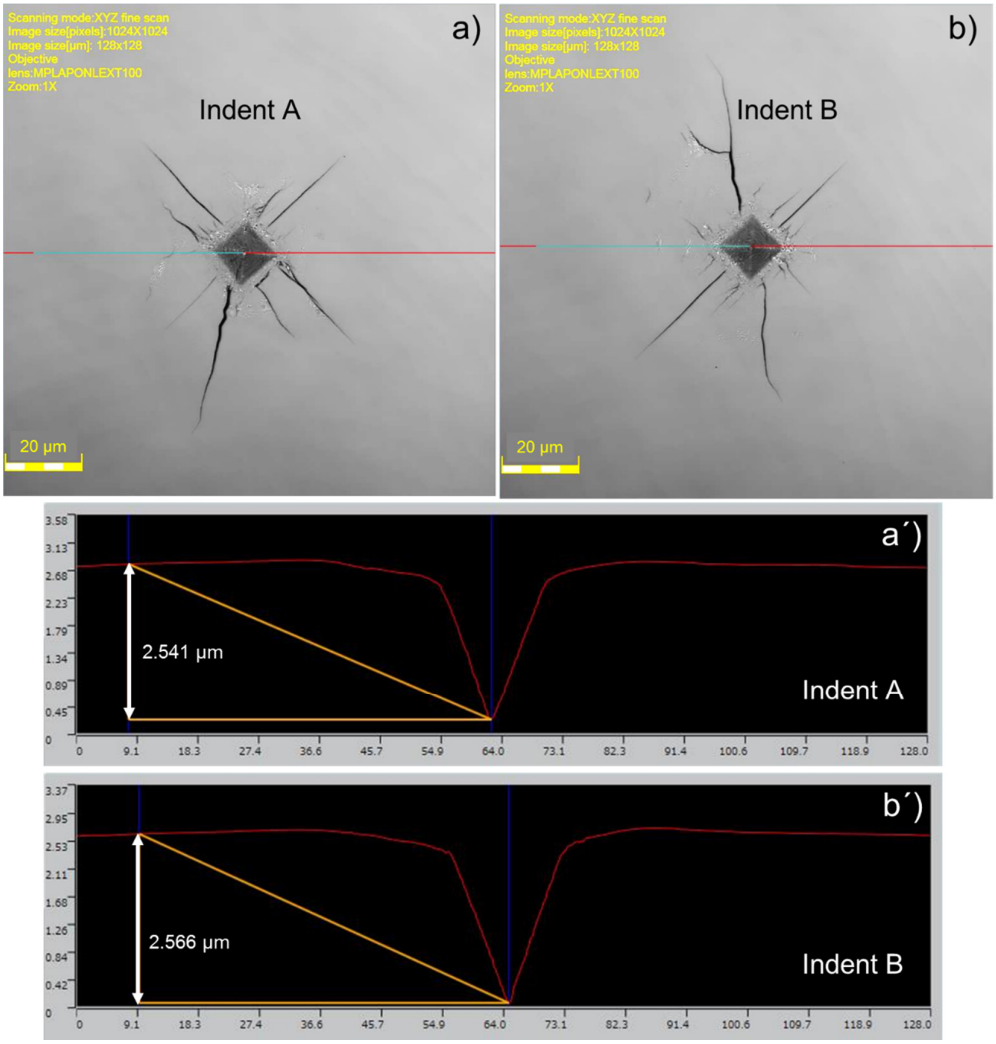

Fig. 3.2.3: 200 gf Vickers indentations along with representative indentation depths after one-hour polishing

After one-hour polishing, the indentation depth for indent 'A' and 'B' was measured to be 2.541 µm and 2.566 µm, respectively. The amount of material removed per hour was calculated by subtracting the measured non-polished and polished indentation depths. For indent 'A' and 'B', it was determined to be 0.122 µm / hour and 0.120 µm / hour, respectively. The same indentations were further polished for another one-hour using OPS vibrational polishing and indentation depths for polished indents were measured using laser microscope as shown in Fig. 3.2.4.

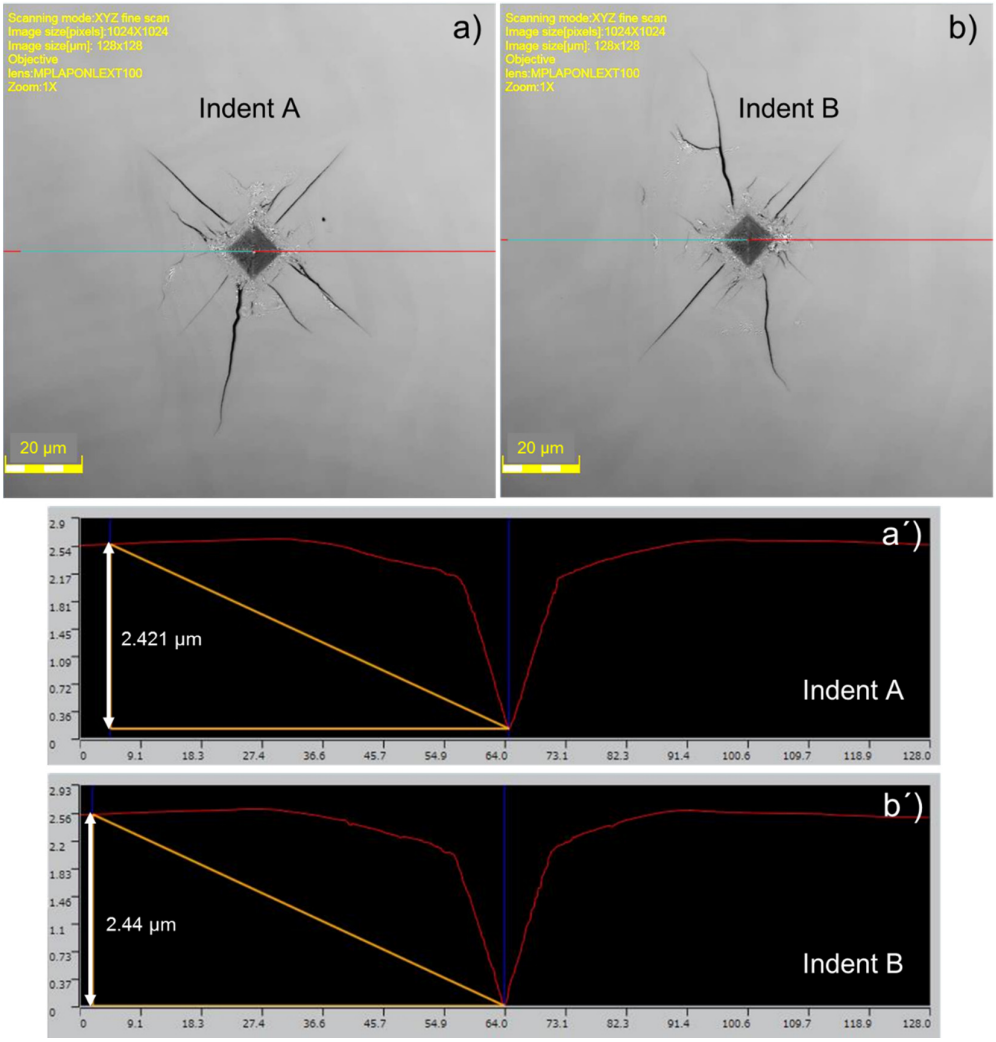

Fig. 3.2.4: 200 gf Vickers indentations along with representative indentation depths after two-hours polishing

After two-hours polishing, the indentation depth for indent 'A' and 'B' was measured to be 2.421 µm and 2.44 µm, respectively. For second polishing, the amount of material removed per hour was determined to be 0.12 µm and 0.126 µm for indent 'A' and 'B', respectively. The polishing rate was thus determined by averaging the removal rate per hour and found to be 0.122 ± 0.003 µm/hour.

The material removal rate was found to be strongly influenced by silica suspension concentration and applied weight. For the present work, a weight of ~900 grams and 4:1 ratio of silica suspension to distilled water were used for vibrational polishing. As Fig. 3.2.1 schematically illustrates that below the center of indent, the plastic zone still exists which requires etching to reveal the dislocation structure below the indentation. From the known

polishing rate, the dislocation structure at any desired depth underneath the indentation can be studied.

3.3 Experimental Protocol

3.3.1 Analysis of Dislocation Structure on the Surface of Specimen

The polished specimens were first etched for the 20s in 10ml 65% HNO_3 with a few drops of 40% HF to reveal pre-existing dislocations. To study the dislocation structure evolution from incipient plasticity to a fully developed plastic zone, the indentation experiments were performed by using Berkovich and spherical indenter tips at different loads (see section 3.5 for details). The indentations were first imaged with a scanning electron microscope (MIRA 3XMH, FEG-SEM, TESCAN, Czech Republic) to observe slip steps on the surface. A confocal laser microscope was further used to measure the indentation depth. After indentations, the dislocation structure within the plastically deformed zone was revealed by re-etching the STO single crystal for 10 to 20 seconds in the same etchant. The second etching step leads to larger etch-pits for the pre-existing dislocations, allowing to distinguish them from the indentation- induced etch-pit pattern as shown in Fig. 3.3.1 for an exemplary 45 mN Berkovich indentation.

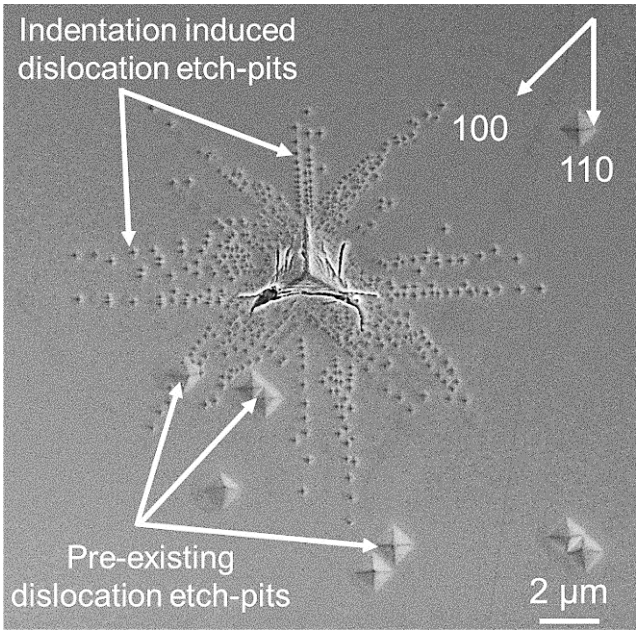

Fig. 3.3.1: Etched SEM Berkovich indentation at 45 mN load showing pre-existing dislocation etch-pits along with indentation-induced etch-pits

A higher etching time (~20 seconds) was used for studying the dislocation shape and tracking the dislocation pile-ups. However, for dislocations quantification, lower etching time (~10 seconds) was used.

3.3.2 Analysis of Dislocation Structure below the Indentation via SPET

Fig. 3.3.2 schematically illustrates the presence of plastic zone below the spherical indentation. To reveal the dislocation structure at desired depth below the indentation (indicated by dotted line in Fig. 3.3.2), vibrational polishing was conducted to remove a certain amount of material from the specimen surface. After reaching desired polishing depth, subsequent etching was done to reveal the dislocation structure. The process of sequential polishing and etching is termed as SPET, which allow to obtain the dislocation structure at any chosen polishing depth.

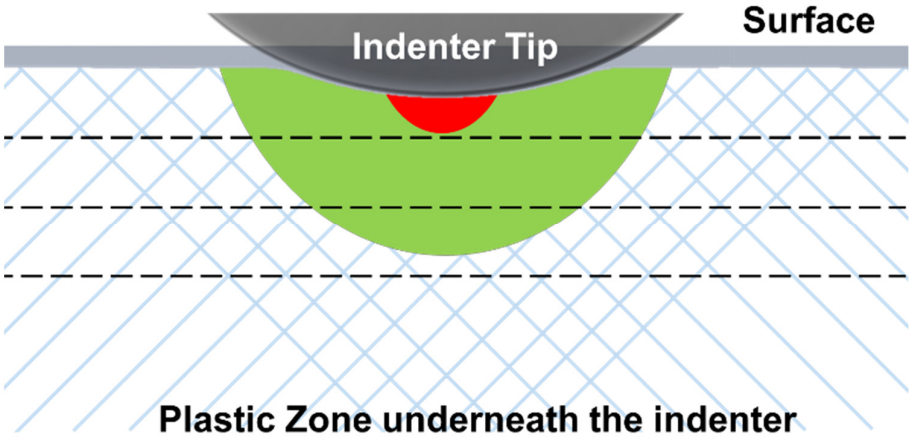

Fig. 3.3.2: Schematic illustration of plastic zone below the indentation where dotted lines depict the desired polishing depths

After imaging the dislocations at that particular polishing depth, further vibrational polishing was performed until next desired polished depth was reached. After each etching step, the specimen should be polished until all the dislocation etch-pits from the previous etching step were no longer visible on the surface, which is the minimum criteria for polishing depth. The whole process was repeated until no etch-pits were observed at the point of contact below the indentation or after obtaining the desired number of cross-sections as shown in Fig. 3.3.3.

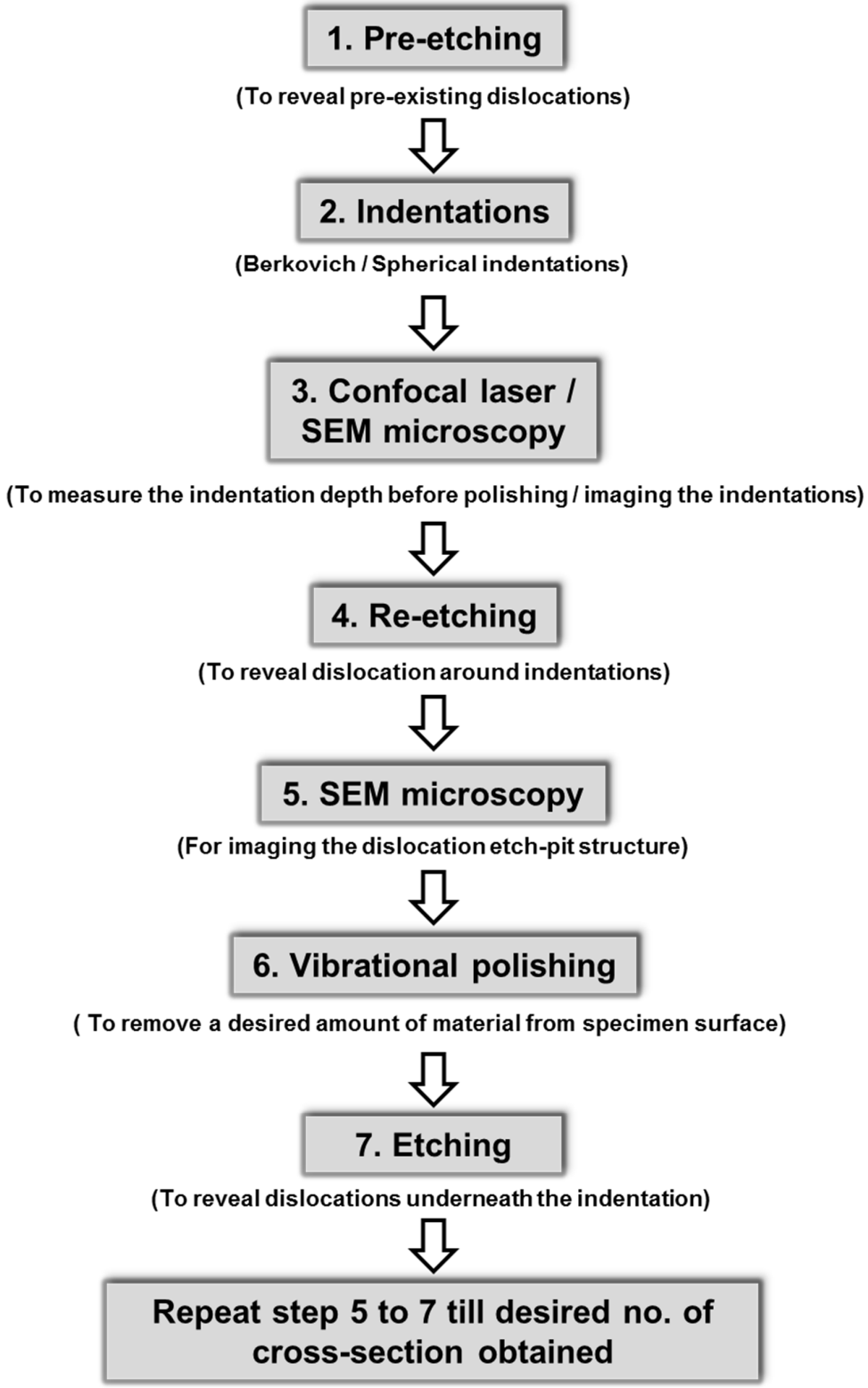

Fig. 3.3.3: Schematic of experimental protocol for 3D dislocation etch-pit structure study

3.4 Dislocation Etch-Pit Quantification

For quantification of dislocation etch-pits, the etched SEM images were digitized by placing a spot at the center of each etch-pit as exemplarily shown for pile-up A in Fig. 3.4.1.

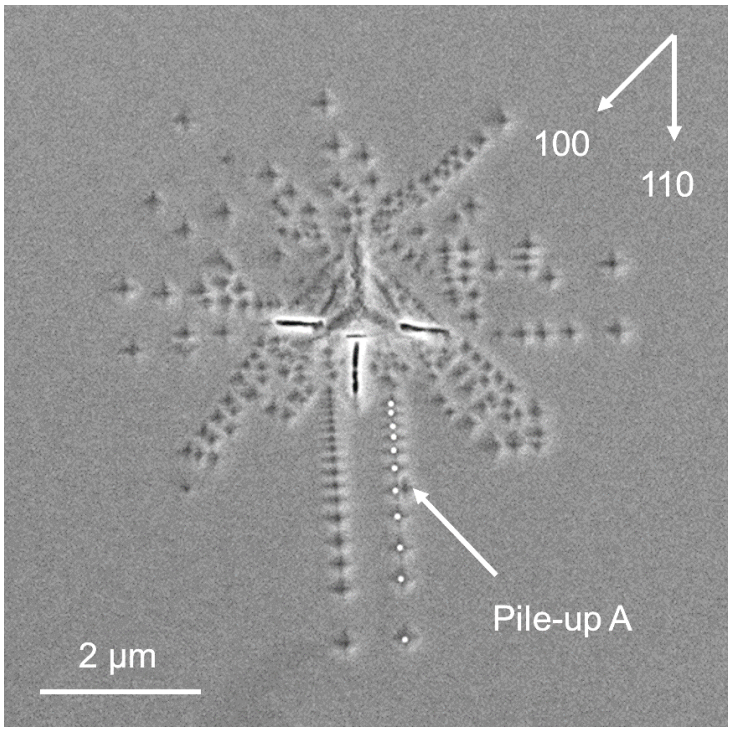

Fig. 3.4.1: Etched SEM Berkovich indentation at 12 mN load

It is also evident from Fig. 3.4.1 that the non-polished, etched indentations show the dislocation etch-pits only around the residual impression and inside the contact area, the etch-pits are invisible. For estimation of lattice frictional stress at room and 350 °C, only dislocation pile-ups were digitized. However, to study the ISE, the specimen was polished and dislocation structure underneath the indentation was digitized as shown in Fig. 3.4.2 for an exemplary polished 25 mN indent. Using digitized image, the dislocation density (defined as the number of etch-pits / digitized points per unit area) were analyzed in circular regions.

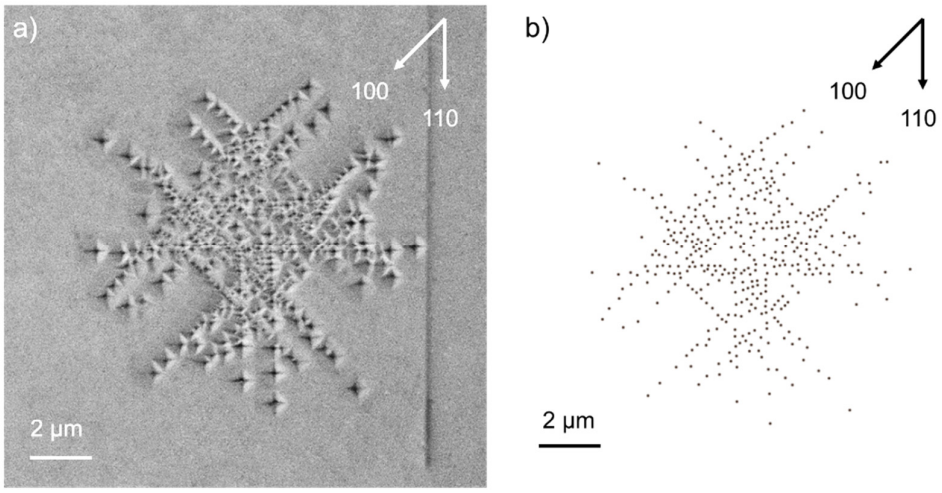

Fig. 3.4.2: Dislocation etch-pit structure underneath (at -1200 nm) the 25 mN Berkovich indentation (a) SEM image (b) Digitized image

3.5 Indentation Experiments

For nanoindentation experiments, two separate instrumented nanoindenters, iNano (Nanomechanics inc., USA) and G200 (Keysight Technologies, USA) were used in the present work. Both nanoindenters are equipped with load controlled (LC) and continuous stiffness measurement (CSM) units. A maximum load of 50 mN and 500 mN can be applied by using iNano and G200 nanoindenter, respectively. However, the iNano has a lesser time constant and better dynamics as compared to G200 nanoindenter, which enables to identify the different events occurring within the material like multiple pop-in events. Therefore, iNano was used for lower load Berkovich indentation experiments. The G200 nanoindenter was further used for room temperature and 350 °C Berkovich indentations. However, the spherical indentation experiments were performed only at room temperature using nanoindenter G200 and Brinell hardness tester (Wolpert Dia Tester2, Germany). The details of these indentation experiments are given below:

3.5.1 Spherical Indentations

The spherical indentation experiments were carried out with a G200 nanoindenter from Keysight Technologies, USA, equipped with diamond spherical indenter tips having radii of 7.5 µm and 25 µm. Based on the Hertzian elastic contact solution, the data before the pop-in event was fit (as shown in Fig. 3.5.1, for an exemplary spherical nanoindentation LD curve) using a power law relationship, $P \alpha h^{3/2}$, and indenter tip radius was calculated using Eq. 2.2.9.

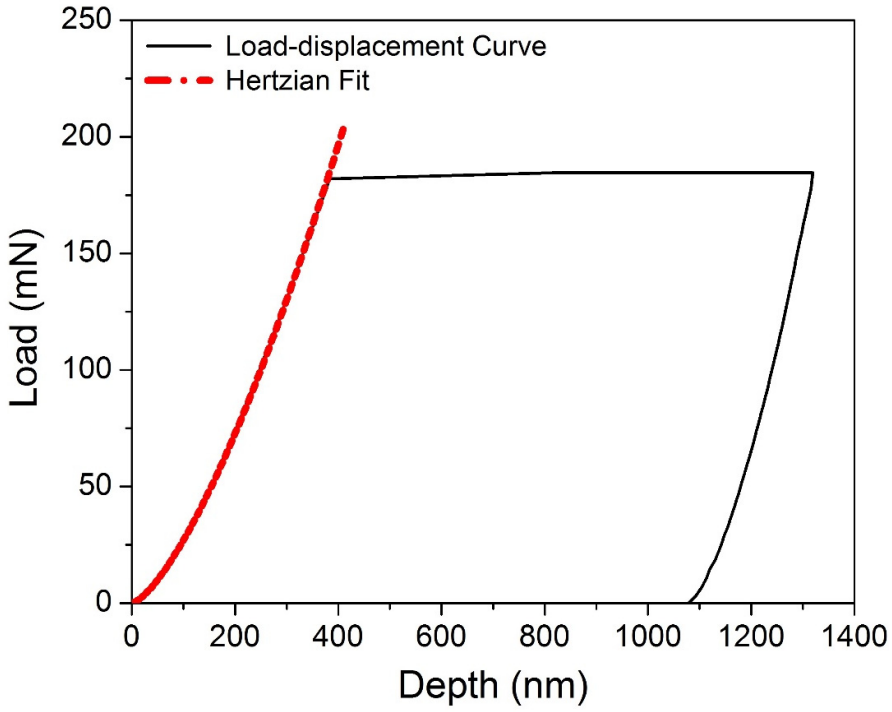

Fig. 3.5.1: Spherical indentation load – displacement curve for R = 7.5 µm along with the Hertzian fit before pop-in event

Maximum loads of 200 mN and 450 mN were applied in 7.5 µm and 25 µm radii ball indentations, respectively. Several nanoindentation experiments were stopped just after the first pop-in (denoting the elastic-to-plastic transition of the material) to study the dislocation structure around indentations at the point of incipient plasticity. Along with nanoindentation experiments, a Brinell hardness tester (Wolpert Dia Tester2, Germany) having a steel tip of 2.5 mm radius was used to study the dislocation structure evolution at lower a/R ratio, where 'a' is the contact radius and 'R' is the tip radius. The 3D dislocation etch-pit structure underneath the indentation was revealed by using the SPET analysis as explained in section 3.2.

3.5.2 Room Temperature Berkovich Indentations

The room temperature Berkovich indentations were performed via two separate instrumented nanoindenters, iNano (Nanomechanics inc., USA) and G200 (Keysight Technologies, USA) using the diamond indenter Berkovich tip. The amorphous silica mounted on an aluminum base was used for calibrating the area function of the tip. A range of loads up to 45 mN and 400 mN were used in these experiments by using iNano and G200 nanoindenter, respectively. During the experiments, the load and penetration depth was measured during the entire indentation tests and the hardness was measured by using the Oliver-Pharr method [44].

The LC and CSM methods were used to study the ISE behavior and the effect of the change in hardness during multiple pop-in events, respectively (see section 4.2.1 for details).

3.5.3 High Temperature (350 °C) Berkovich Indentations

An instrumented indentation system (G200 Nanoindenter, Keysight Technologies, USA) equipped with both sample and sapphire indenter tip heating (Laser Heater for Nanoindentation, Surface Systems Technology, Germany) was used for 25°C and 350°C indentation testing. The sapphire Berkovich tip was heated by an 808 nm laser having a maximum power of 4W from the back of the tip. The STO sample was mounted with a graphite glue onto a quartz plate within the nanoindenter sample tray.

Sample heating was accomplished with a 939 nm laser having a maximum power of 45 W. A thermocouple was embedded within the quartz plate less than 1mm from the bottom surface of the sample. The temperature was held constant with PID controller. The temperature control for tip and sample was within 0.1°C of the target temperatures. Since STO is highly non-conducting, the sample surface temperature was measured by an additional thermocouple in direct contact. The sample surface temperature was found to be only 70% of the stage thermocouple temperature. The tip temperature was therefore set to match the observed surface temperature of the sample in order to avoid thermal gradients. In an effort to minimize thermal drift, indentation load was linearly ramped to the maximum (50, 100, and 200 mN) in 5s, followed by a 1s hold, and then a 5s unload to 90% of the maximum load. Drift rates, i.e., the time rate of change in displacement under constant load, were subsequently estimated.

Amorphous silica mounted on an aluminum base was used for calibrating the area function of the tip. However, during preliminary testing, a noticeable blunting of the sapphire tip was found at higher temperatures. So, hardness, H, was calculated by the applied load divided by the contact area in order to avoid complications with tip blunting over the course of the testing.

3.6 HR-EBSD

The HR-EBSD measurements were performed on both STO Berkovich and spherical indentations (in etched and un-etched conditions) at the surface and various polishing depths. The indentations with residual impression / etched surface can be easily located for HR-EBSD measurements. However, for polished cross-sections, the plastic zone below the residual impression is not visible inside the SEM. Therefore, larger indentation depth reference arrays were made close to the indentations of interest. An exemplary region is shown in Fig. 3.6.1, where indentations of load 2 mN, 5 mN and 10 mN are the arrays of interest, whereas the reference arrays are indicated by dotted rectangles.

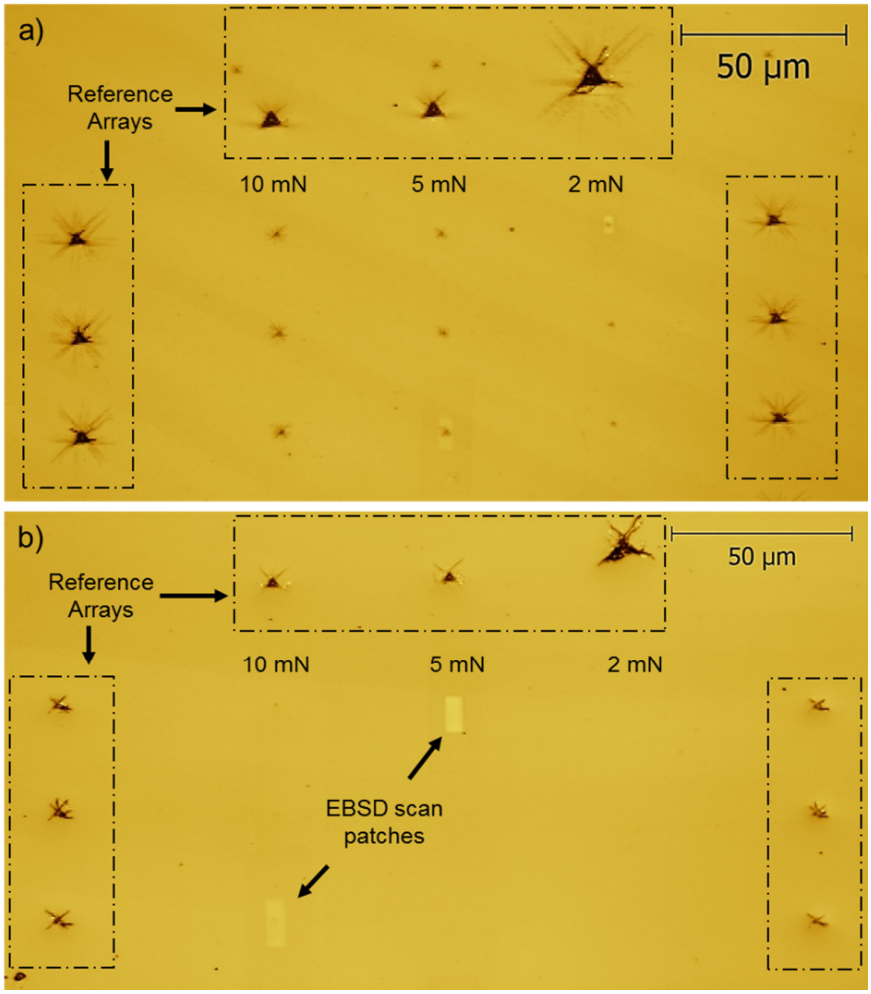

Fig. 3.6.1: Laser microscope images of reference arrays (in dotted boxes) along with arrays of interest (2 mN, 5 mN and 10 mN) for HR-EBSD measurements at a) Surface in etched conditions b) after polishing in un-etched condition

At the surface, in etched conditions, each 2 mN, 5 mN and 10 mN indentation can be easily identified (Fig. 3.6.1a). However, on the polished surface and in the un-etched conditions, the residual impression or plastic zone is not visible for the small load indentations (Fig. 3.6.1b). In such cases, the indentations of interest were located by measuring the distance from the arrays of reference indentations and HR-EBSD was performed.

The HR-EBSD measurements were made with a TESCAN MIRA3 SEM equipped with an EDAX TSL DigiView EBSD system (EDAX, Mahwah, NJ, USA). The system was operated at 15keV. A very thin layer of carbon was used to avoid drift and charging effect. An exemplary Kikuchi pattern of a carbon coated (001) oriented STO single crystal along with simulated pattern is shown in Fig. 3.6.2, which clearly indicate a good quality pattern and ensure the reliability of EBSD measurements for further analysis.

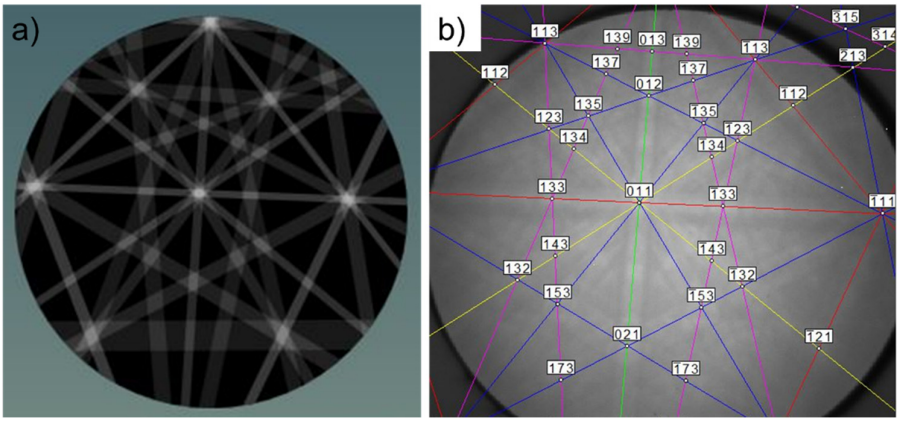

Fig. 3.6.2: Kikuchi pattern of (001) STO single crystal (a) simulated pattern (b) carbon coated pattern

Fig. 3.6.3 shows a High Resolution Kernel Average Misorientation (HR-KAM) Map obtained on the etched surface of R = 7.5 µm spherical indentation.

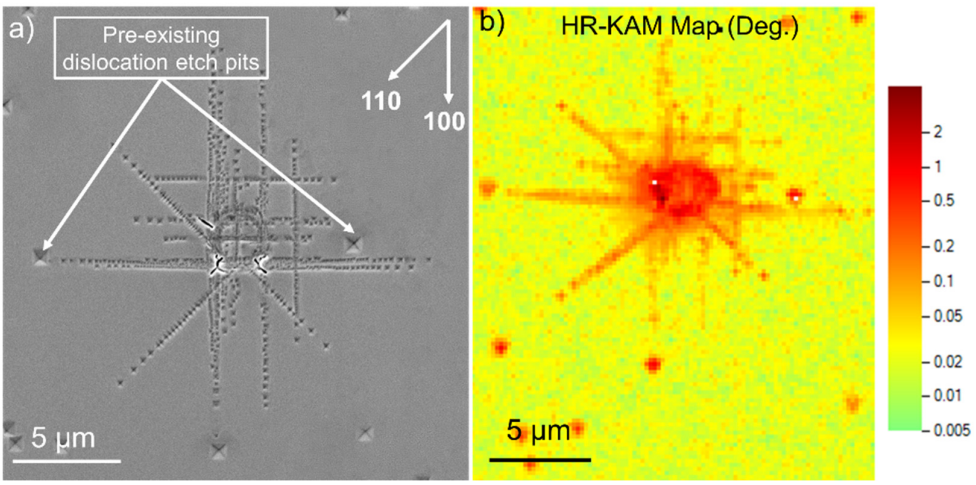

Fig. 3.6.3: Spherical indentation of R = 7.5 µm tip, showing dislocation microstructure at the surface (a) SEM image showing dislocation etch-pit structure (b) HR-KAM map showing higher misorientation at positions of etch-pits

The HR-KAM map clearly indicates the higher misorientation in both <100> and <110> dislocation etch-pits positions along with the pre-existing dislocation etch-pits (larger red spots). The same indentation was polished to remove 300 nm of material from the surface of the specimen and HR-EBSD was performed on the non-etched surface, which reveals only the central regions of the indentation in the HR-KAM map (Fig. 3.6.4b). After EBSD measurements, the indentation was re-etched, which reveals the dislocation pile-ups in both <100> and <110> directions at 300 nm depth below the indentation (Fig. 3.6.4a).

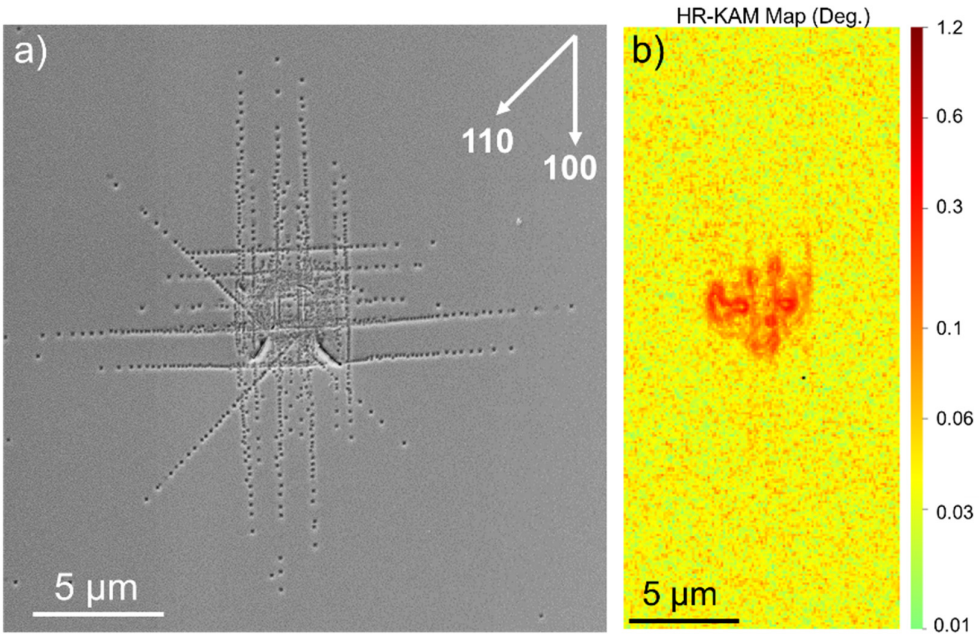

Fig. 3.6.4: Spherical indentation of R = 7.5 µm tip, showing dislocation microstructure after removing 300 nm of material (a) SEM image showing pile-ups in both <100> and <110> directions (b) HR-KAM map showing misorientation only in the central region of indentations

This evidence confirms that the presence of pile-ups in HR-KAM on the etched surface were artificial due to the presence of etch-pits. Therefore, in the present work, all the EBSD measurements were performed on non-etched surfaces. After EBSD measurements, specimens were re-etched to reveal the dislocation etch-pit structure at that particular depth and for direct comparison with HR-EBSD maps.

HR-EBSD measurements were performed by using 100 nm and 200 nm step sizes. Fig. 3.6.5 shows GNDs distribution map for two 5 mN polished Berkovich indentations performed at 100 nm and 200 nm step sizes.

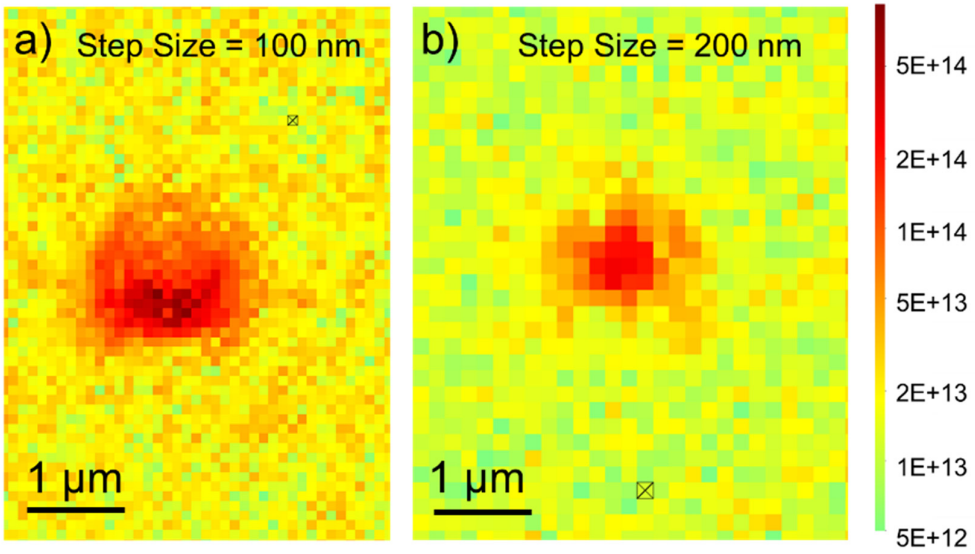

Fig. 3.6.5: GNDs distribution map obtained from HR-EBSD analysis of 5 mN Berkovich indentations using a step size of (a) 100 nm (b) 200 nm

The noise level was calculated by excluding the dense region of GNDs from the rest of scan area. For 200 nm step size measurements, the noise level was found to be lower (~ 1.4 x 10^{13} m^{-2}) compared to 100 nm step size (~ 2.5 x 10^{13} m^{-2}). However, due to larger step size (200 nm), the data points in the central region of indentation were reduced as compared to 100 nm step size measurement. Therefore, for smaller indentation depths and quantification of dislocations, a step size of 100 nm was used.

The EBSD patterns were analyzed using the commercial software Cross-Court 4 (CC4) from BLG Vantage Software Inc. (Bristol, UK). The software CC4 involved the cross-correlation analysis based on the detection of small shift with respect to a reference pattern, representing a un-strain region. The details of GND density distribution and elastic strain calculations can be found in reference [107]. With regards to the uniaxial compression and indentation testing cited above in section 2.4 along with the results in the present work, ⟨110⟩{110} slip systems were used in crosscourt software for analyzing GNDs distribution maps.

In subsequent sections, 3D dislocation structure at incipient plasticity and its evolution around and underneath the spherical indentations will be discussed first. This discussion will be followed by the room and elevated temperature Berkovich indentation experiments.

Chapter 4 Results and Discussion

4.1 Spherical Indentation Experiments

4.1.1 Incipient Plasticity and Effect of Pre-existing Dislocations

The strong influence of pre-existing dislocations on incipient plasticity is demonstrated by carrying out the nanoindentation experiments on pre-etched STO single crystal. Fig. 4.1.1(a) shows a SEM image of an exemplary region of two ball indentations from a regular array of twenty indents (having a spacing between two consecutive indents of 70 µm) performed at maximum load of 50 mN with R = 7.5 µm tip radius spherical indenter along with representative load-displacement curves (Fig. 4.1.1b).

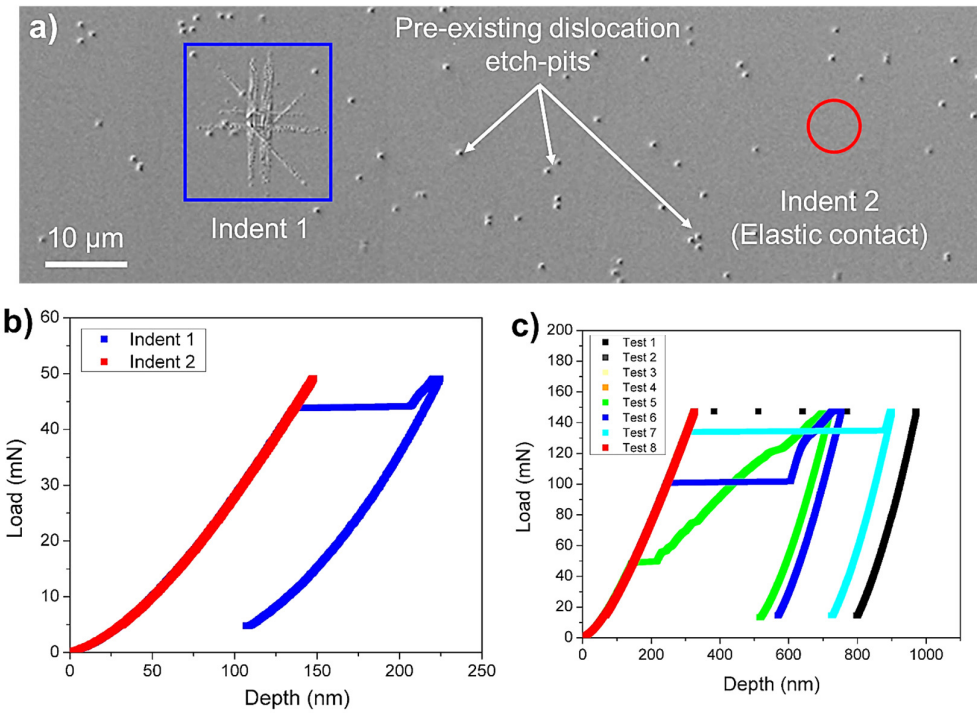

Fig. 4.1.1: (a) Etched SEM image of R = 7.5 µm spherical indentations along with load – displacement curves (b) 50 mN (c) 150 mN, where tests 2,3,4 & 8 were pure elastic, having loading – unloading curve on top of each other.

The average initial dislocation density in the region was determined to be 1.8×10^{10} m^{-2}. Out of twenty indentation tests, only two indentations led to plastic deformation. For such a plastic contact, a clear pop-in was observed in the load-displacement curve (indent

1 in Fig. 4.1.1(b)), whereas elastic contact leads to a completely reversible loading and unloading curve (indent 2). The absence of a plastic zone for indent 2 was confirmed by etching (indicated by a red circle in Fig. 4.1.1a). Even for crystals with a very low initial dislocation density, the probability of the dislocation nucleation increases with increasing load [54]. Fig. 4.1.1(c), obtained at a load of the 150 mN indentation experiment, shows plastic deformation at higher loads and with a larger pop-in length. When pre-existing dislocations were inside / close to the contact location, the pop-in occurred at much lower loads with smaller pop-in lengths (see test 5 in Fig. 4.1.1(c)). However, for the regions like indent 2 (Fig. 4.1.1a), contact either would be elastic (test 2,3,4&8) or pop-in occurred at much larger load with larger pop-in lengths (test 1&7) as shown in Fig. 4.1.1(c). The influence of pre-existing dislocations on the pop-in phenomenon is well-known and discussed in the literature [29, 55]. However, it is pertinent to mention here that the incipient plasticity load is strongly related to dislocation structure around the indentations. When first pop-in occurs at lower loads, only few dislocation pile-ups can be observed, whereas at larger first pop-in event load, fully developed dislocation pile-ups structure can be seen for STO. This direct relevance of the dislocation structure to incipient plasticity is reported here for the first time in STO.

Several indentations were stopped just after the first pop-in event to study the dislocation structure at incipient plasticity. Fig. 4.1.2(a) illustrates the result for R = 7.5 µm spherical indentation that was stopped after the first pop-in event at a load level of 40 mN. Inside the residual impression, a couple of etch-pits that remained from the pre-etching can clearly be seen. After indentation, but before re-etching, several slip steps in <100> direction are observable (Fig. 4.1.2a). This suggests that the slip along the <100> directions leads to the formation of surface steps indicating a Burgers vector with a component perpendicular to the surface.

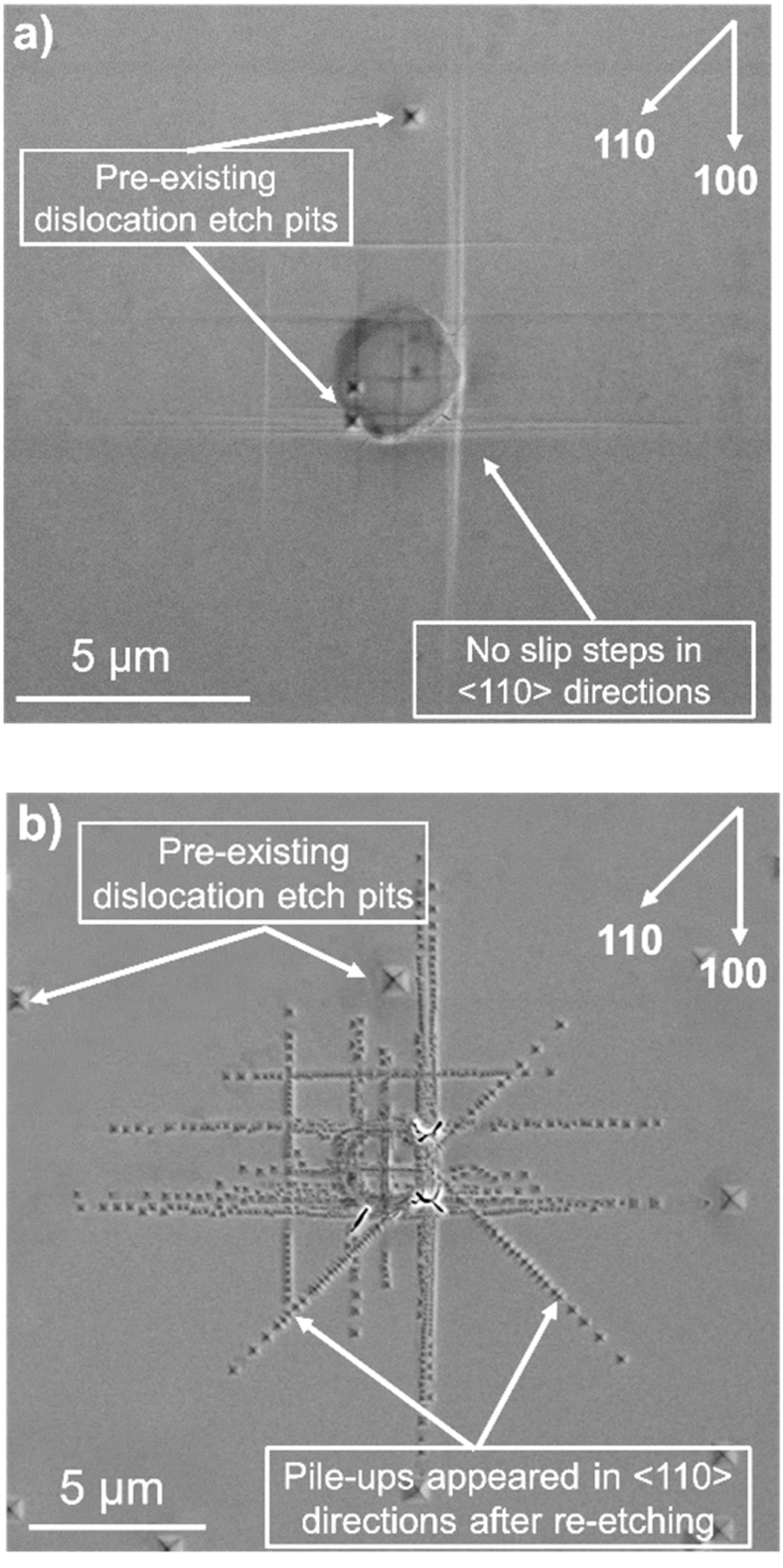

Fig. 4.1.2: SEM images of 7.5 µm tip radius spherical indentation (a) before etching showing slip step only in <100> directions (b) after re-etching showing etch-pits in <100> as well as <110> directions

After re-etching of the same indent, dislocation etch-pits appear along the slip steps aligned in <100> directions, but also in <110> directions (Fig. 4.1.2b). As will be shown by our simulations, these additional etch-pits along <110> directions are associated with dislocations on $\langle 110 \rangle \{1\bar{1}0\}$ systems, which have a Burgers vector parallel to the surface plane and dislocations emerge with a pure edge character. Consequently, these dislocations do not leave behind surface steps, and etching was thus required to make them visible.

The present spherical indentation analysis provides a direct experimental evidence showing pre-existing dislocations also strongly influence the maximum shear stress (τ_{max}) at the pop-in load. The spherical indentations conducted close to pre-existing dislocations showed lower τ_{max} values. For the spherical indentation shown in Fig. 4.1.2, the maximum shear stress was determined using $\tau_{max} = 0.31 p_o$, where p_o was calculated from Eq. 2.2.10. The τ_{max} was calculated to be ~ 5.6 GPa, using the pop-in load of 40 mN, an effective indentation modulus of 264 GPa and an indenter tip radius of 7.5 µm. Since the shear modulus of STO is 107 GPa, the calculated τ_{max} value was determined to be very low as compared to the theoretical shear strength ($G/2\pi$) value of 17 GPa. However, for the regions like indent 2 (Fig. 4.1.1), for 7.5 µm tip radius spherical indentations, the average τ_{max} value was determined to be 9.1 ± 0.9 GPa. On the other hand, for similar regions, the average τ_{max} for 25 µm tip radius spherical indentations was determined to be 6 ± 0.1 GPa, which is even lower than the 7.5 µm tip radius spherical indentations. To explain the influence of pre-existing dislocations on τ_{max}, a schematic diagram showing the effect of change of indenter tip radius on the influence of highly stressed zone below the indentations are shown in Fig. 4.1.3.

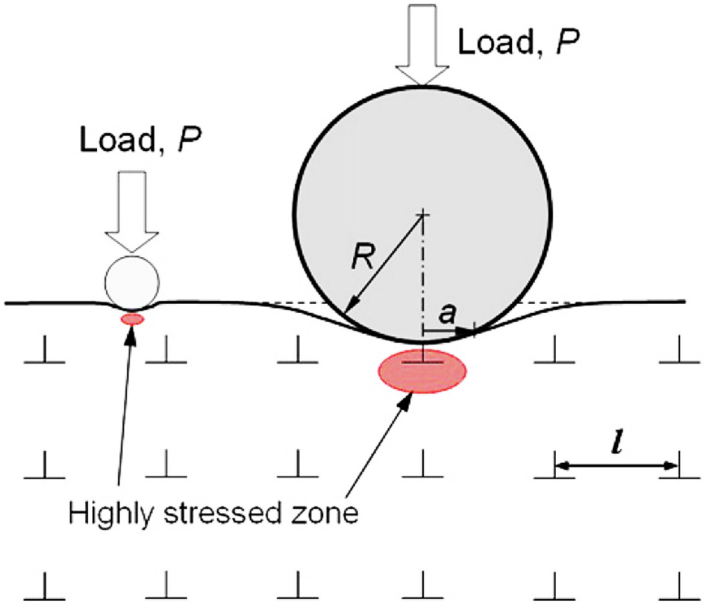

Fig. 4.1.3: Schematic diagram showing the geometry of the nanoindentation test with spherical indenters [54]

For the small spherical indentations, there is a larger probability that the highly stressed region can be much smaller than the average spacing between the dislocations '*l*'. Therefore, the plasticity can occur at much higher shear stress. Whereas, for larger spherical indentations, the probability of the presence of pre-existing dislocations in the highly stressed region is higher, which leads to plasticity at lower stresses. Hence, for 25 µm tip radius spherical indentations, the τ_{max} was calculated to be lower (~6 GPa) as compared to 7.5 µm tip radius spherical indentations. Moreover, for 7.5 µm spherical indentations, when the indentations were made inside / close to the pre-existing dislocations, the maximum shear stress is reduced from ~ 9.1 GPa to the ~ 5.6 GPa. If the indentations are made in a dislocation free region with a smaller tip radius, the τ_{max} value is expected to reach close to the theoretical shear strength value at pop-in event, which will be discussed in section 4.2.1 for Berkovich indentation experiments.

4.1.2 Three-dimensional Dislocation Structure Evolution and Activated Slip Systems

The evolution of the plastic zone during spherical indentation is strongly dependent on the dislocation density as well as the tip radius. For pristine crystals, a large pop-in will prevent studying the dislocation structure at low a/R ratios, which is, however, important for understanding the evolution of the dislocation structure from an elastic-plastic transition to a full plastic behavior. Therefore, a larger spherical indenter tip with R = 2.5 mm was used and

the dislocation structure evolution was analyzed in terms of the representative strain measure a/R. Fig. 4.1.4 illustrates the dislocation etch-pit structure around a 2.5 mm radius ball indentation at 50 N load with the dotted circle indicating the contact area.

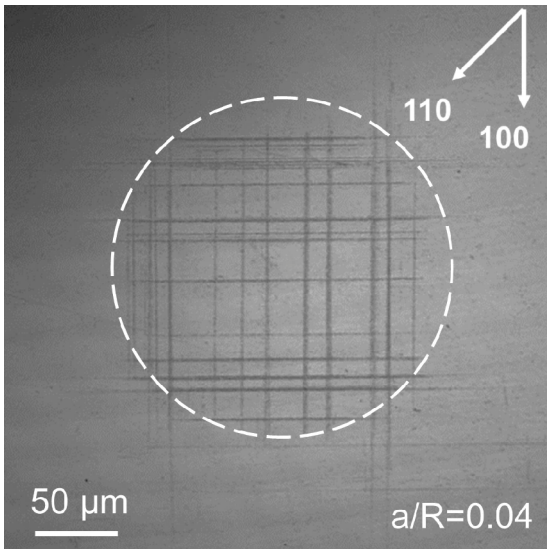

Fig. 4.1.4: Laser microscope image of an etched 2.5 mm tip radius spherical indentation at 50N load

At a/R=0.04, only dislocation pile-ups in <100> directions can be seen, confirming that they appear first. Furthermore, the dislocation pile-ups form an intersecting quadratic figure, which resembles a box like structure.

For small spherical indenter tip indentations (R = 25 µm), at a/R = 0.12, dislocation pile-ups along <110> directions were also observed, along with pile-ups in <100> directions (Fig. 4.1.5a) indicating that the pile-ups in <110> directions appear at a later stage of plastic deformation. With increasing indentation load, the number of dislocation pile-ups in <100> and <110> directions increases, leading to a fully developed asterisk-shaped plastic zone as shown in Fig. 4.1.5b. Both of these indentations (Fig. 4.1.5 (a) and (b) at 190 and 400 mN load, respectively) were stopped just after first pop-in event and a clear dependence of the dislocation etch-pit pattern on the pop-in load can be seen, which was mentioned briefly in section 4.1.1.

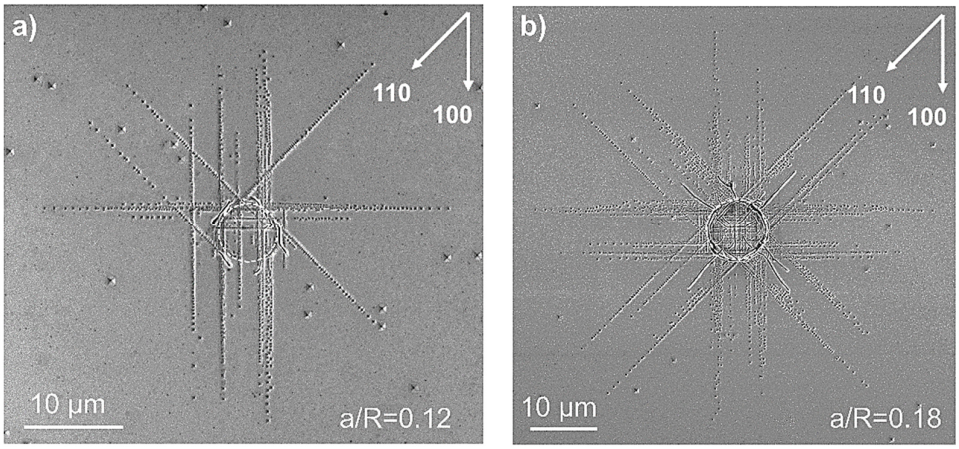

Fig. 4.1.5: SEM images of 25 µm tip radius spherical indentations at (a) 190 mN (b) 400 mN

It seems that larger plastic strains lead to the activation of new slip systems, which are required to accommodate the shape of the spherical indenter. Interestingly, the lengths of <110> dislocation pile-ups exceed those of <100> pile-ups at higher loads, which suggests that dislocation glide in the <110> pile-ups is easier compared to <100> directions. For 7.5 µm tip radius spherical indentations, a similar evolution of the dislocation structure was observed as shown in Fig. 4.1.6.

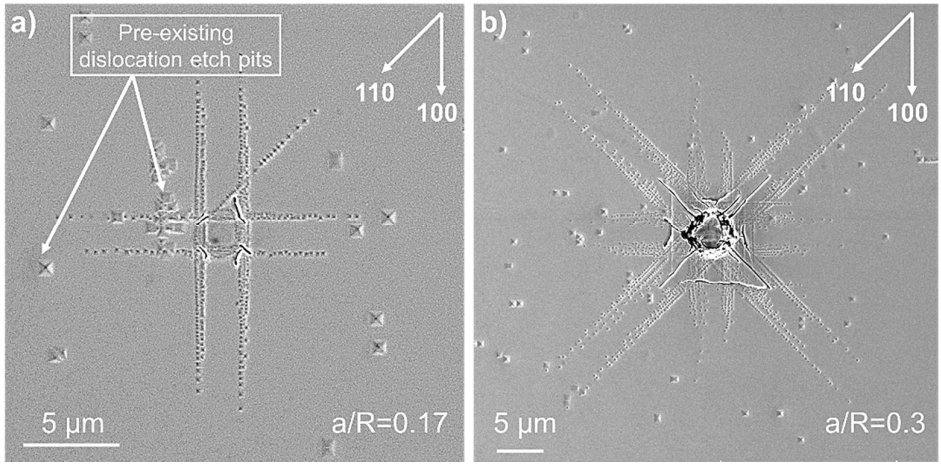

Fig. 4.1.6: SEM images of 7.5 µm tip radius spherical indentations at (a) 50 mN (b) 150 mN

From the shape of etch-pits and by tracking the dislocation pile-up, further insight into the 3-dimensional distribution of the slip systems can be gained (Fig. 4.1.7-8). For this purpose, a 25 µm tip radius spherical indentation at a/R = 0.1 was analyzed. The morphology of an individual etch-pit can already give an indication of the orientation of the dislocation line with respect to the surface.

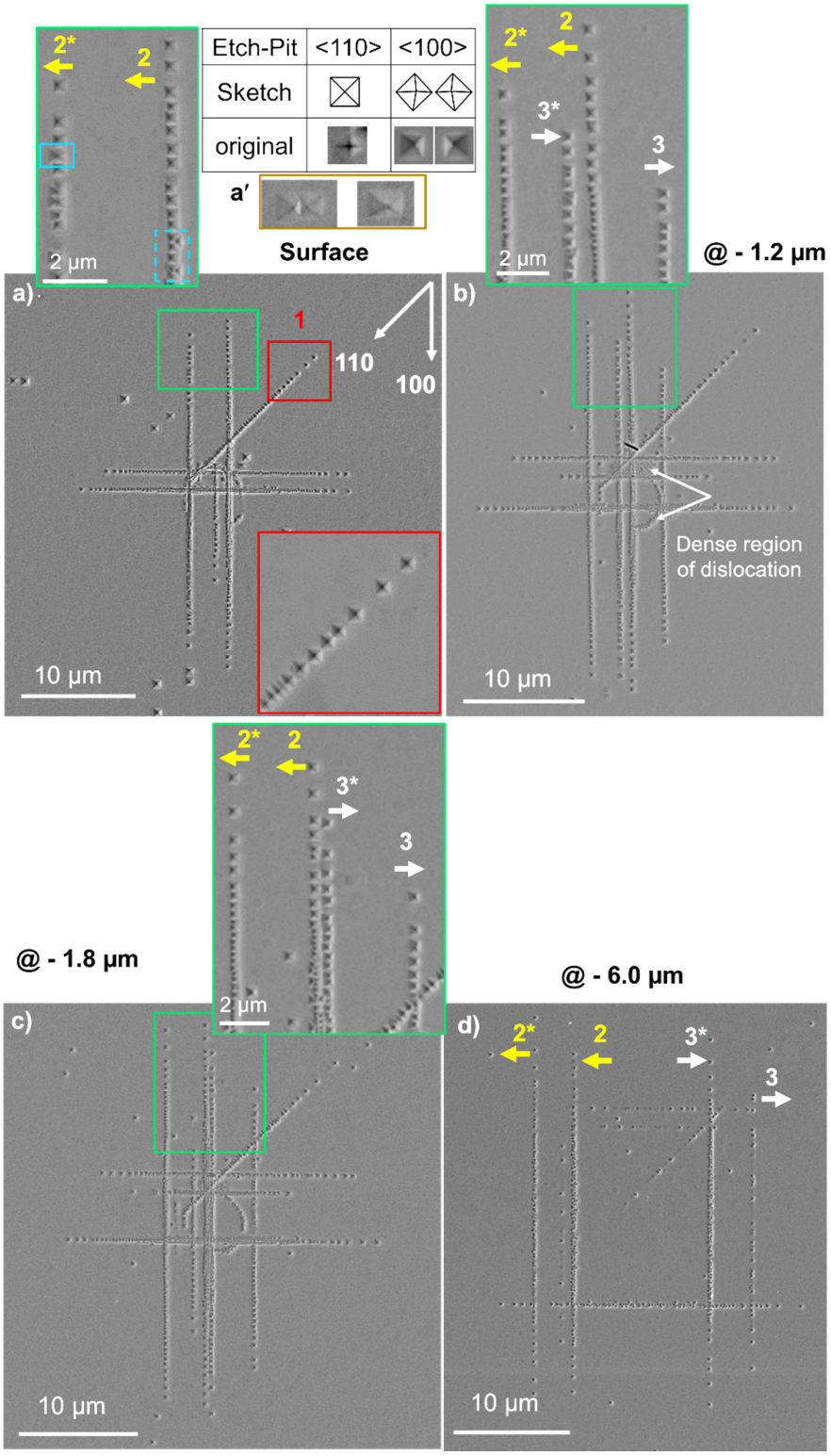

Fig. 4.1.7: SEM images of 25 µm tip radius spherical indentation (a) at the surface along with inset regions showing the symmetrical and non-symmetrical etch-pits in <100> and <110> directions, after polishing (b) -1.2µm (c) -1.8µm (d) – 6.0 µm

For both <100> and <110> directions, dislocation etch-pits with square-shape were found. A closer observation reveals that etch-pits from dislocations in <110> pile-ups are symmetrical in shape (centered bottom) whereas non-symmetrical (off-centered bottom) for <100> pile-ups (inset region of Fig. 4.1.7a). The center position of the non-symmetrical etch pits is either shifted to the left or to the right. In dislocation pile-up #2, the last few etch-pits clearly exhibit a left-shifted center indicating that the intersecting dislocation line is inclined to the surface in the left direction. The symmetrical etch-pits of pile-up #1 (along <110> direction) indicate that these dislocation lines are perpendicular to the surface. Fig. 4.1.8 schematically illustrates the inclination of dislocation line below the surface for symmetrical and non-symmetrical etch-pits.

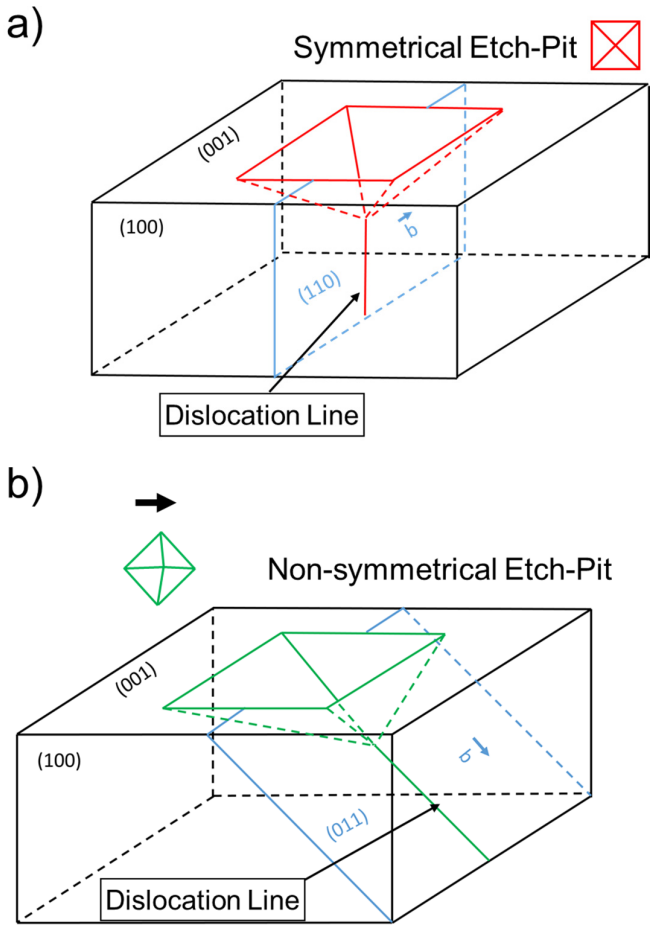

Fig. 4.1.8: Schematic illustration showing the inclination of dislocation with respect to etch – pit (a) symmetrical (b) non-symmetrical

Since the indented plane was (001), the symmetrical etch-pits suggest that the dislocation lines of pile-up #1 lie on {110} planes, which are perpendicular to the surface

(denoted as $\{110\}_{90}$ in the following). Whereas dislocations leading to non-symmetrical etch-pits lie on either $\{110\}_{45}$ (denoting 45° inclination with respect to the surface) or on $\{100\}_{90}$ slip planes. The off-centered shape of the etch-pit indicates that the dislocations in <100> direction lie on $\{110\}_{45}$ slip planes. Fig. 4.1.9 schematically illustrates the assumed configuration of dislocation half loops that lead to pile-ups of symmetrical and non-symmetrical etch-pits.

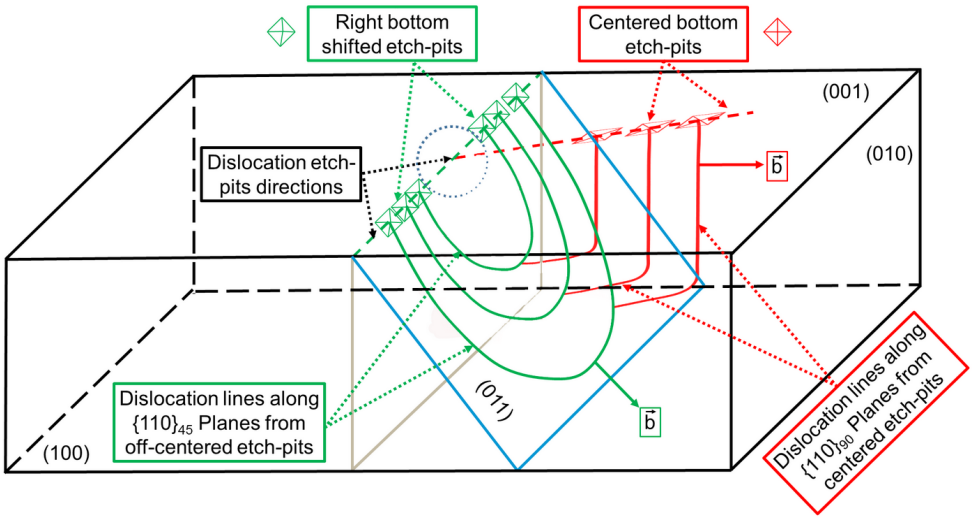

Fig. 4.1.9: Schematic illustration of dislocation half loops underneath the indentation from centered and off-centered dislocation etch-pits along $\{110\}_{90}$ and $\{110\}_{45}$ planes

The dislocation pile-ups in <100> directions were tracked below the surface to confirm that the dislocations lie on $\{110\}_{45}$ planes. For this purpose, sequential polishing and etching were performed. After removing 1.2 µm and 1.8 µm of material from the surface of the specimen, a significant change in dislocation pile-up positions in <100> directions was observed. As expected, pile-up #1 in <110> direction did not change its position (Fig. 4.1.7), because dislocations are located on a plane perpendicular to the surface. The dislocation pile-ups #2 and #2* were chosen as exemplary pile-ups to discuss the 3D nature of slip planes and pile-ups. For both pile-ups, #2 and #2*, a left off-centered shift for the last few etch-pits can be clearly seen in the inset of Fig. 4.1.7(a) indicating an inclination with the surface. Moreover, the shape of the fourth etch-pit in pile-up #2* (marked with a blue box) was found to be non-square. Such non-square shapes occur when dislocations are very close to each other, and their etch-pits combine as illustrated in Fig. 4.1.7(a′). Below the blue boxed etch-pit in pile-up #2*, the shape of etch-pit was found to be square again with left-shifted center, which suggests the presence of another dislocation pile-up close to pile-up #2*. Similarly, in the dotted rectangular

region in pile-up #2, we identified additional nearby etch-pits, suggesting the presence of multiple pile-ups close to pile-up #2.

After removing 1.2 µm of material from the surface and subsequent etching, two new pile-ups #3 and #3* close to pile-up #2 and #2* were observed as shown in Fig. 4.1.7b. The etch-pit centers in pile-up #3 and #3* were found to be right-shifted, indicating an inclination of dislocations opposite to pile-ups #2 and #2*. The distance between pile-up #2* and #3* at this depth was measured to be ~2.4 µm, which is twice the polishing depth. This strongly suggests that the elongated non-square etch-pits on the original surface in Fig. 4.1.7(a) were due to a near overlap of pile-ups #2* and #3*, which separate below the surface. Fig. 4.1.10 schematically shows the alignment of pile-ups #2,# 2*, #3 and #3* below the indenter along differently oriented $\{011\}_{45}$ planes.

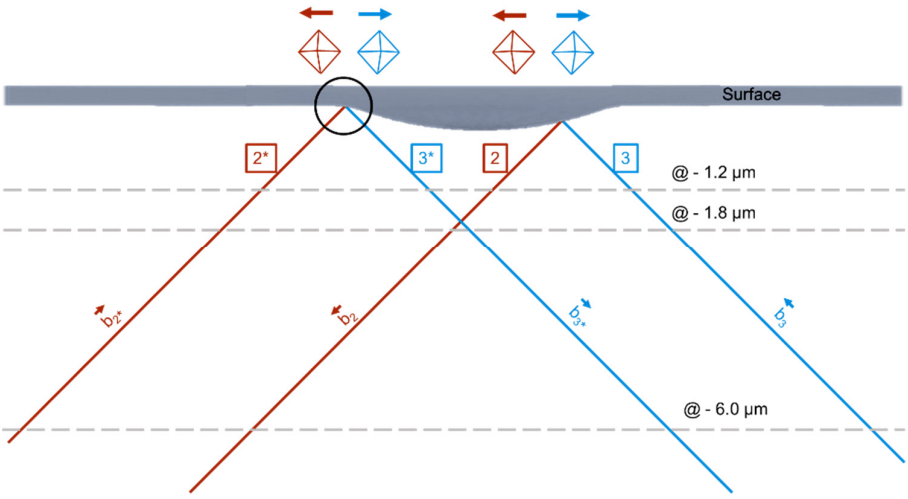

Fig. 4.1.10: Schematic illustration of dislocation pile-up #2, #2, #3 and #3* movement below the indentations along $\{110\}_{45}$ planes*

Fig. 4.1.10 indicates that the pile-ups #2 and #3* should cross each other between the depths of 1.2 µm and 1.8 µm. SEM images of the surface polished to 1.8 µm depth confirmed this crossing (Fig. 4.1.7c). A significant change in etch-pit spacing in pile-ups #2 and #3* can be seen before and after crossing, indicating some interaction between the intersecting pile-ups. In addition to that the length of pile-up #2 decreases after crossing pile-up #3*.

Further polishing (down to 6 µm) revealed a dislocation free region surrounded by a box-shaped etch-pit structure consisting of <100> dislocation pile-ups lying on $\{110\}_{45}$ slip

planes. Due to the U-shaped half loops below the indentation, a shortening of the pile-up lengths in <100> and <110> etch-pit directions (Fig. 4.1.7d) was observed, whereas the <110> pile-ups nearly vanished.

Right below the surface, a region of high dislocation density with a half circular shape can be clearly identified (Fig. 4.1.7b). In this region, complex dislocation interactions are expected. The dislocation etch-pits with a spacing of ~50 nm were resolved in this dense region of dislocations, by lowering the etching time. This corresponds to a maximum dislocation density of 4 x 10^{14} m^{-2}, which is much higher than the values recently reported by Patterson et al. [23] during uniaxial compression testing using the X-ray diffraction rocking curve technique. The shape of individual etch-pits in the dense region of dislocation density (Fig. 4.1.7b) cannot be resolved and the probability of etch-pit coalescence is much higher. Due to these issues, 3D dislocation etch-pit tracking is not feasible, making it difficult to identify the activated slip systems. Therefore, MD simulations were conducted to provide further insight into the defect interaction mechanisms.

4.1.3 MD Simulations

Standard experimental techniques can provide only an incomplete view of the microscopic processes that govern the materials response in nanoindentation tests, especially, when they take place below the surface. In order to develop a more complete understanding of 3D dislocation structure formation, MD simulations were performed by Alexander Stukowski in collaboration with Material Modelling division of TU Darmstadt.

The MD model of single crystal STO comprises 160 x 160 x 80 perovskite unit cells (10.2 million atoms). The spherical indenter (R=32 nm), which is modeled as a moving repulsive force field, is moved along $[00\bar{1}]$ at constant velocity (v=40 m/s) into the material. The temperature of the system is kept close to 0 K to study the quasi-static behavior of the specimen and exclude temperature and indentation rate-dependent effects as far as possible. The simulations were performed with the simulation code LAMMPS [118] and analyzed with our software OVITO [119]. Long-range Coulombic interactions were computed with the particle-particle particle-mesh (PPPM) solver of LAMMPS.

To assess possible model size effects, we repeated the simulation with a larger crystal (320 x 320 x 240 unit cells, 123 million atoms). The observed dislocation structures are virtually the same as in the small model, but the larger crystal shows a more compliant behavior, both in the elastic and the plastic regime due to the extended material volume. Thus,

the simulation volume does not fundamentally affect the formation of dislocation defects in the plastic zone, whereas hardness values reported from these simulations cannot be directly compared to experiments on larger scales. Furthermore, we repeated the simulation at four times slower indentation rate, which showed no significant difference in the load response or the observed dislocation structures.

As will be discussed below, complex defect structures form below the indenter in the MD simulation. While conventional atom filtering techniques [120] are routinely being used to reveal structural defects in simulated crystal lattices, their ability to discriminate between different types of crystal defects is limited. In this study we employ a more sophisticated computational analysis technique, the so-called dislocation extraction algorithm (DXA) [121-122], which provides additional informative value: It can reliably and efficiently tell dislocations apart from other kinds of crystal defects, identify their Burgers vector and character, and build a discrete line representation of the dislocations in a fully automated manner. This conversion from the atomistic model to a clear and highly reduced description of the dislocation line network enables us to follow the formation, motion and reaction of dislocations in great detail.

In the simulated nanoindentation experiment, the dislocation structure evolution was developed in several steps. The load-displacement curve and the associated dislocation structure will be discussed in following. As Fig. 4.1.11(A) shows, at the end of the purely elastic regime, the first drop in the measured indentation force was associated with the nucleation of two dislocation loops on the $(10\bar{1})$ and $(\bar{1}0\bar{1})$ planes 3-5 nm below the contact. These closed loops quickly turn into half-loops when reaching the nearby surface and expand into the material at an angle of 45° to the surface (Fig. 4.1.11A). Soon after, more loops successively nucleate on all four equivalent planes$(10\bar{1})$, $(\bar{1}0\bar{1})$, $(01\bar{1})$, and $(0\bar{1}\bar{1})$, forming a four-fold symmetric dislocation structure. The points of intersection of the half-loops with the surface move along the four $\langle 100 \rangle$ directions away from the indent. The dislocations all have $\langle 10\bar{1} \rangle$ Burgers vector forming an angle of 45° with the surface (Fig. 4.1.11B). At the surface intersections, the dislocations have pure screw character and leave behind surface steps as confirmed by experimental evidence (Fig. 4.1.2a).

Loops on the four active $\{101\}_{45}$ glide planes intersect and eventually start to form a dense, entangled network of dislocations in the region below the contact area of the indenter. At higher loads (Fig. 4.1.11D), we observe frequent reactions below the contact area. The interaction of

two expanding $\langle 10\bar{1}\rangle$ loops on different $\{101\}_{45}$ slip planes triggers a dissociation of one of the dislocations at the intersection node (reaction $\langle 10\bar{1}\rangle \rightarrow \langle 100\rangle + \langle 00\bar{1}\rangle$). This dissociation reaction proceeds within a limited range along the $\langle 10\bar{1}\rangle$ loop and away from the intersection node. The edge component of the small $\langle 00\bar{1}\rangle$ product loop glides towards the surface. In some instances, the local stress is high enough to also activate the bowing out of the $\langle 100\rangle$ dislocation, which then expands on a plane parallel to the surface. Most importantly, however, the sessile dissociation node of the original $\langle 10\bar{1}\rangle$ subsequently acts as a nucleation site for $\langle 110\rangle$ dislocation loops expanding on a $\{\bar{1}10\}_{90}$ planes, which forms a 90° angle with the {001} surface. This process, thus leads to vertically aligned edge dislocations that will eventually form pile-ups along <110> directions on the surface (red lines in Fig. 4.1.9). The activation of such additional glide systems is necessary to accommodate the large strains during spherical indentation. It should be noted, however, that the absolute size of the simulation model is very small compared to the experiments and that the full evolution of the extended plastic zone is not accessible using an atomistic simulation approach due to inherent size and time limitations.

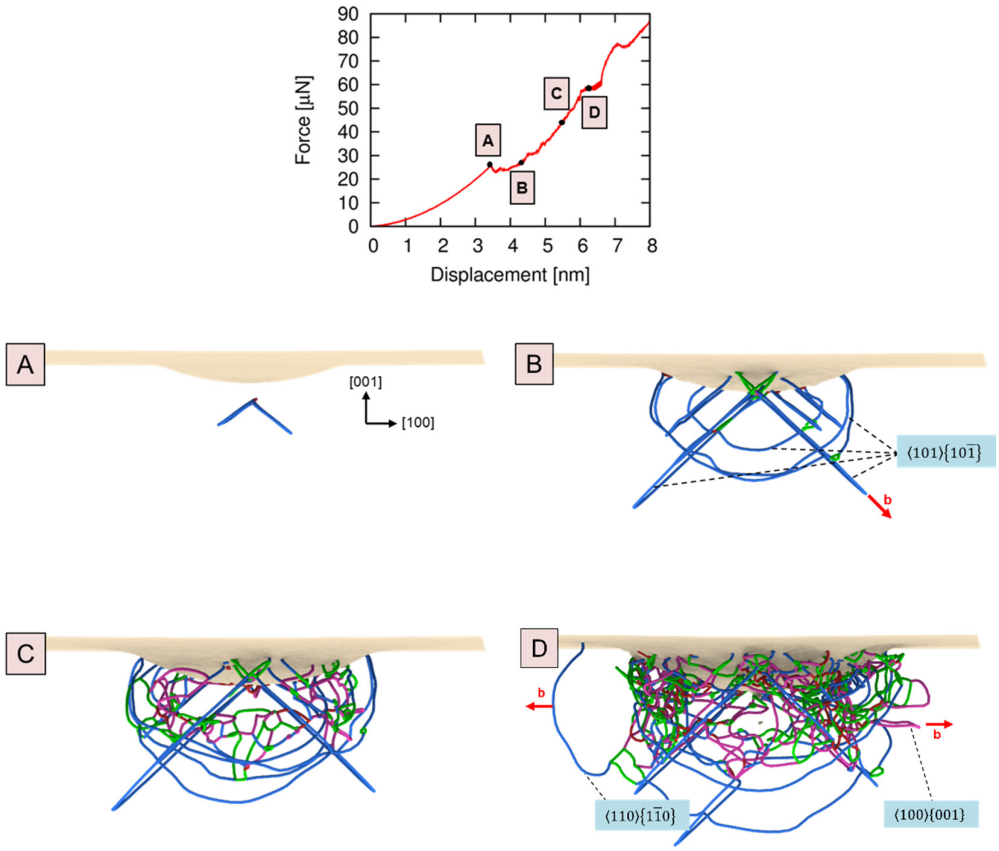

Fig. 4.1.11: Top: Force-displacement curve obtained from MD simulation of indentation with a 32 nm radius sphere. Bottom: Snapshots of the extracted dislocation structure corresponding to points A, B, C and D along the force-displacement curve. Dislocation line colors indicate Burgers vector types (blue: <110>, magenta: <100>, green: ½<111>)

4.1.4 Experimental vs MD simulation

Within the size limitations of the MD model, a good agreement between the experimentally observed and simulated dislocation structures was found. Both experiments and MD simulations confirmed that at the early stage of plastic deformation slip starts along $\{110\}_{45}$ planes. MD simulation revealed that the dislocations along $\{110\}_{45}$ planes have a pure screw character at the intersection with the surface and lead to a surface step formation, which is confirmed by non-etched indented SEM analysis (Fig. 4.1.2a). At later stages of plastic deformation, MD simulation analysis shows the onset of slip along $\{110\}_{90}$ planes as a result of dislocation interaction in the dense defect region below the contact area. The Burgers vector

for dislocations along $\{110\}_{90}$ planes were found to be parallel to the surface. For that reason, no steps were observed along <110> directions and only re-etching revealed these pile-ups in <110> directions (Fig. 4.1.2a). The origin of <110> pile-up can also be traced back experimentally to the high density region below the indentation. It must be noted, however, that the MD simulations are performed at much higher displacement rates and smaller contact sizes. That is why a quantitative and one-to-one comparison between experiment and MD simulation is beyond the scope of the present work.

Furthermore, MD simulation analysis revealed different sub-surface dislocation reactions in the dense defect region, which cannot be studied from dislocation etch-pit tracking. For instance, an additional slip system $\langle 100\rangle\{001\}$ was identified in the MD simulations, which is oriented parallel to the surface and therefore cannot be made visible using the etch-pit technique. It, therefore, remains unclear whether it is active in the experiment or just an artifact of the simulation. Yang et al. [25] reported the slip along $\langle 110\rangle\{001\}$ and $\langle 110\rangle\{1\bar{1}0\}$ systems from Vickers's macro-indentation TEM analysis, which is the only study giving indication of a secondary slip system, i.e., $\langle 110\rangle\{001\}$. However, Matsunaga et al. and Kondo et al. [24, 26] in their ex-situ and in-situ TEM analysis, observed slip only for $\langle 110\rangle\{1\bar{1}0\}$ systems. In the present work, from careful analysis of 3D dislocation pile-ups and etch-pit structure equipped with MD simulations, slip along $\langle 110\rangle\{1\bar{1}0\}$ systems can be confirmed, but no slip in $\langle 110\rangle\{001\}$ system was found at room temperature, during spherical indentation experiments.

4.1.5 Indentation Size Effect for Spherical Indentations

As briefly mentioned in section 2.2.3, the ISE for spherical indentations is manifested through the radius of the sphere rather than the depth of penetration. Therefore, a plot between hardness as a function of a/R is shown in Fig. 4.1.12 for 7.5 µm, 25 µm and 2.5 mm tip radius spherical indentations.

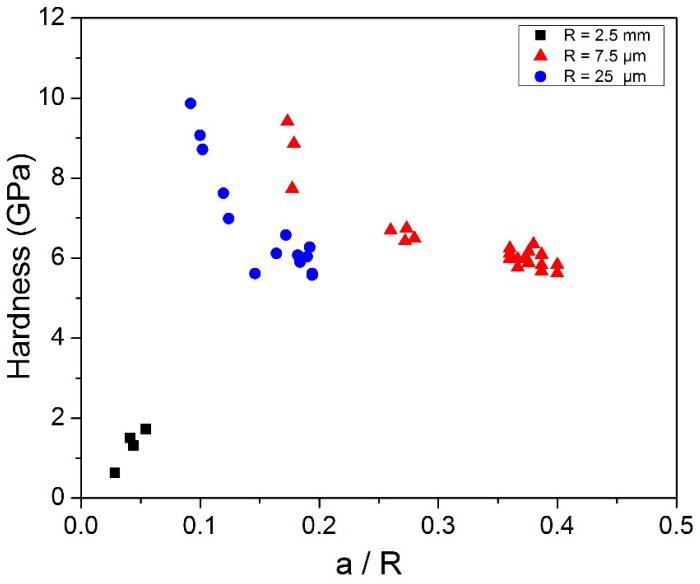

Fig. 4.1.12: Hardness vs a/R plot for 2.5 mm, 7.5 µm and 25 µm tip radius spherical indentations

For all of the spherical indentations, the hardness was calculated by using the applied load divided by the contact area, where the contact area was determined via confocal laser microscope and SEM. For 2.5 mm tip radius spherical indentations, hardness increases with the increase of a/R ratio from 0.03 to 0.05 as shown in Fig. 4.1.12, which is an expected ISE behavior for spherical indentations. Due to STO specimen size limitations, further higher loads 2.5 mm spherical indentations were not conducted.

For both 7.5 µm and 25 µm tip radius spherical indentations, high hardness values were observed as compared to 2.5 mm tip radius spherical indentations. However, a significant decrease in hardness with an increase of a/R ratio was observed for 7.5 µm and 25 µm tip radius spherical indentations, which is an unexpected ISE behavior for spherical indentations. The 7.5 µm and 25 µm tip radius spherical indentations show an increase in cracking with an increase in the a/R ratio (Fig. 4.1.5 and Fig. 4.1.6). The cracking lead to stress relaxation in the material, which consequently results in larger penetration depth than expected and the measured hardness is underestimated. For 2.5 mm tip radius spherical indentations, no cracking was observed (Fig. 4.1.4), therefore, hardness increases with increase of a/R ratio from 0.03 to 0.05 as shown in Fig. 4.1.12. However, at larger indentation depths, cracking is also expected for 2.5 mm spherical indentation, which consequently decreases the hardness. Therefore, the study of ISE using spherical indentation for STO is not feasible due to cracking.

4.1.6 HR-EBSD on Spherical Indentation Experiments

To study the misorientation and GND densities, the HR-EBSD was conducted on 50 mN, R=7.5 µm ball indentations. Fig. 4.1.13 illustrated the HR-KAM and GND density map obtained after removing 300 nm of the material from the surface of an un-etched 7.5 µm spherical indentation.

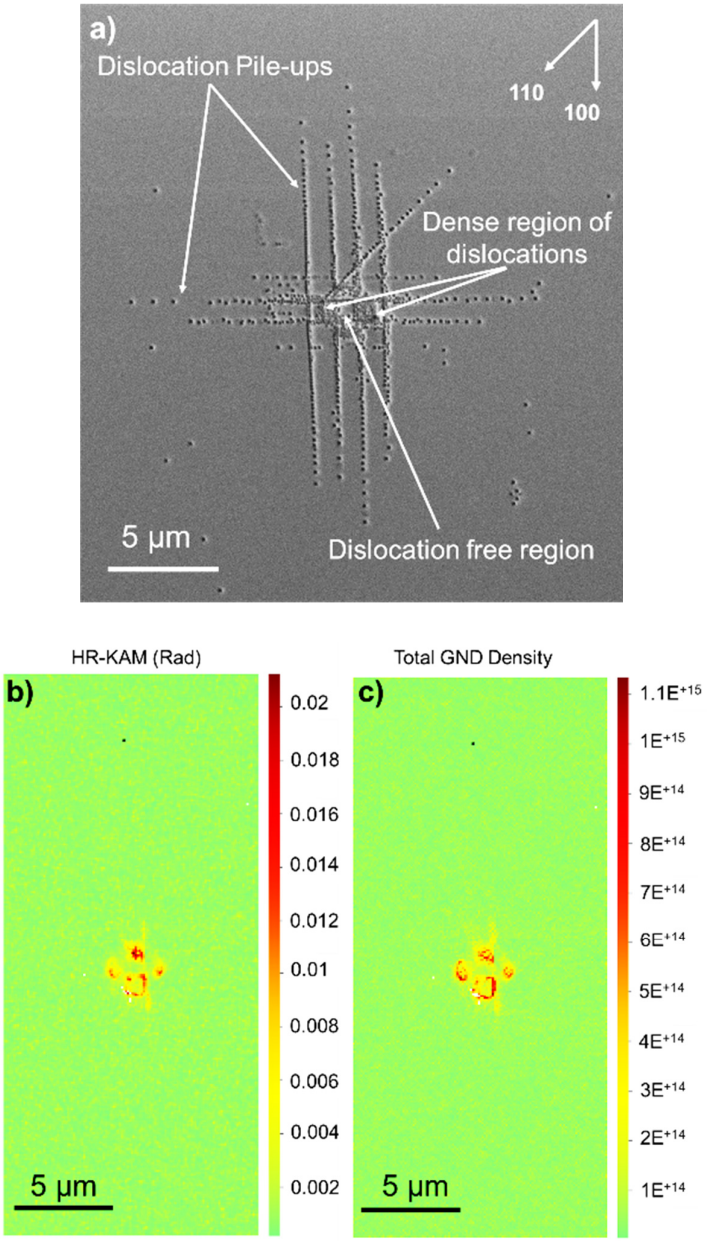

Fig. 4.1.13: 50 mN spherical indentation of R = 7.5 µm, after removing 300 nm of material (a) etched SEM image (b) HR- KAM Map (c) GNDs distribution map

After EBSD, the specimen was etched to reveal the dislocation etch-pit pattern and to compare with EBSD measurements. At 300 nm polishing depth, dislocation pile-ups along <100> and <110> direction can be clearly seen in SEM image along with central dislocation free region, surrounded by the dense region of dislocation density (Fig. 4.1.13a). From the HR-KAM map, maximum misorientation at the corners of spherical contact was observed, which shows a good agreement with the dislocation structure revealed in SEM image. The GNDs map also indicates the higher dislocation densities (8.9×10^{14} m^{-2}) in that particular region.

4.2 Room Temperature Berkovich Indentation Experiments

4.2.1 Incipient Plasticity and Multiple Pop-in Events

Fig. 4.2.1 shows load – displacement (LD) curves for 2 mN nanoindentations obtained via LC method, on a pre-etched STO single crystal specimen. A clear displacement burst at 0.2 mN can be seen for both curves, known as ‘’Pop-in’’ depicting the elastic to plastic transition within the material. In addition to the first pop-in, LD curve shows several multiple pop-in events (indicated by circles in Fig. 4.2.1) at different indentation loads.

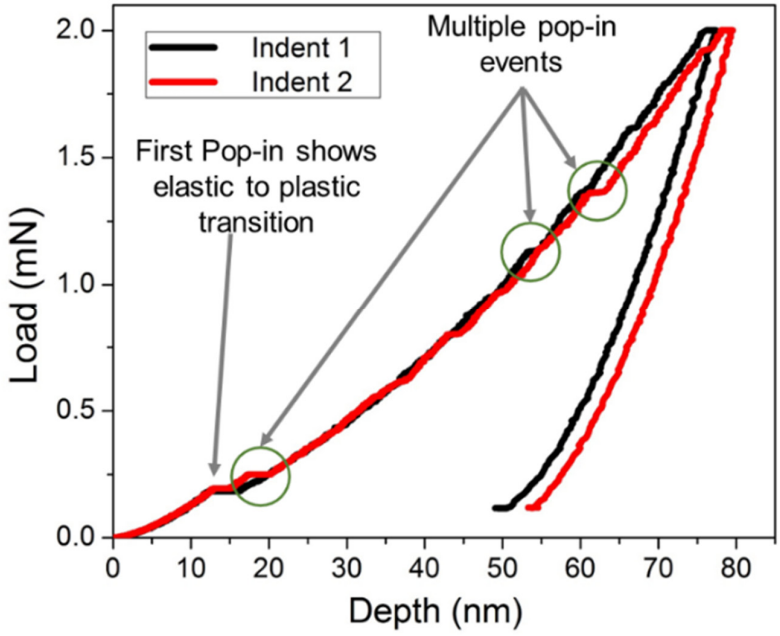

Fig. 4.2.1: Load – Displacement curve of 2 mN indentations showing first pop-in and multiple pop-in events

Before the pop-in, the material deforms purely elastically and no residual impression was found on the surface. Moreover, after etching, no etch-pits were observed in the region of the elastic contact, whereas indentations loaded to just after the first pop-in show a few dislocation etch-pits. The first pop-in loads in Berkovich nanoindentation experiments were found to be quite reproducible (Fig. 4.2.1 and Fig. 4.2.2). From repeated measurements of 200 indents, the average first pop-in load is found to be 0.18 ± 0.02 mN.

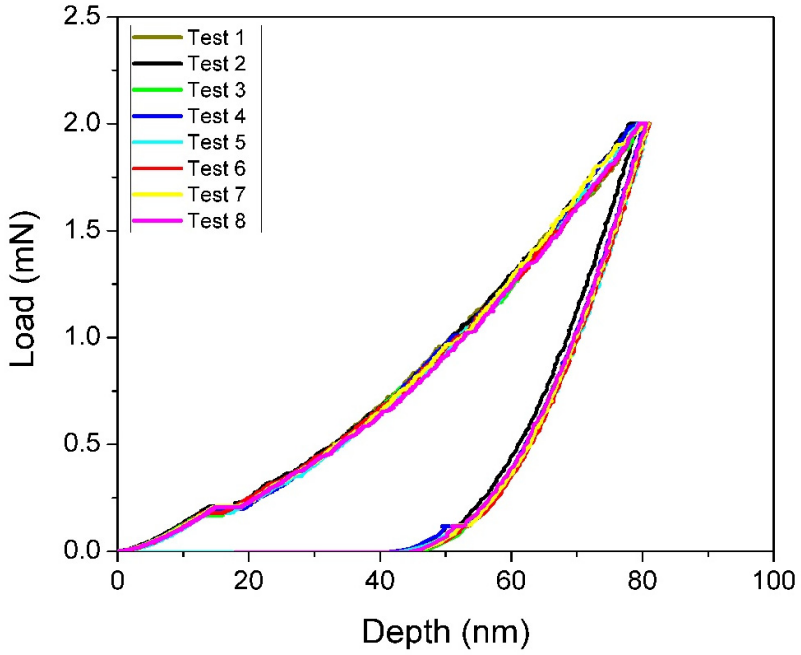

Fig. 4.2.2: Exemplary 2 mN load – displacement curves showing reproducibility of the first pop-in events

At the first pop-in event, the maximum shear stress (τ_{max}) was calculated to be 14.5 ± 0.5 GPa, using the pop-in load of 0.18 ± 0.02 mN, an effective indentation modulus of 264 GPa and an indenter tip radius of 130 nm. Since the shear modulus of STO is 107 GPa, the calculated τ_{max} is very close to the theoretical shear strength ($\frac{G}{2\pi}$) value of 17 GPa. These evidences confirm that the first pop-in event causes the homogeneous nucleation of dislocations underneath the indentations.

Similar to the LC data, the CSM LD curve shows multiple pop-in events as shown in Fig. 4.2.3(a).

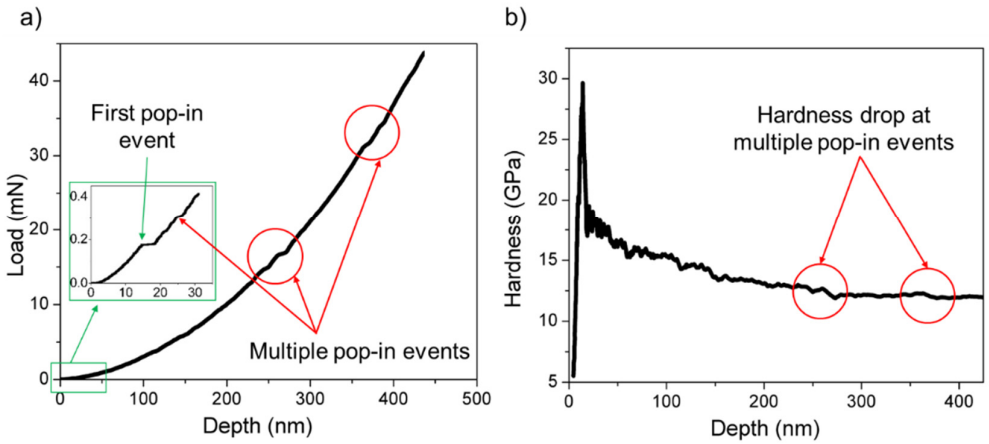

Fig. 4.2.3: CSM 45 mN indentation (a) Load – displacement showing multiple pop-in events (b) Hardness vs indentation depth plot indicating a hardness drop at multiple pop-in events

The continuous loading and unloading of the CSM method facilitate to measure the hardness and stiffness continuously as a function of depth. A clear hardness drop was observed at multiple pop-in events as shown in Fig. 4.2.3b. At smaller indentation loads (< 5 mN), where cracking is absent, these multiple pop-in events can be related to the nucleation of new slip systems, which will be discussed in section 4.2.3. With an increase in indentation load, a significant cracking was observed for Berkovich indentations as shown in Fig. 4.2.4 for the un-etched 45 mN and 400 mN indentations.

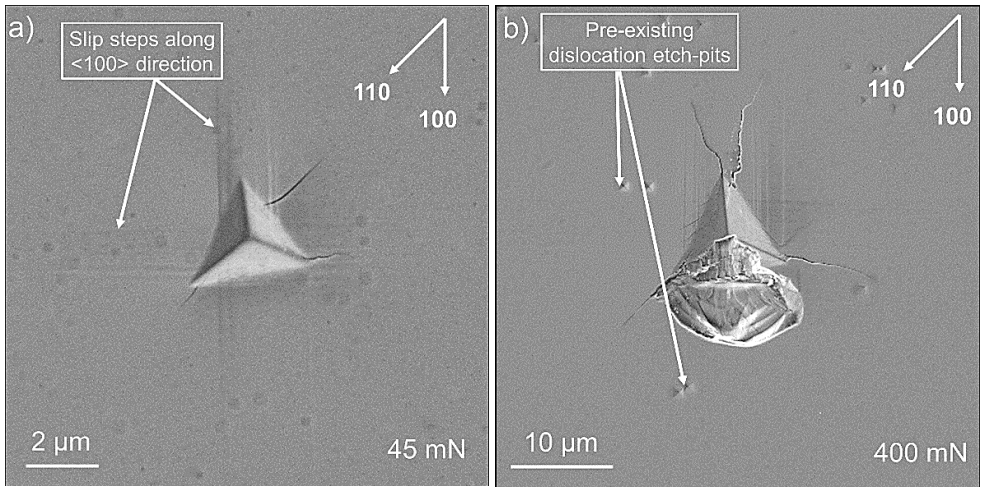

Fig. 4.2.4:Un-etched SEM Berkovich indentations showing slip line only in <100> directions (a) 45 mN (b) 400 mN

Such cracking behavior at larger indentation loads directly influences the nanoindentation data and much larger hardness drops were observed in CSM hardness versus

depth plot, which eventually underestimated the measured hardness as shown in Fig. 4.2.5 for exemplary tests.

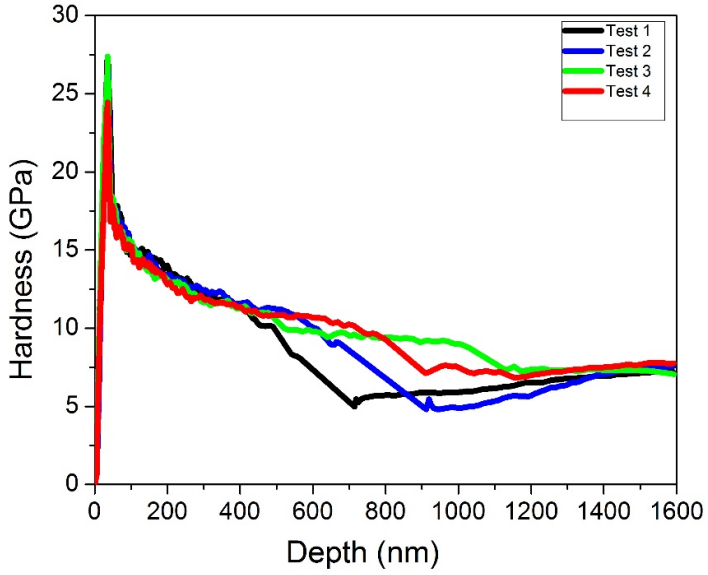

Fig. 4.2.5: CSM hardness vs indentation depth plot showing a significant hardness drop

Therefore, to study the relevance of multiple pop-in events with the nucleation of new slip systems, 2 mN indentation load was chosen due to the absence of cracking. Moreover, similar to spherical indentations, slip steps only in <100> direction for un-etched Berkovich indentations were observed as shown in Fig. 4.2.4 for 45 mN and 400 mN indentations, which suggested that for <100> dislocations, the Burgers vector is perpendicular to the surface. After re-etching the Berkovich indentations, dislocation etch-pits in both <100> and <110> direction were observed (Fig. 3.3.1 and Fig. 4.2.6), which indicate that for <110> dislocations, the Burgers vector is parallel to the surface and dislocations emerge with a pure edge character. Therefore, <110> dislocations do not leave steps behind the surface and etching was required to make them visible.

4.2.2 Dislocation Structure Evolution around Berkovich Indentations

The dislocation etch-pits structure around the Berkovich indentations was revealed after etching the (001) STO single crystal for 10 – 20 sec. A four folded etch-pit symmetry was observed, where dislocations were aligned along <010> and <110> directions as shown in Fig. 4.2.6 (f) for a 10 mN indent. This well-defined asterisk-shape along <100> and <110> directions forms, step by step, from lower load to higher load indentations as illustrated in Fig. 4.2.6(a-f). For 1 mN indentations, only a few small dislocation pile-ups were formed, along

which single etch-pits can be observed. The pile-up #I and #II in Fig. 4.2.6(a) for a 1 mN indentation clearly belong to <110> directions. The etch-pits labelled as A and A* for 1 mN and 2 mN, respectively, can be identified as single dislocation (Fig. 4.2.6a and c). For such etch-pits, the dislocation pile-ups are not fully developed.

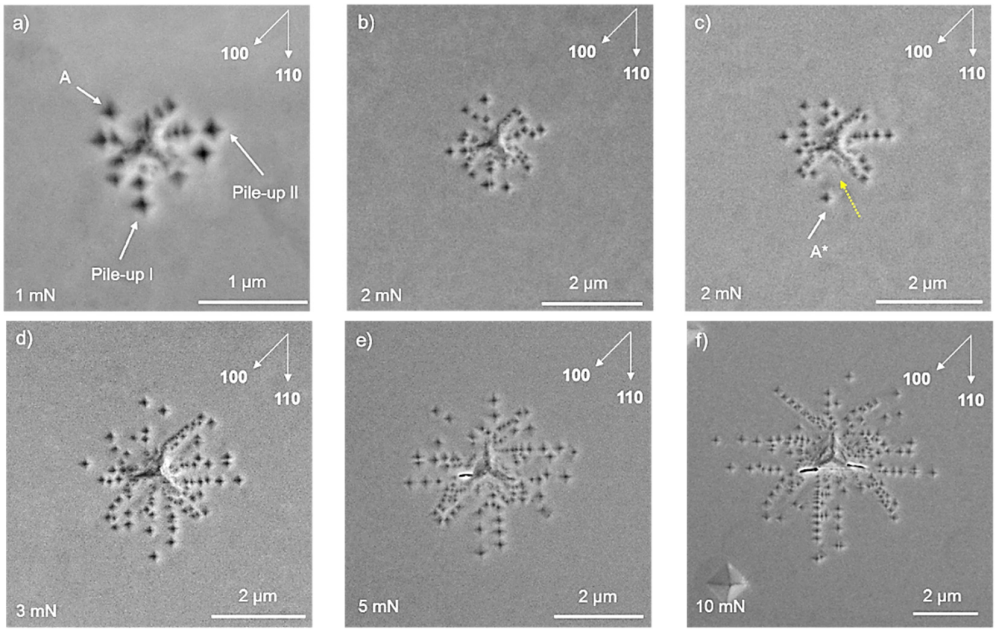

Fig. 4.2.6: Etched SEM Berkovich indentations on the specimen surface (a) 1mN (b-c) 2mN (d) 3mN (e) 5mN (f) 10mN

The dislocation etch-pit patterns around the Berkovich indentations were found to be stochastic at the same load. Even though the same single crystal STO was used and the indentations were closely spaced, we find a random occurrence of the dislocation pile-ups around the indent (Fig. 4.2.6b and c). The dislocation pile-up #I, which can be clearly identified in <110> etch-pit directions for 1 mN indentation was found missing against one of the 2 mN indentations (Fig. 4.2.6c, indicated by dotted arrow). However, for another 2 mN indentation, few longer etch-pit pile-ups on the same position can be seen (Fig. 4.2.6b).

4.2.3 Multiple Pop-ins and Dislocation Pile-up Evolution

As explained in section 4.2.1, after the first pop-in event, the STO load displacement curve shows the series of multiple pop-in events (Fig. 4.2.1) for 2 mN indentation load. Multiple pop-in events in a LD curve can occur for several reasons like fracture of the oxide film on the surface of the specimen, cracking or phase changes during indentation. However,

STO retains its cubic symmetry at room temperature without any phase change and no cracking was observed below 5 mN for Berkovich indentations. Therefore, 2mN indentations are chosen for the discussion of multiple pop-in events. The first pop-in occurred at 0.2 mN for both 2 mN indentation curves, but the loads for multiple pop-in events were found stochastic for both loading curves (Fig. 4.2.1). The dislocation etch-pit pattern around the same 2 mN indentations were also found different as shown in Fig. 4.2.6(b) and (c). The difference in dislocation etch-pit pattern and stochastic nature of multiple pop-in loads suggests that the occurrence of multiple pop-in events could be related to the nucleation and initiation of new slip systems during the pop-in, after which the glide plane is active and dislocation loops are emitted forming larger dislocation pile-up lengths. The scatter in multiple pop-in event loads and dislocation pile-ups could be due to the complex interaction of dislocations in the center region of the plastic zone from, which dislocation pile-ups are emitted.

4.2.4 3D Dislocation Structure Evolution underneath the Berkovich Indentations

For studying the 3D dislocation structure evolution underneath the Berkovich indentations, sequential polishing and etching were applied to remove ~600 nm and ~1200 nm of material from the surface of the specimen for 5 mN and 25 mN indentation, respectively, as shown in Fig. 4.2.7. After removing ~600 nm of material, a box-shaped region of high dislocation density can be clearly identified for both indentation loads. The size of this box-shaped region was also found to be increasing with polishing depths, instead of being constant. In the center-region of high dislocation density, etch-pits with a spacing of ~40 nm were resolved. However, the shape of the individual etch-pit in such a complex entangled network cannot be resolved.

With increasing polishing depth, a decrease in dislocation pile-up length was observed, which ends up with a box-shaped region of high dislocation density indicated by a yellow box for 5 mN indentation (Fig. 4.2.7b). Further polishing of the 5 mN indentation revealed that dislocation etch-pits in the central dense region of plastic zone disappeared, resulting in a dislocation free region surrounded by a box-shaped dislocation etch-pit pattern (indicated by a green box). The pattern was aligned in <100> directions and the dislocation could lie on either $\{010\}_{90^\circ}$ (depicting 90° inclination with respect to the surface) or $\{110\}_{45^\circ}$ (indicating 45° inclination with respect to the surface). To clarify this, the etch-pit shape, as well as, the 3D configuration of the dislocation pile-ups need to be considered.

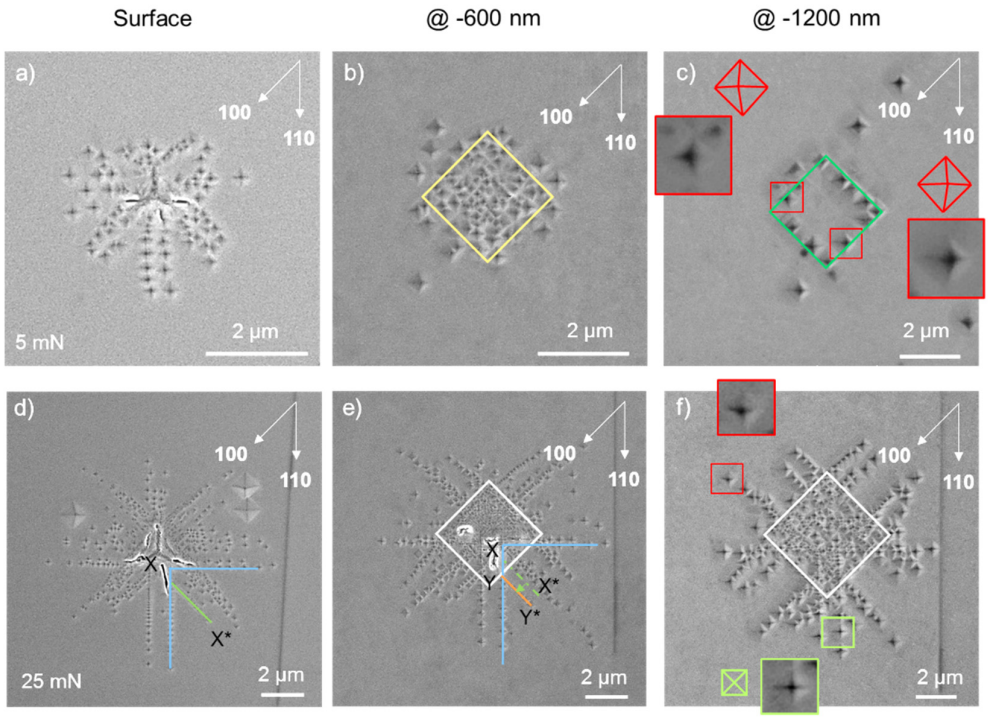

Fig. 4.2.7: Etched SEM Berkovich indentations at surface and different polishing depths for (a-c) 5 mN (d-f) 25 mN

For <110> dislocation pile-ups, square-shape etch-pits with sharp centered bottom were observed (Fig. 4.2.7f), indicating that the dislocation line is perpendicular to the surface, lying on $\{110\}_{90°}$. However, for <100> pile-ups, off-centered dislocation etch-pits were found (Fig. 4.2.7c and f), indicating that the intersecting dislocation line has an inclination to the surface and the dislocation line can lie on $\{110\}_{45°}$ planes. Further evidence for the $\{110\}_{45°}$ glide plane was found in the relative position of the dislocation pile-up XX* for 25 mN indentation, as shown in Fig. 4.2.7d. The two blue lines in <110> etch-pit direction (Fig. 4.2.7) were chosen as the reference lines for tracking <100> dislocation pile-up XX*, since <110> dislocation pile-up lie only on $\{110\}_{90°}$ planes and will not change their position after polishing. As shown in Fig. 4.2.7e, after removing 600 nm of material, the dislocation pile-up at XX* position was shifted to the YY* position. The distance between line XX* and YY* was also found to be equal to the polishing depth, which confirms that the <100> dislocation etch-pit pile-ups lie on $\{110\}_{45°}$ plane. This evidence also confirms that during Berkovich indentations, slip occurs along $\langle 110 \rangle \{110\}$ system, which is in good agreement with the literature and facilitates GNDs measurements via HR-EBSD that require predefined slip systems.

In the light of aforementioned experimental evidence (Fig. 4.2.6 and Fig. 4.2.7), the evolution of dislocation pile-ups with increasing indentation load around the Berkovich indentations is schematically illustrated in Fig. 4.2.8.

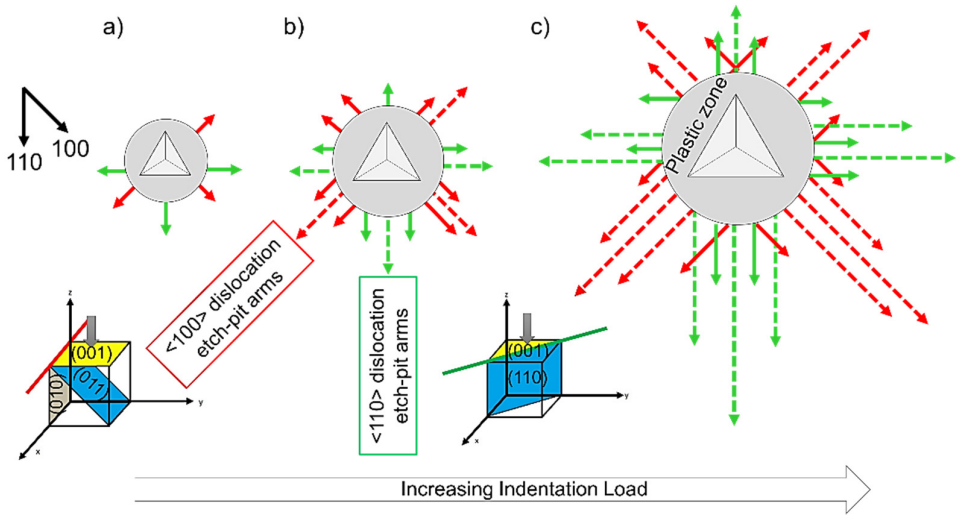

Fig. 4.2.8: Schematic of dislocation pile-ups evolution around Berkovich indentation with increasing load

At low indentation load (Fig. 4.2.8a), a small plastic zone with high dislocation density can be seen from which few dislocation pile-ups are emitted along <010> and <110> directions. With increasing indentation load [Fig. 4.2.8(b) and (c)], the size of the plastic zone increases and more dislocation pile-ups are emitted from the center region (indicated by solid arrows) along with the increase in the length of pre-existing dislocation pile-ups (indicated by dotted arrows).

4.2.5 Elastic Strain Fields around Berkovich Indentations

Fig. 4.2.9 illustrates the normal elastic strain component (ε_{11}, ε_{22}, ε_{33}) and shear elastic strain component (ε_{12}) maps, obtained from HR-EBSD analysis on 5 mN indentation, after removing 80 nm of material from the surface of the specimen.

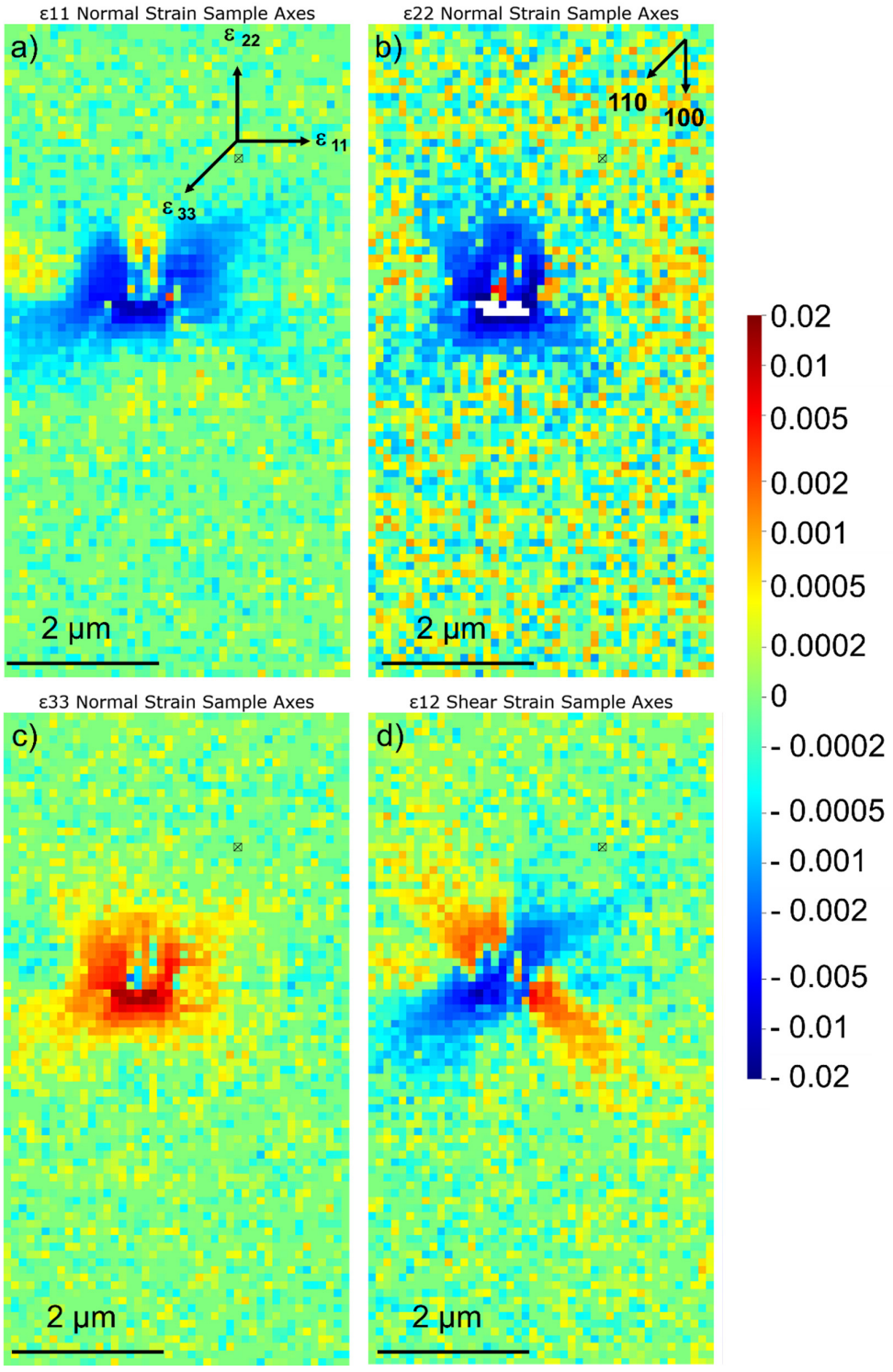

Fig. 4.2.9: Selected elastic strain component maps for 5 mN non-etched Berkovich indentations, after removing 80 nm of material from the surface of the specimen

The elastic normal strains show the expected behavior for an indentation plastic zone with compressive strains in ε_{11} and ε_{22}, which are balanced by tensile strains in the ε_{33} component. In the ε_{12} shear strain map, positive (red) and negative (blue) shear strains can be clearly identified only along <110> directions. For that particular direction, the slip is associated with ⟨110⟩{110} systems thus the dislocations emerge with a pure edge character, which leads to positive and negative elastic shear strains only in <110> directions.

4.2.6 Indentation Size Effect and Quantification of Dislocation Microstructure

Fig. 4.2.10 shows the hardness as a function of maximum indentation depth, evaluated from cyclic load – displacement Berkovich nanoindentation data using a maximum load of 100 mN.

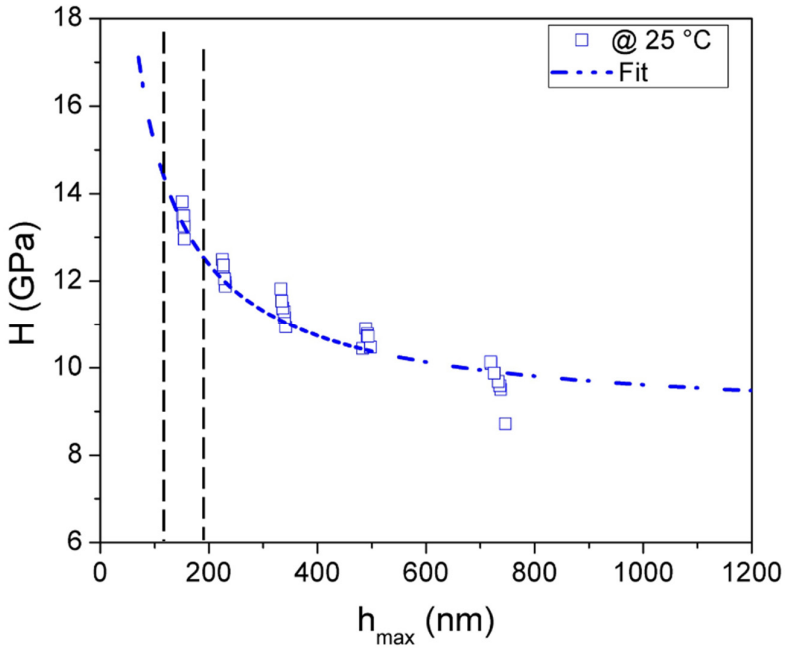

Fig. 4.2.10: Hardness as a function of maximum indentation depth evaluated from cyclic 100 mN nanoindentation experiments

For 5 mN and 10 mN indentations, the hardness was measured to be ~ 14 GPa and ~ 12.7 GPa, respectively, via Oliver-Pharr method (indicated by dotted line in Fig. 4.2.10). Moreover, H^2 and $1/h_{max}$ plot (Fig. 4.2.11) shows a linear behavior, which is in good agreement with the Nix – Gao model.

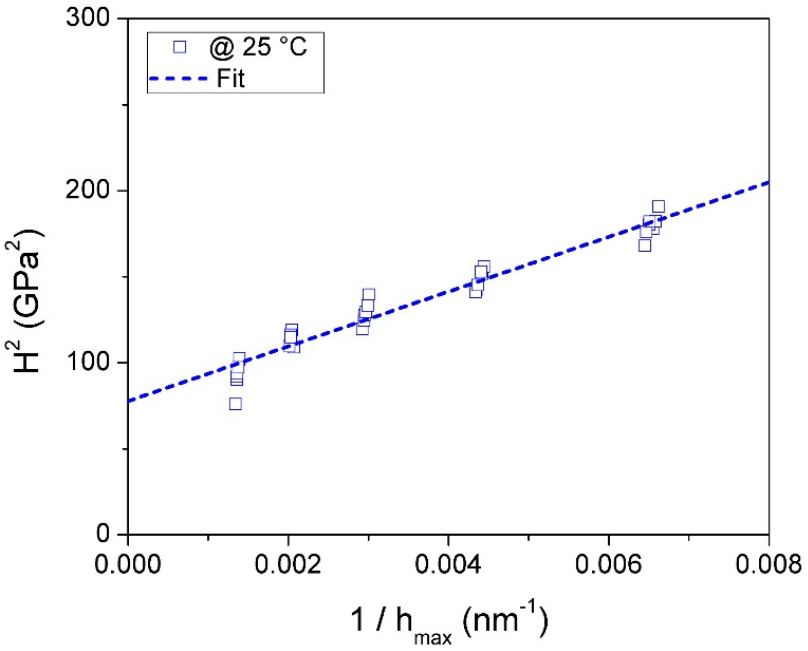

Fig. 4.2.11: Nix –Gao plot obtained from 100 mN cyclic load control nanoindentation experiments

The dislocation structure underneath the Berkovich indentations was quantified after removing 80 nm and 180 nm of material from 5 mN (~ 40 nm) and 10 mN (~ 90 nm) indentations, respectively, using dislocation etch-pit positions and HR-EBSD analysis. At these polishing depths, both 5 mN and 10 mN indentations have the same indentation to polishing depth ratio, which is important for comparing the dislocation structure at different loads. Fig. 4.2.12 shows the SEM images of 5 mN and 10 mN indentations after removing 80 nm and 180 nm of material, respectively, along with digitized images, which were used for etch-pit analysis.

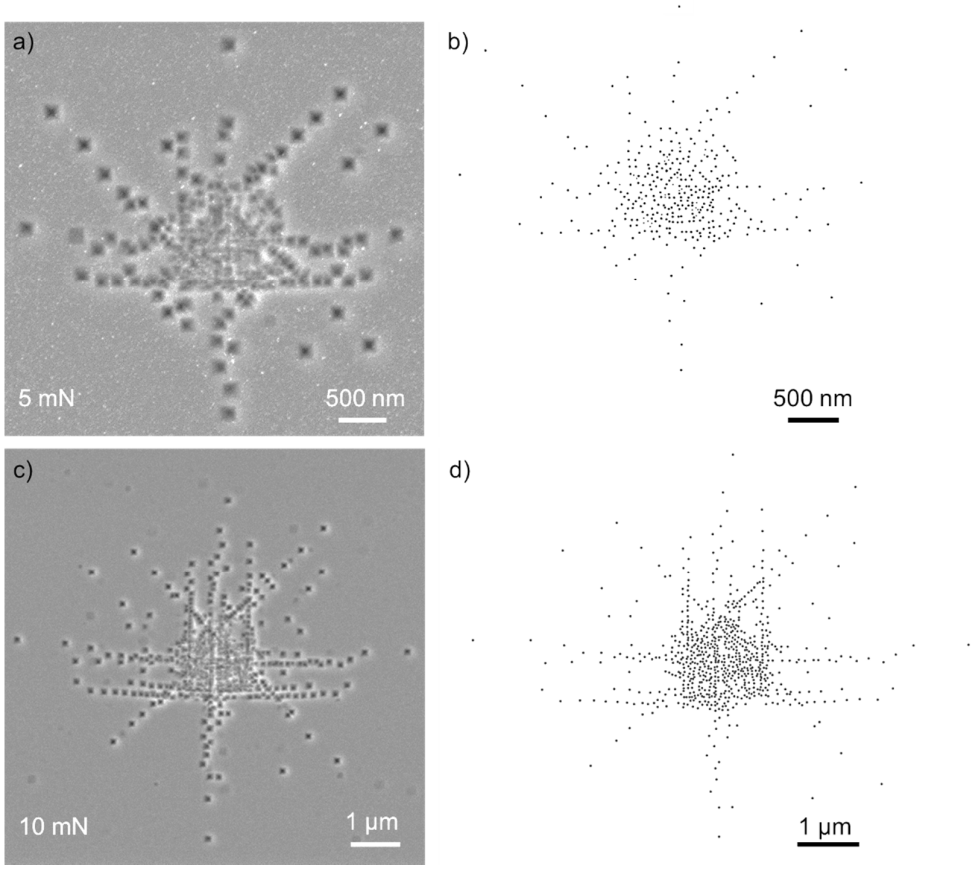

Fig. 4.2.12: 5 mN and 10 mN Berkovich indentations after removing 80 nm and 180 nm of material from the surface of the specimen, respectively, (a and c) SEM images showing dislocation etch-pit structure, (b and d) digitized images

The contact radii were measured on the pristine indentations to be 0.5 µm and 0.9 µm for 5 mN and 10 mN, respectively, indicated as dotted circles in Fig. 4.2.13. These radii were used to normalize the size of the plastic zone for different loads.

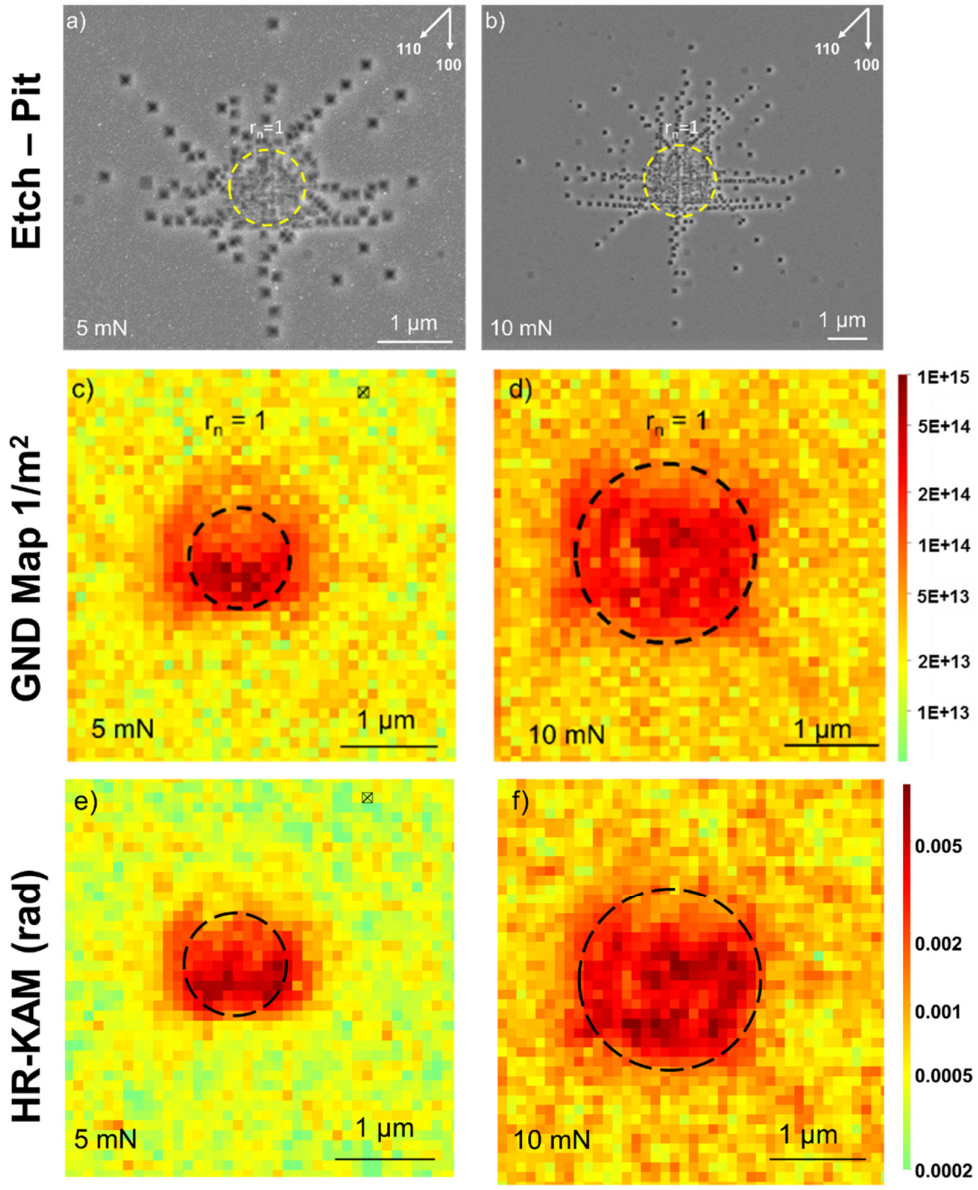

Fig. 4.2.13: 5 mN and 10 mN Berkovich indentations after removing 80 nm and 180 nm of material from the surface of the specimen, respectively, (a-b) SEM images showing dislocation etch-pit structure, (c-d) GNDs distribution map obtained from HR-EBSD, (e-f) HR-KAM map in radian obtained from HR-EBSD analysis

To calculate the dislocation line length per unit volume from etch-pit analysis, the relation $L_V = 2P_A$, (with P_A being the number of etch-pits per unit area) was used, which assumes a random orientation of dislocations [123]. Given the limited number of slip systems in STO and the results above on the 3D dislocation structure, this assumption may not be fully valid. However, there is no analytical approach to a more accurate stereological correction factor, as this would require detailed knowledge on the shape and population of dislocations on each slip system. For 5 mN and 10 mN indentations, the etch-pit analysis of dislocation

density in the dotted circular region results in 5.56 x 10^{14} m^{-2} and 3.96 x 10^{14} m^{-2}, respectively, showing that the dislocation density for 5 mN indentation is ~1.4 times higher compared to 10 mN indentations. For both indentations, the ratio of experimental hardness ($\frac{H_{5\,mN}}{H_{10\,mN}} = \frac{14\,GPa}{12.7\,GPa} = 1.10$) and the square root of dislocation densities ($\frac{\sqrt{\rho_{5\,mN}}}{\sqrt{\rho_{10\,mN}}} = 1.18$), measured for the dense zone are quite similar which corroborates the measured dislocation densities.

Fig. 4.2.13 (c-d) illustrates the GND density distribution maps obtained from cross-correlation HR-EBSD analysis of the same 5 mN and 10 mN indentations at 80 nm & 180 nm polishing depths before etching. The GND maps show only a region of high dislocation density, but no pile-ups around the central region of the indentation can be observed, which were visible after etching (Fig. 4.2.13a - d). Around the central region with high GND density, the maps still indicate a considerable GND density even though no etch-pits were visible in this area, which is attributed to the relatively high noise level of the method (Fig. 4.2.13c and d). The noise level was calculated by averaging over all points, excluding the high GND density region. For 5 mN and 10 mN indentations, the noise was found to be 2.5 x 10^{13} m^{-2} and 3.1 x 10^{13} m^{-2}, respectively. Fig. 4.2.13 (e-f) shows the HR-KAM map obtained from cross-correlation HR-EBSD analysis for the same indentations, which shows higher misorientation in the central region of indentations where a dense region of dislocation was observed in etch-pit and GNDs analysis.

Similar to the etch-pit analysis, the average GND density in the dotted circular region, which corresponds to the contact radius is higher (~ 1.2 times) for 5 mN indentations compared to 10 mN indentations. In order to not just rely on one data point, dislocation densities were calculated for 11 zones ranging from 0.2 µm to 1.7 µm radii for both indentations. For a better comparison of the dislocation structure at both loads, the results obtained from each zone were normalized by the contact radius of the corresponding indentation as shown in Fig. 4.2.14.

Both HR-EBSD and etch pit analysis show for each normalized radius a higher dislocation density at smaller loads. The dislocation density quantified from etch-pit analysis includes both SSDs and GNDs, whereas HR-EBSD provides only the minimum GND density necessary to generate the measured orientation distribution. Again, etch-pit and HR-EBSD analysis show the same trend, but different quantities, with the GND densities from HR-EBSD being approx. 40% lower than the total dislocation density quantified by the etch-pit analysis. These results were in good agreement with an HR-EBSD study on Ni single crystals under

uniaxial compressing, also showing that about half of the total dislocation density (calculated by the Taylor equation) were GNDs [124].

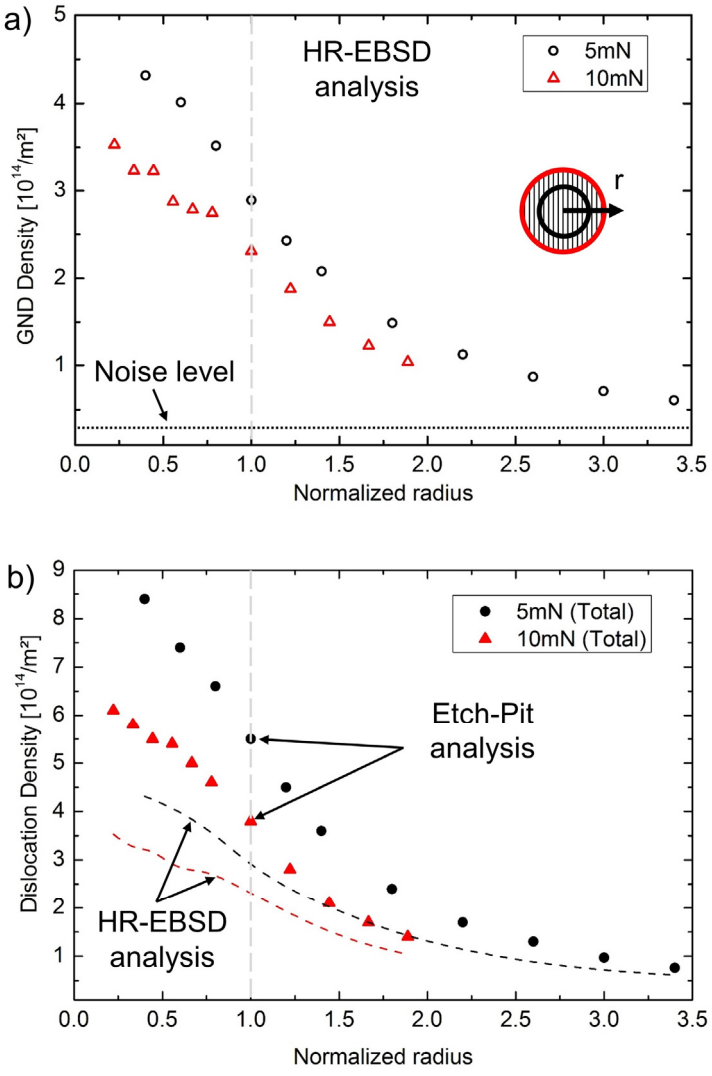

Fig. 4.2.14: Dislocation density in each zone for 5 mN and 10 mN indentations at polishing depths of 80 nm and 180 nm, respectively, (a) HR-EBSD analysis (b) Etch-pit (filled circles & triangles) and HR-EBSD (dotted lines) analysis

These results qualitatively validate the assumption in the Nix-Gao model that lower indentation depths result in higher GND densities. On the other hand, it needs to be mentioned that the strain field and dislocation density distribution around nanoindentations are quite complex and simplified models can only partly explain the size effects.

4.2.7 Hardness – Yield Strength Discrepancy

As briefly mentioned in Section 1.1, STO, surprisingly, exhibits a very high macroscopic hardness of 9.5 GPa, which is unexpected for a material with a yield strength of ~120 MPa. The reason for this large discrepancy can be understood from the results obtained from the dislocation etch-pit analysis of Berkovich indentations. Taylor's equation (Eq. 2.2.19) can be used to determine the hardness from the quantified etch-pit dislocation density.

Patterson et al. [23] calculated the elastic modulus of (001) oriented STO single crystal to be 264 GPa at 25 °C by resonant frequency and damping amplifier equipment (RFDA, HT1750, IMCE nv). A Poisson's ratio of 0.237 [25] was used in this analysis, which resulted in a shear modulus, G, of 107 GPa at 25 °C. A Burgers vector of 5.5 x 10^{-4} µm and H_{fric} of 0.63 GPa [22] was used in the calculation. Assuming that the deformation resistance is attributed to the dislocation density in a plastic zone with a diameter that equals the contact radius, the present etch-pit analysis provides the sum of ρ_{SSD} and ρ_{GND}(5.56 x 10^{14} m^{-2} and 3.96 x 10^{14} m^{-2} for 5 mN and 10 mN, respectively). However, the M, C and α are the unknown quantities for STO and difficult to determine. Assuming standard numbers of C and M (~ 3) for cubic materials, it turns out that a high dislocation interaction coefficient of ~ 1 is required to balance the Taylor equation. This is not implausible considering the complex arrangement and high density of dislocations in the plastic zone. Using these values, the Taylor hardness was determined to be 13.2 GPa and 11.3 GPa for 5 mN and 10 mN indentations, respectively, which is close to the hardness measured via the Oliver – Pharr method (i.e., 14 GPa and 12.7 GPa for 5 mN and 10 mN indentations, respectively).

Further simulation based approaches are needed to assess the unknown parameters. At this stage, it can be stated that the discrepancy of low yield strength and high hardness in STO stems from a high dislocation density region present underneath the indentations. In addition to that, the complex interaction in such a region of high dislocation density leads to the formation of sessile dislocations [25], which contribute further to such high hardness values for a low yield strength material.

4.3 Elevated Temperature Berkovich Indentation Experiments

4.3.1 Incipient Plasticity and Indentation Hardness at 25 °C and 350 °C

The nanoindentation experiments conducted with sapphire Berkovich indenter tip at 25 °C and 350 °C were strongly influenced by the pre-existing dislocations. Similar to spherical indentation experiments, the indentations performed close to pre-existing etch-pits end up with a residual impression, whereas, the indentations away from the pre-existing etch pits end up with the elastic contact. Fig. 4.3.1a shows 50 mN nanoindentations at 25 °C, where for indent 1, a residual impression along with few etch-pits can be clearly seen, whereas the contact is elastic in the case of indent 2 (shown as a circle).

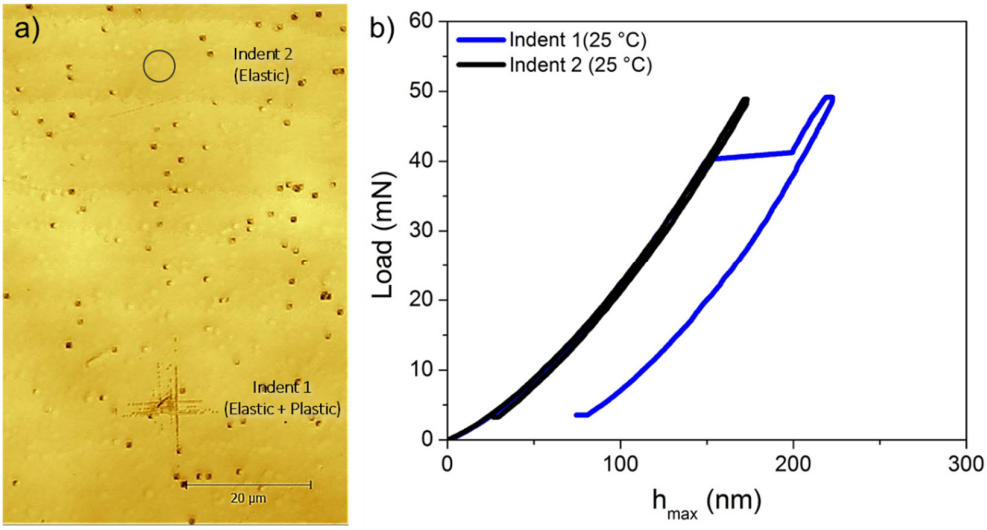

Fig. 4.3.1: (a) Laser microscope image for 50 mN indentations at 25°C (b) Load – displacement curve of indent 1 and 2 at 50 mN

The load-displacement curves for the same two indents are shown in Fig. 4.3.1b with a "pop-in event" depicting the elastic to plastic transition within the material. Moreover, a significant load-displacement curve shift (before pop-in) between 25 °C and 350 °C was observed, indicating bluntness of the tip during the indentation as shown in Fig. 4.3.2 for exemplary 50 mN indentations.

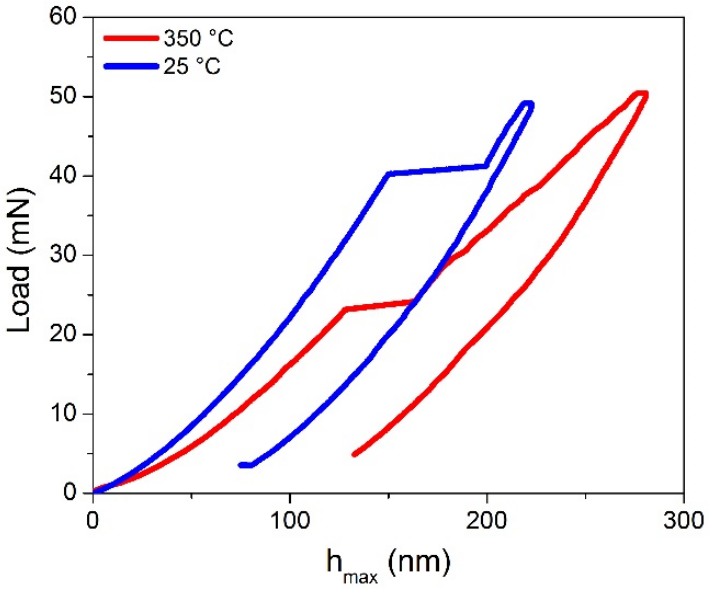

Fig. 4.3.2: Load – displacement curve of 50 mN Berkovich indentations at 25 °C and 350 °C

Due to change in tip geometry during the indentations, the hardness for each indentation was calculated from the residual impressions via laser microscope imaging. The hardness as a function of the displacement into the surface is shown in Fig. 4.3.3(a) for 25 °C and 350 °C indentations. For better visualization of the displacement data, a logarithmic scale was used. At lower indentation depths, 25 °C indentations exhibited a higher hardness as compared to 350 °C indentations, which indicate that at 350 °C size effects in STO are much smaller as compared to 25 °C.

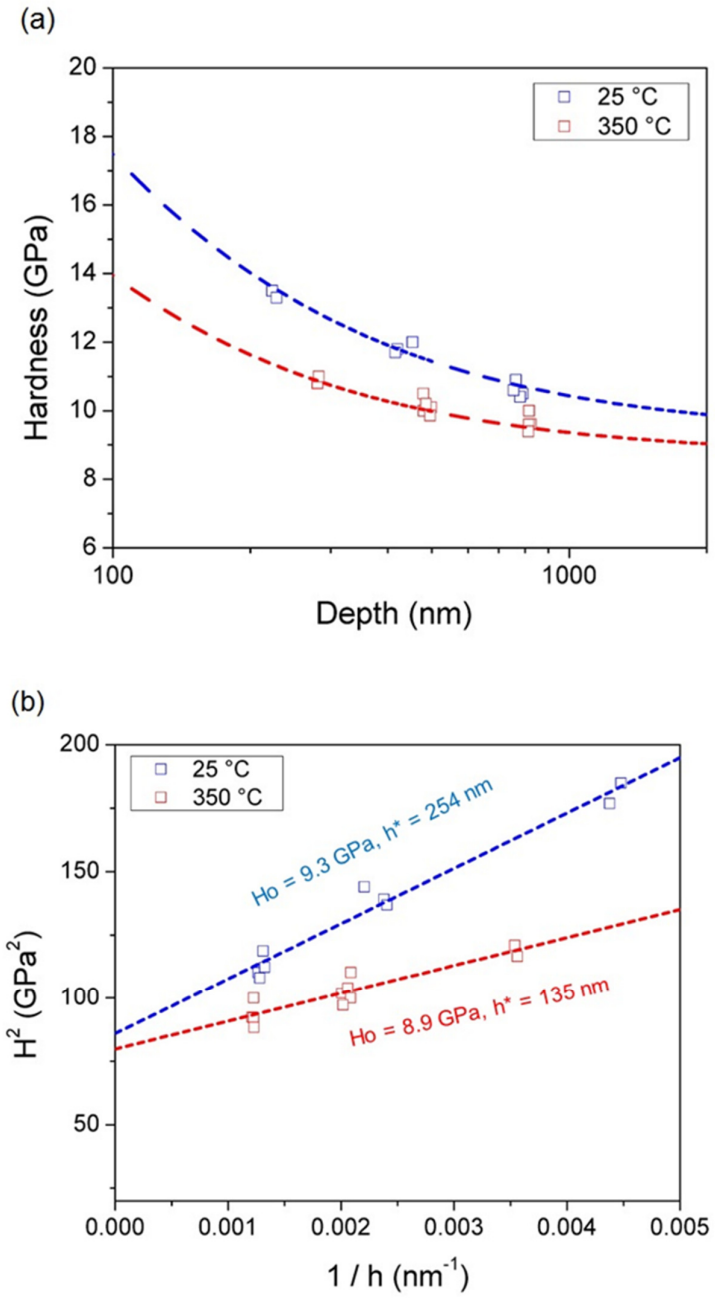

Fig. 4.3.3: ISE in single crystalline STO at 25 °C and 350 °C (a) Hardness as a function of depth (b) Nix – Gao plot

Fig. 4.3.3(b) shows the Nix-Gao plot from which H_o (macroscopic hardness) and h^* (intrinsic plasticity length scale) were calculated from the y-intercept and slope of the linear fit, respectively, for 25 ˚C and 350 ˚C indentations. The macroscopic hardness H_o was found to be 9.3 GPa and 8.9 GPa for 25 ˚C and 350 ˚C, respectively, which indicates a small difference

of H_o values between aforementioned temperature regimes. However, a considerable decline in h^* from 254 nm to 135 nm was observed with increase in temperature.

The significance of h^* can be understood by using modified Nix-Gao model, where Durst et al. introduced a factor f which denotes the size of the storage volume of GNDs. The Eq. 2.2.21 suggested that the characteristic indentation length scale h^* depends on the storage volume of GNDs f or dislocation density of SSDs. Therefore, to accommodate the decrease in h^*, either f or ρ_{SSD} or both should increase with temperature. As briefly mentioned in section 2.2.3, the Nix-Gao model does not explicitly take into account the thermal effects, therefore, other physical explanations of h^* and H_o of temperature dependency are also possible.

4.3.2 Dislocation Etch-Pit Structure at 25 °C and 350 °C

Fig. 4.3.4 illustrates an exemplary dislocation etch-pit structure for 200 mN Berkovich indentations at 25 °C and 350 °C.

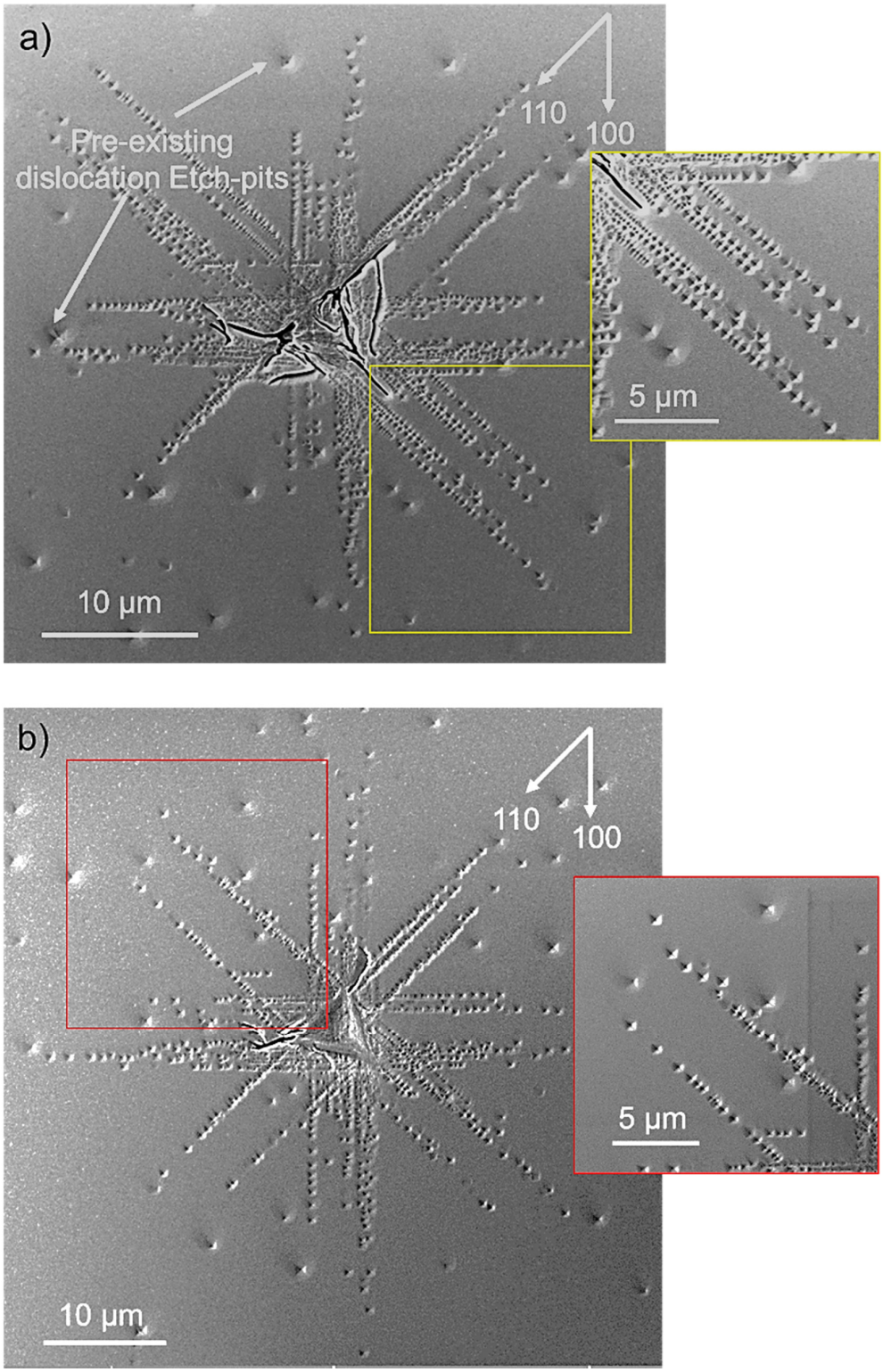

Fig. 4.3.4: SEM image of etched 200 mN Berkovich indentations at (a) 25 °C (b) 350 °C with inset regions

The average dense region of dislocations along with dislocation pile-ups was found larger for 200 mN (47.3 ± 2.1 µm) and 100 mN (36.13 ± 1.3 µm) indentations at 350 °C as

compared to 25 °C, 200 mN (40.5 ± 1.2 μm) and 100 mN (27.3 ± 1.2) indentations, respectively.

Moreover, the number of dislocations per pile-up was determined to be lower for 350 °C indentations as compared to 25 °C indentations. For this analysis, only larger dislocation pile-ups (with a/r > 5) were considered where 'a' is the contact radius and 'r' is the radial distance from the center of indent. The average number of dislocations per pile-up was measured to be 2.3 ± 0.4 μm^{-1} and 1.5 ± 0.1 μm^{-1} at 25 °C and 350 °C, respectively. Furthermore, a larger spacing between the consecutive outermost dislocations in pile-ups was observed for 350 °C as compared to 25 °C indentations (Fig. 4.3.4).

4.3.3 Dislocation Pile-up Model for Estimation of Lattice Frictional Stress

The model proposed by Gaillard et al. [93], where the equilibrium positions of dislocation etch-pits were used to estimate lattice frictional stress was adopted. They developed the model for estimating lattice friction in the case of the onset of plasticity just after pop-in using spherical indenters and used elastic Hertzian stress fields to estimate the contact stresses. The difficulty comes in the form of the applied indentation stress field, which is elastic-plastic for the current indentations. So, the analysis herein was modified for elastic-plastic pyramidal indentations by extending the description of the applied shear stress, τ_a, for a fully developed plastic zone with Hill's solution [125] of the expanding cavity model. The shear stresses acting on the elastic region surrounding the plastic zone scale with a functional form of:

$$\tau_a = F\,\frac{Ha^3}{r^3}, \qquad \textit{(Eq. 4.3.1)}$$

here, H is the hardness, a is the contact radius and r is the radial distance from the center of the indent to dislocation position. Hill's model is an oversimplification for considering the absolute magnitude of the stress field around indentations in single crystals. Therefore, a scaling factor F has been introduced in Eq. 4.3.1 for empirically achieving the best description of the stress distribution from a given dislocation pattern. The details of fitting this factor with actual observed dislocation spacing will be explained in following paragraphs.

The elastic modulus of STO in the <001> direction was calculated to be 268 GPa from single crystal elastic constants [126]. A value of 264 GPa and 238 GPa was found by resonant frequency and damping amplifier equipment (RFDA, HT1750, IMCE nv) [23] for 25 °C and 350 °C, respectively. A Poisson's ratio of 0.237 [25] was used in this analysis, which resulted

in a shear modulus, G, of 107 GPa at 25 °C and 96 GPa at 350 °C. A Burgers vector of 5.5 x 10^{-4} µm was used in the calculation. The lattice parameter change due to thermal expansion was less than 1% and therefore neglected in the analysis.

Fig. 4.3.5a shows a schematic of a Berkovich indentation in a (001) oriented STO single crystal in which a dense indentation plastic zone can be observed along with the extended dislocation pile-ups aligned along <010> and <110> directions. As explained in section 4.1.2 and 4.2.4 for spherical indentations and Berkovich indentations, respectively, that the dislocation lying along <110> directions represent the straight dislocation lines on $\{110\}_{90}$ glide planes perpendicular to the surface and emerge with a pure edge character. Therefore, these dislocation pile-ups were chosen for the calculation of lattice frictional stresses. Moreover, for such glide system image forces, τ_{im}, are considered to be zero [93]. On the other hand, the dislocation pile-ups in <100> directions could lie on either $\{010\}_{90}$ glide planes perpendicular to the specimen surface or $\{110\}_{45}$ planes inclined at an angle of 45° to the surface. Due to this complication, these dislocation pile-ups were not considered in the current analysis. In order to avoid the contribution of nearest parallel dislocation pile-ups, only isolated pile-ups were taken into account for the frictional stress calculations. Fig. 4.3.5b. schematically illustrates the interaction between the applied stresses, τ_a, dislocation-dislocation interaction stresses, τ_d, as well as the lattice frictional stress, τ_f.

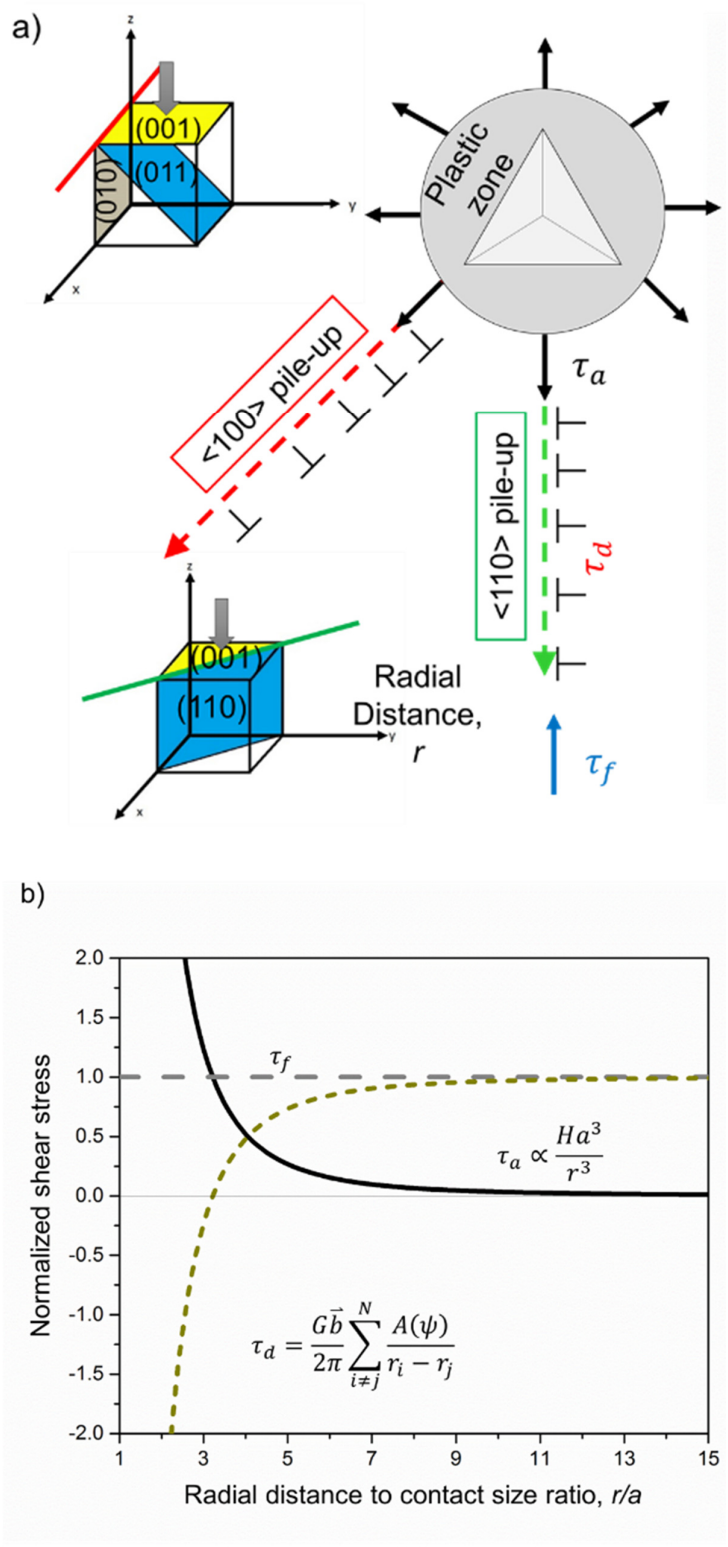

Fig. 4.3.5: Schematics of (a) the plastic zone around a Berkovich indentation along with dislocation pile-ups in characteristic slip directions and of (b) the combined effect of the applied, frictional and dislocation-dislocation interaction shear stresses

The frictional stress is assumed to be constant for a given glide system. The applied stress from the elastic-plastic indentation decreases as $1/r^3$. The applied stress will push the dislocations apart and is balanced by dislocation-dislocation interactions as well as the frictional stress. In this example, at r/a >10, the effect of τ_a is almost negligible, which suggests that at this particular stage only Peach-Koehler forces are resisting lattice frictional stresses.

Experimentally, it is expected that at elevated temperatures, the dislocation pile-up will be influenced by the change in the lattice friction. For estimating the influence of the lattice resistance on a dislocation pile-up, the equilibrium positions of 24 edge dislocations have been calculated for H = 12.5 GPa, τ_{f1} = 30 MPa and τ_{f2} = 60 MPa. Under the equilibrium conditions, the higher frictional stress leads to shorter dislocation pile-up as compared to lower frictional stress as depicted in Fig. 4.3.6.

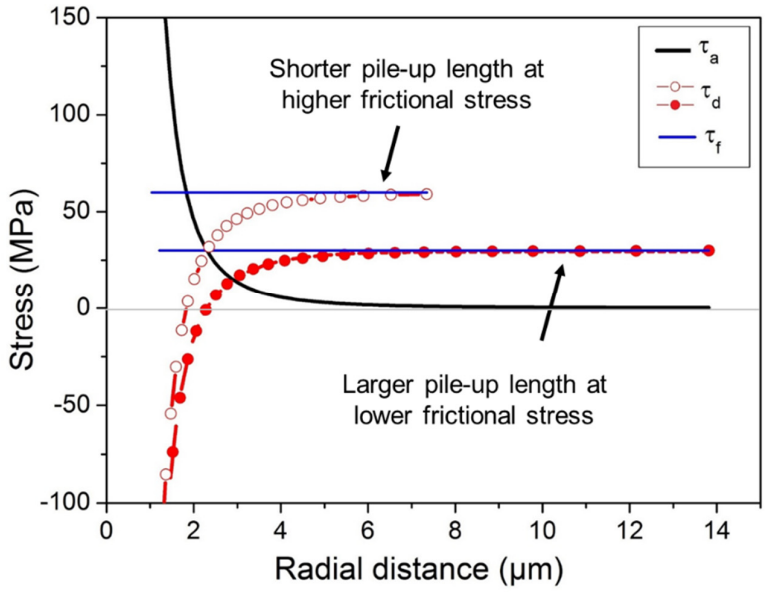

Fig. 4.3.6: The influence of frictional stress on dislocation pile-up under the equilibrium condition

Moreover, the spacing between the consecutive outermost dislocations was found larger at τ_{f1} = 30 MPa as compared to τ_{f2} = 60 MPa. For better visualization, a graph between consecutive dislocations spacing (Δr) and radial distance (r) is shown in Fig. 4.3.7.

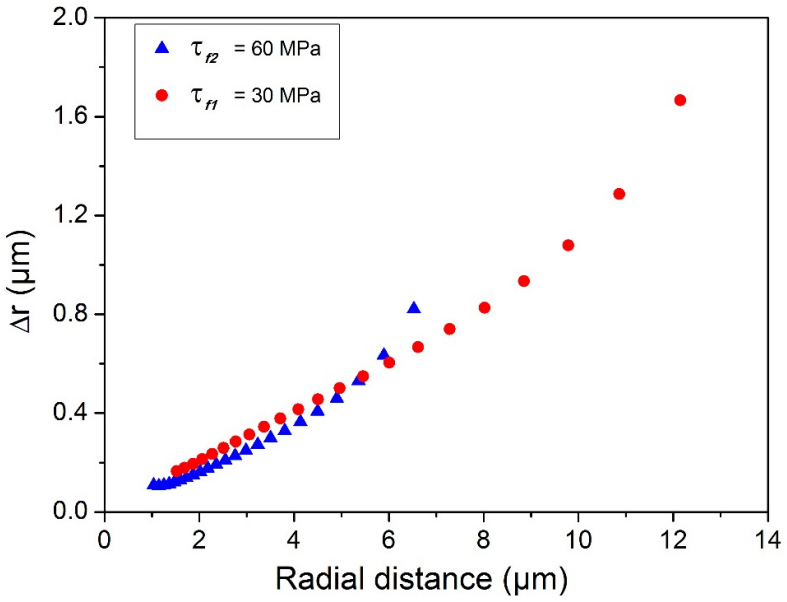

Fig. 4.3.7: The influence of frictional stress on dislocation pile-up and consecutive spacing of dislocations under the equilibrium conditions

Both τ_{f1} = 30 MPa and τ_{f2} = 60 MPa show a similar trend, i.e., the spacing between the consecutive dislocation increases with increase in radial distance. However, at larger radial distances (away from residual impressions), for τ_{f1} = 30 MPa, a significant increase in Δr was found for outermost dislocations as compared to τ_{f2} = 60 MPa. Fig. 4.3.6 and Fig. 4.3.7 confirm that the influence of lattice frictional stress on the dislocation pile-up predicted by the model is in good agreement with experimental observations. i.e., for indentation experiments performed at room temperature, the dislocation pile-ups were found shorter with smaller consecutive outermost dislocation spacing as compared to 350 °C indentations, which show larger dislocation pile-ups along with higher consecutive outermost dislocation spacing.

The effect of hardness on the dislocation pile-up is illustrated in Fig. 4.3.8, calculated from 24 edge dislocation equilibrium positions. At the same load level, a higher contact radius is found for the lower hardness. Furthermore, for H = 12.5 GPa and H = 10 GPa, the total dislocation pile-up lengths were found to be 9.7 μm and 16.2 μm, respectively. Thus, the decrease in hardness results in larger contact radii and thereby longer pile-ups for the same number of dislocations. For 24 dislocations at H = 12.5 GPa, τ_d saturates roughly at r/a > 10. However, for H = 10 GPa, the pile-up length is shorter (r/a < 10) and τ_d is not yet fully saturated.

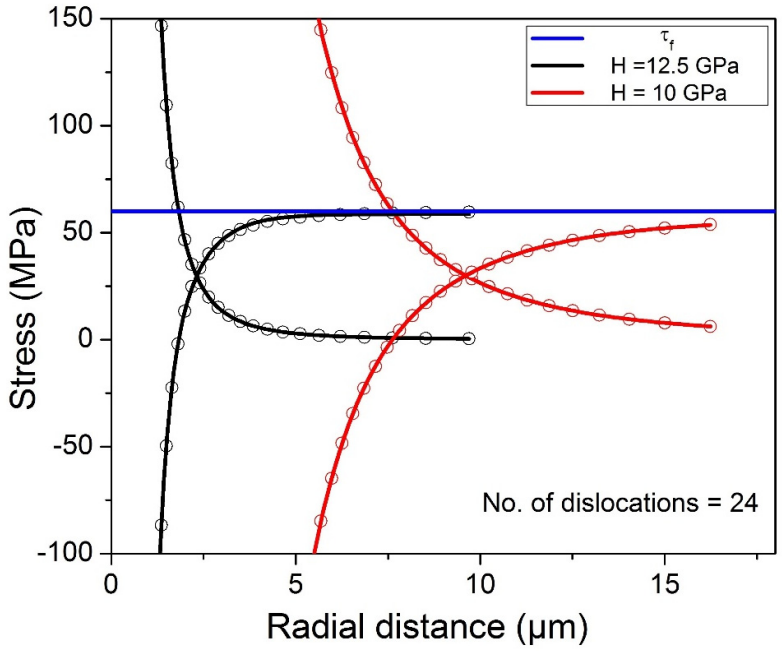

Fig. 4.3.8: The influence of hardness on dislocation pile-up under the equilibrium condition

For both H = 12.5 GPa and H = 10 GPa, the number of dislocations was increased from 24 to 60 and their influence on dislocation pile-up length is illustrated in Fig. 4.3.9.

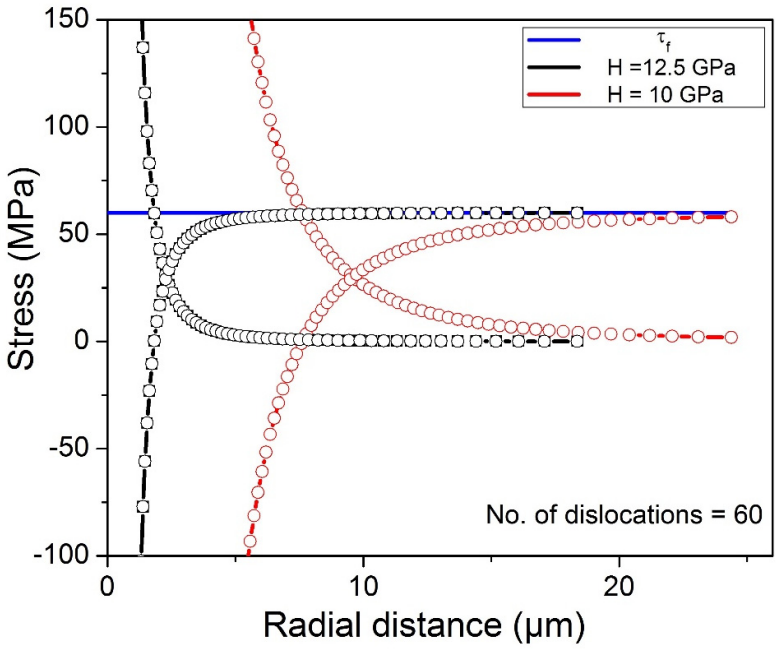

Fig. 4.3.9: The influence of hardness and number of dislocations on dislocation pile-up under the equilibrium condition

The increase in dislocations leads to increase in dislocation pile-up length from 9.7 μm to 18.3 μm and 16.2 μm to 24.4 μm for H = 12.5 GPa and H = 10 GPa, respectively. For 24 dislocations at H = 12.5 GPa, τ_d was already saturated with a very small contribution of applied stresses (0.8 MPa). The increase in number of dislocations leads to an increase in the dislocation pile-up length, which consequently reduced the contribution of applied stresses to zero at H = 12.5 GPa. Therefore, only longer pile-ups were considered for experimental analysis with a very small contribution of τ_a and a saturation in τ_d. On the other hand, at H = 10 GPa, τ_d was not saturated for 24 dislocations, however, by increasing dislocations from 24 to 60, leads to τ_d saturation at H = 10 GPa with a very small contribution of applied stresses (2 MPa).

4.3.4 Estimating Lattice Frictional Stresses from Dislocation Etch-Pit Pile-ups

Fig. 4.3.10 provides the dislocation etch-pit structure around room temperature Berkovich indentations at maximum loads of 100 mN. The center of the indent is surrounded by a region of high dislocation density from which dislocation pile-ups are emitted along the <100> or <110> directions. In order to apply the model based on the modified Hill's solution, the plastic zone is defined as the localized region of high density of dislocation etch-pits immediately surrounding the indent. For single pile-ups on <110>{110} glide systems, the

position of each etch-pit has been determined and the radial distance from the center of the indent to the etch-pit center was measured to calculate τ_d as the sum given in Eq. 2.3.2.

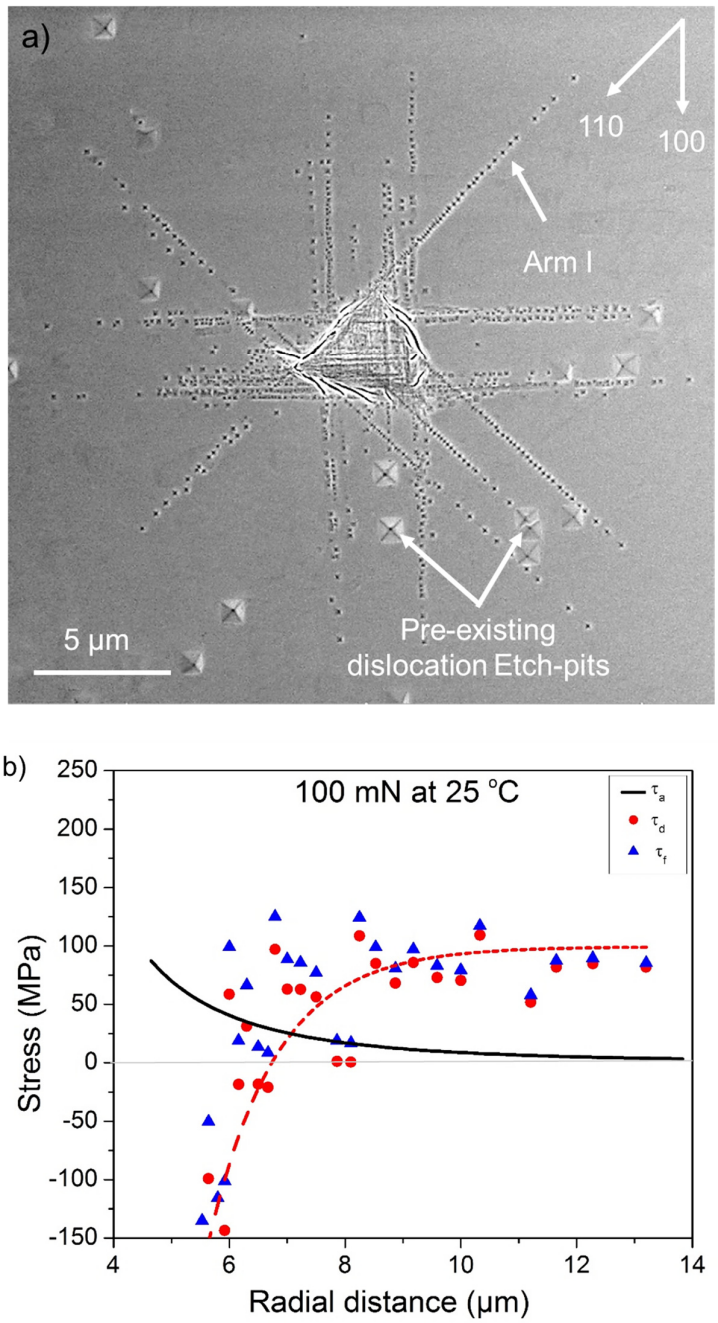

Fig. 4.3.10: (a) 100 mN etched Berkovich indentation at 25 °C, along with respective shear stress curves (b).

The resulting shear stresses from the model are shown in Fig. 4.3.10b. Considering τ_d in Fig. 4.3.10b (highlighted by a dashed red line for clarity), the stress is negative close to the dense plastic zone, but strongly increases until saturation at an approximately constant stress at large radial distances relative to contact size.

Since the stresses are negative and rapidly changing with proximity to the plastic zone, the applied stress from the indent needs to be considered for balancing the dislocation-dislocation interactions. At larger r values, where τ_d saturates, the dislocation pile-up is apparently already in equilibrium, and the lattice friction can be considered as approximately equal to τ_d.

In the model, the applied stress, τ_a, is now estimated (Eq. 4.3.1) such that in the whole pile-up region a nearly constant frictional stress is being achieved and the pile-up is thereby in equilibrium. With reference to Fig. 4.3.10b, for balancing the stresses, values of F in Eq. 4.3.1 between 0.1 to 0.2 produced consistent values of lattice frictional stresses over a wide range of loads at 25 °C for STO, independent of the hardness. At small radial distances, significant scatter in τ_f was observed as compared to large distances, attributed here to the high dislocation density region and the complex interaction of the plastic zone and dislocation pile-ups. However, the scatter in τ_f values is dramatically reduced once the pile-up is far enough away from the indent center, indicating a minute contribution of the applied stress on the dislocation spacing. Since, the Peach-Koehler forces are constant at larger distances to the plastic zone, the factor F has only provided a constant value of frictional stress close to the indent. The lattice frictional stress estimated by averaging the last 3 or 4 positions in the pile-up was insensitive to the value of F in Eq. 4.3.1 between values of 0.1 – 0.2 for all pile-ups examined in this work. For Arm I (Fig. 4.3.10a), the average lattice frictional stress was found to be 88 ± 2 MPa for edge dislocations at 25 °C. The number of dislocations for that particular arm was found to be 2.1 μm^{-1}.

Similar to the 25 °C indentations, the dislocation etch-pit arms were likewise found to be aligned along the <110> and <100> directions for 350 °C indentations. Since the loading and unloading were performed at the same temperature (350 °C), upon cooling, the increase in lattice frictional stress [22] will freeze the 350 °C indentation dislocation position at room temperature. So, the studied pile-up is the characteristic pile-up for 350 °C. To calculate the τ_f for 350 °C indentations, the sample was polished to remove ~60 nm of material from the surface in order to enhance etching conditions by eliminating possible contamination during exposure to high temperature. In Fig. 4.3.11(a), the etched image of 100 mN indentation is shown at 350 °C. The dislocation pile-ups (r/a > 5) were chosen for 350 °C frictional stress measurement. Shear stress as a function of the radial distance the dislocation pile-ups from 100 mN indentation at 350 °C is plotted in Fig. 4.3.11 (b and c) for Arm II and III, respectively.

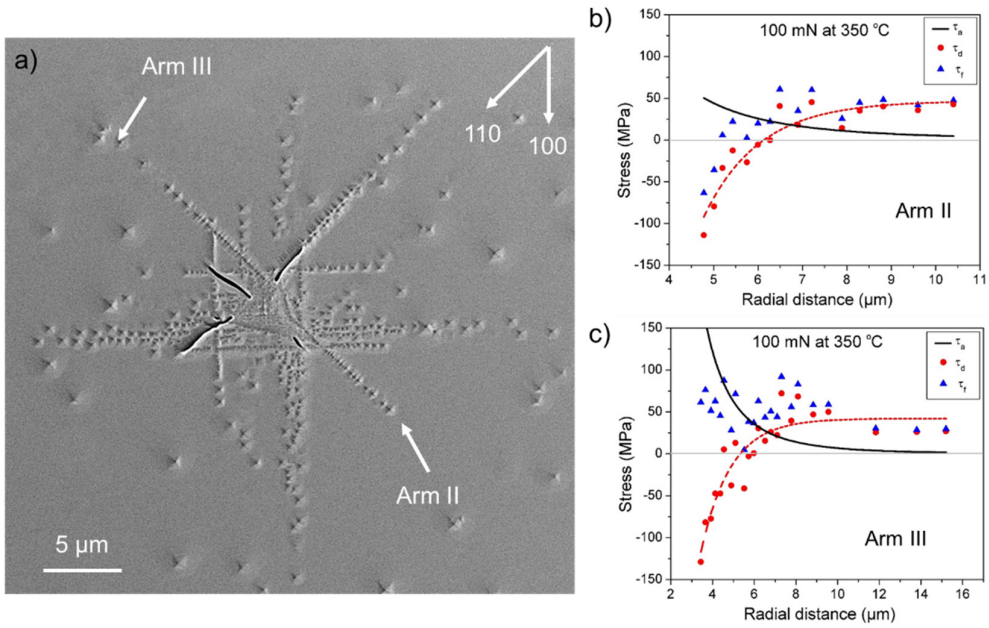

Fig. 4.3.11: (a) Etched Berkovich 100 mN indentation at 350 °C, along with respective shear stress curves for (b) Arm II and (c) Arm III.

The frictional stresses for Arm II pile-up were calculated to be 56 ± 4 MPa for edge dislocations at 350 °C. However, for Arm III pile-up, frictional stresses were found a bit lower (36 ± 5 MPa for edge dislocations) due to a larger spacing between the last few dislocation etch-pits. The number of dislocations for Arm II and Arm III was found to be 1.4 $\mu m^{-1}$and 1.5 μm^{-1}, respectively.

The frictional stress was calculated for different isolated pile-ups (r/a > 5) for 25 °C and 350 °C indentations. The average values for measured isolated dislocation pile-ups were found to be 89 ± 13 MPa and 46 ± 12 MPa for edge dislocations at 25 °C and 350 °C, respectively. The results of the frictional stress obtained from the various dislocation pile-ups at 25 °C and 350 °C were compared with uniaxial compression test data of Taeri et al. [22] and found to be in a reasonable agreement as shown in Fig. 4.3.12.

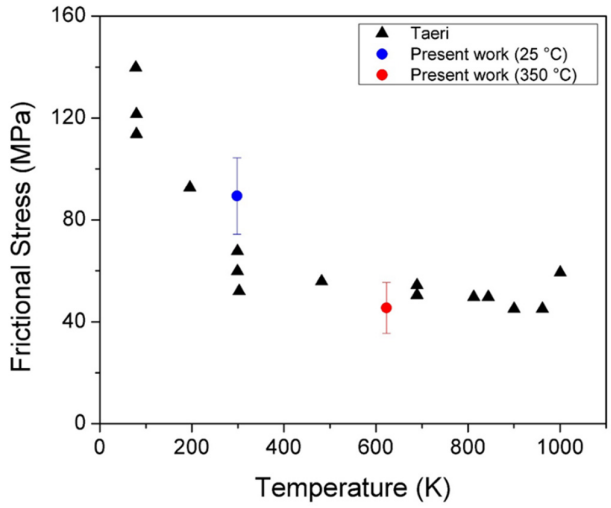

Fig. 4.3.12: Comparison of frictional stress obtained from nanoindentation (present work) and uniaxial compression test [22]

Chapter 5 Summary and Conclusions

In the present work, the 3D dislocation structure evolution (from incipient plasticity to a fully developed plastic zone) via spherical and Berkovich indentations in (001) STO single crystal was studied for the first time using a unique combination of chemical etching and HR-EBSD. The major findings obtained during room temperature spherical and Berkovich indentation experiments along with 350 °C Berkovich indentations are listed separately in each section below:

5.1 Spherical Indentations

1) For spherical indentations, at low a/R ratios, the plastic zone was found to be confined to <100> directions, just below the indentations. With an increasing a/R ratio, additional dislocation pile-ups in <110> directions evolved, which eventually lead to fully developed asterisk-shaped dislocation etch-pit patterns.
2) The cross-sections obtained from SPET at different polishing depths and indentation loads enabled us to track the evolution and three-dimensional structure of dislocation pile-ups. This analysis confirmed that, at the initial stage of plasticity <100> dislocation pile-ups evolve, lying on $\{110\}_{45}$ planes, inclined at 45° to the surface. At the later stage of plasticity, pile-ups of <110> edge dislocations on $\{110\}_{90}$ planes nucleate, which are aligned perpendicular to the surface.
3) The derived assumptions from 3D etch-pit analysis were qualitatively confirmed by corresponding direct MD simulations conducted in collaboration with the Material Modelling Division of TU Darmstadt.
4) From 3D dislocation etch-pit analysis and MD simulations, only the primary slip system $\langle 110 \rangle \{1\bar{1}0\}$ can be confirmed.
5) The pre-existing dislocations strongly influence the pop-in load and the maximum shear stress value at the initial pop-in event.

5.2 Room Temperature Berkovich Indentations

1) Along with the initial pop-in (due to the incipient plasticity), multiple pop-in events in the LD – curve were observed. Corresponding to the stochastic nature of multiple pop-in events, the dislocation etch-pit pattern was found different for same loads. These

evidences suggest that the occurrence of multiple pop-in events could be related to the nucleation and growth of pile-ups leading to hardness drops.

2) The SPET revealed a box-shaped dense region of high dislocation density from which pile-ups were emitted. At larger polishing depths, a dislocation free region surrounded by box-shaped etch-pits was observed, which stems from <100> etch-pit direction, lying on $\{110\}_{45°}$ planes.

3) For self-similar indentation to polishing depth ratio and contact radii, the ISE in STO was studied by direct evidence of the dislocations using Etch-pit and HR-EBSD analysis for polished 5 mN and 10 mN indentations. The dislocations quantified from etch-pit and HR-EBSD analysis show a similar trend in dislocation densities, i.e., higher dislocation density at lower loads. This result qualitatively validates the assumption in the Nix-Gao model that lower indentation depths result in higher GND densities. On the other hand it needs to be mentioned that the strain field and dislocation density distribution around nanoindentations are quite complex and simplified models can only partly explain the size effects.

4) The elastic strain field data was reported for the first time in STO at a local scale. The in-plane shear strain component ε_{12} shows pronounced elastic strain fields in <110> directions, which can be attributed to the pure edge character of dislocations along <110> direction.

5) The hardness – yield strength discrepancy in STO was studied using dislocation etch-pit analysis. From the known quantities, H_{fric}, G and b for STO, dislocation densities calculated via etch-pit analysis in the present work and assuming standard numbers of C and M (~ 3) for cubic materials leads to higher dislocation interaction co-efficient (α) of ~ 1. Using these values, the Taylor hardness was determined to be 13.2 GPa and 11.3 GPa for 5 mN and 10 mN indentations, respectively, which is very close to the hardness measured via the Oliver – Pharr method (i.e., 14 GPa and 12.7 GPa for 5 mN and 10 mN indentations, respectively).

5.3 High Temperature Berkovich Indentations

1) A significant decrease in ISE was observed at 350 °C compared to room temperature indentations.

2) The dense region of dislocations along with dislocation pile-ups were found to be larger for 350 °C indentations as compared to 250 °C indentations.

3) For r/a > 5, the spacing between the outermost consecutive dislocations in a pile-up for 350 °C indentations was calculated to be higher as compared to 25 °C indentations.

4) The number of dislocations per pile-up was found to be higher for 25 °C indentations as compared to 350 °C indentations.

5) Based on the residual stress field of the indenter and the dislocation-dislocation interactions in the individual dislocation pile-up, a simple model was derived to measure the lattice frictional stress at 25 °C and 350°C. For larger individual pile-ups (r/a > 5), shear stresses for outermost dislocations were found to be nearly constant and used for the estimation of the lattice frictional stress. For edge dislocations, the lattice frictional stresses calculated from the model were found to be 89 MPa and 46 MPa at 25°C and 350 °C, respectively, consistent with literature data from single-slip uniaxial compression experiments.

Chapter 6 Suggestions for Future Experimentation

The summary of future experimentations is listed below:

6.1 Tailoring Local Conductivity

As briefly mentioned in the introduction section, the dislocations in STO have gained attention due to their potential role as pathways for fast ionic or electronic transport. To study such phenomenon, a direct observation of dislocations plays a vital role. The present work shows that dislocations with a spacing of ~ 40 nm can be resolved using a chemical etching technique. Moreover, nanoindentation can be used for inducing well-aligned dislocation patterns in STO and the dislocation microstructure can be visualized at a local scale using the SPET technique. The present work also confirmed the edge and screw nature of dislocations along <110> and <100> pile-ups, respectively, which is potentially interesting for tailoring the local ionic conductivity. Fig. 6.1.1 illustrated the initial steps required for localized conductivity measurement.

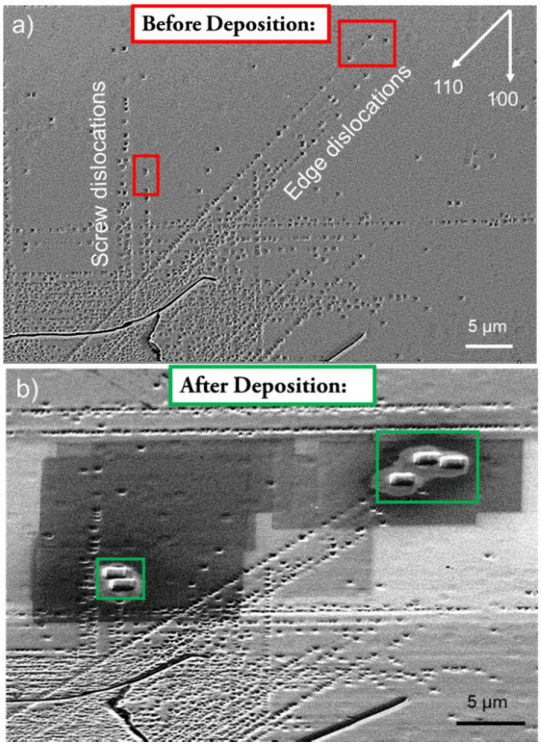

Fig. 6.1.1: Polished and etched SEM images of 100 gf Vickers indentation (a) with rectangular region showing selected <110> and <100> dislocation etch-pits before Pt deposition (b) after deposition

In this particular example, the outermost dislocation etch-pits in <110> and <100> directions depicting edge and screw dislocations, respectively, were identified (indicated by rectangles in Fig. 6.1.1a). After that Pt patches were coated on the selected etch-pits, which act as the contact points for micro-electrodes to determine the local conductivity. The SPET can also be used to obtain the desired plastic zone with few dislocation etch-pits (Fig. 4.2.7), which enabled to study the localized conductivity with limited and controlled defect structure.

6.2 Small Scale Deformation via Micro-pillar Compression

In contrast to other ceramics, STO can be plastically deformed at room temperature. To develop a better understanding of dislocations based plasticity processes at the small scale in STO, micro-pillar compression testing at different strain rates could be done, which is still missing in the literature. The micro-pillar fabrication can be conducted using FIB and in-situ nanoindentation with a flat punch indenter tip can be used for uniaxial compression testing inside an SEM. The load – displacement curves along with a direct observation of the test obtained from this in-situ approach may help to understand size effects in detail for STO. Moreover, these micro-pillar experiments combined with TEM analysis and complementary simulations can provide further insight on formation, motion, and interaction of dislocations, which play a vital role to study the small-scale deformation behavior in a material. These studies can also help in better understanding the hardness – yield strength discrepancy of STO.

References

[1] C.H. Ahn, J.M. Triscone, J. Mannhart, “Electric field effect in correlated oxide systems”, Nature, 424 (2003) 1015 – 1018.

[2] A. Tkach, O. Okhay, P.M. Vilarinho, A.L. Kholkin, “High dielectric constant and tunability of strontium titanate ceramics modified by chromium doping”, J. Phys. Cond. Matter., 20 (2008) 415224.

[3] O. Bernard, M. Andrieux, S. Poissonnet, A.M. Huntz, “Mechanical behavior of ferroelectric films on perovskite substrate”, J. Euro. Ceram. Soc., 24 (2004) 763 – 773.

[4] Q. Ma, F. Tietz, D. Sebold, D. Stöver, “Y-substituted $SrTiO_3$-YSZ composites as anode materials for solid oxide fuel cells: Interaction between SYT and YSZ”, J. of Power Sources, 195 (2010) 1920 – 1925.

[5] K.K. Adepalli, M. Kelsch, R. Merkle, J. Maier, “Enhanced ionic conductivity in polycrystalline TiO_2 by one-dimensional doping”, Phys. Chem. Chem. Phys., 16 (2014) 4942 – 4951.

[6] A. Tschöpe, E. Sommer, R. Birringer, “Grain size dependent electrical conductivity of polycrystalline cerium oxide: I. experiments”, Solid State Ionics., 139 (2001) 255 – 265.

[7] K.K. Adepalli, M. Kelsch, R. Merkle, J. Maier, “Influence of line defects on the electrical properties of single crystal TiO_2”, Adv. Func. Mater., 23 (2013) 1798 – 1806.

[8] L. Sun, D. Marrocchelli, B. Yildiz, “Edge dislocation slows down oxide ion diffusion in the doped CeO_2 by segregation of charged defects”, Nat. Comm., 6 (2015) 6294.

[9] R.A. De Souza, J. Fleig, R. Merkle, J. Maier, “$SrTiO_3$: A model electro-ceramic”, Z. Metallkd., 94 (2003) 218 – 225.

[10] V. Metlenko, A.H. Ramadan, F. Gunkel, H. Du, H. Schraknepper, S. Hoffmann-Eifert, R. Dittmann, R. Waser, R.A. De Souza, “Do dislocations act as atomic autobahns for oxygen in the perovskite oxide $SrTiO_3$?”, Nanoscale, 6 (2014) 12864 – 76.

[11] D. Marrocchelli, L. Sun, B. Yildiz, “Dislocations in $SrTiO_3$: easy to reduce but not so fast for oxygen transport”, J. Am. Chem. Soc., 137 (2015) 4735 – 4748.

[12] K. Szot, R. Dittmann, W. Speier, R. Waser, "Nanoscale resistive switching in $SrTiO_3$ thin films", Phys. Status Solidi RRL, 1 (2007) R86 – R88.

[13] R. Waser, R. Dittmann, G. Staikov, K. Szot, "Redox-based resistive switching memories – nanoionic mechanisms, prospects and challenges", Adv. Mater., 21 (2009) 2632 – 63.

[14] K. Szot, W. Speier, G. Bihlmayer, R. Waser, "Switching the electrical resistance of individual dislocations in single-crystalline $SrTiO_3$". Nat. Mater., 5 (2006) 312–320.

[15] K. Szot, W. Speier, R. Carius, U. Zastrow, W. Beyer, "Localized metallic conductivity and self-healing during thermal reduction of $SrTiO_3$". Phy. Rev. Lett., 88 (2002) 075508.

[16] F.W. Lytle, "X-ray diffractometry of low temperature phase transformations in strontium titanate", J. Appl. Phys., 35 (1964) 2212 – 2215.

[17] E. K. H. Salje, M. C. Gallardo, J. Jiménez, F. J. Romero, J. Del Cerro, "The cubic-tetragonal phase transition in $SrTiO_3$: excess specific heat measurements and evidence for a near tri-critical, mean-field type transition mechanism", J. Phys. Condens. Matter., 10 (1998) 5535 – 43.

[18] D. Brunner, S. Taeri, W. Sigle, M. Rühle, "Surprising results of a study on the plasticity in $SrTiO_3$", J. Am. Ceram. Soc., 84 (2001) 1161 – 63.

[19] P. Gumbsch, S. Taeri, D. Brunner, W. Sigle, M. Rühle, "Plasticity and an inverse Brittle-to-Ductile Transition in strontium titanate", Phys. Rev. Lett., 87 (2001) 085505.

[20] D. Brunner, "Low-temperature plasticity and flow-stress behavior of strontium titanate single crystal", Acta Mater., 54 (2006) 4999 – 5011.

[21] Kai-Hsun Yang, New-Jin Ho, Hong-Yang Lu, "Plastic deformation of (001) single crystal $SrTiO_3$ by compression at room temperature", J. Am. Ceram. Soc., 94 (2011) 3104 – 3111.

[22] S. Taeri, D. Brunner, W. Sigle, M. Rühle, "Deformation behavior of $SrTiO_3$ between room temperature and 1800 K under ambient pressure", Z. Metallkd., 95 (2004) 433 – 446.

[23] E.A. Patterson, M. Major, W. Donner, K. Durst, K.G. Webber, J. Rödel, "Temperature-dependent deformation and dislocation density in $SrTiO_3$ (001) Single Crystals", J. Am. Ceram. Soc., 99 (2016) 3411 – 3420.

[24] T. Matsunaga, H. Saka, "Transmission electron microscopy of dislocations in $SrTiO_3$", Phil. Mag., 80 (2000) 597 – 604.

[25] Kai-Hsun Yang, New-Jin Ho, Hong-Yang Lu, “Deformation microstructure in (001) single crystal strontium titanate by Vickers indentation”, J. Am. Ceram. Soc., 92 (2009) 2345 – 2353.

[26] S. Kondo, N. Shibata, T. Mitsuma, E. Tochigi, Y. Ikuhara, “Dynamic observations of dislocation behavior in $SrTiO_3$ by in-situ nanoindentation in a transmission electron microscope”, Appl. Phys. Lett., 100 (2012) 181906.

[27] P. Sadrabadi, K. Durst, M. Göken, “Study on the indentation size effect in CaF_2: Dislocation structure and hardness”, Acta Mater., 57 (2009) 1281 – 1289.

[28] A.A. Zbib, D.F. Bahr, “Dislocation nucleation and source activation during nanoindentation yield points”, Metall. Mater. Trans A, 38 (2007) 2249 – 2255.

[29] A. Montagne, V. Audurier, C. Tromas, “Influence of pre-existing dislocations on the pop-in phenomenon during nanoindentation in MgO”, Acta Mater., 61 (2013) 4778 – 4786.

[30] R.J. Kamaladasa, W. Jiang, Y.N. Picard, “Imaging dislocations in single crystal $SrTiO_3$ substrates by electron channeling”, J. Elec. Mater., 40 (2011) 2222.

[31] G. Naresh-Kumar, B. Hourahine, P.R. Edwards, A.P. Day, A. Winkelmann, A.J. Wilkinson, P.J. Parbrook, C. T. Cowan, “Rapid nondestructive analysis of threading dislocations in Wurtzite materials using the scanning electron microscope”, Phy. Rev. Lett., 108 (2012) 135503.

[32] J. I. Zhang, S. Zaefferer, D. Raabe, “A study on the geometry of dislocation patterns in the surrounding of nanoindents in a TWIP steel using electron channeling contrast imaging and discrete dislocation dynamics simulations”, Mater. Sc. Eng. A, 636 (2015) 231−242.

[33] D. Kiener, R. Pippan, C. Motz, H. Kreuzer, “Microstructural evolution of the deformed volume beneath microindents in tungsten and copper”, Acta Mater., 54 (2006) 2801−2811.

[34] E. Demir, D. Raabe, N. Zaafarani, S. Zaefferer, “Investigation of the indentation size effect through the measurement of the geometrically necessary dislocations beneath small indents of different depths using EBSD tomography”, Acta Mater., 57 (2009) 559−569.

[35] W.D. Nix, H. Gao, “Indentation size effect in crystalline materials: A law for strain gradient plasticity”, J. Mech. Phys. sol., 46 (1998) 411 – 425.

[36] D. Kiener, K. Durst, M. Rester, A. M. Minor, "Revealing deformation mechanisms with nanoindentation," *JOM*, 61 (2009) 14 – 23.

[37] X. G. Qiao, M. J, Starink, N. Gao, "The influence of indenter tip rounding on the indentation size effect," *Acta Mater.*, 58, (2010) 3690 – 3700.

[38] A.J. Wilkinson, G. Meaden, D.J. Dingley, "High-resolution elastic strain measurement from electron backscatter diffraction patterns: New levels of sensitivity", Ultramicroscopy, 106 (2006) 307−313.

[39] A.J. Wilkinson, G. Meaden, D.J. Dingley, "High resolution mapping of strains and rotations using electron backscatter diffraction", Mater. Sci. and Tech., 22 (2006) 1271 – 1278.

[40] B. Britton, I. Holton, G. Meadon, D. Dingley, "High angular resolution electron backscatter diffraction: measurement of strain in functional and structural materials", Microscopy and Analysis, 27 (2013) 8 – 13.

[41] M.S.J. Marshall, A.E. Toledo, L.D. Marks, M.R. Castell, "Defects on strontium titanate", Springer series in surface sciences, 58 (2015) 327 – 349.

[42] T. Leisegang, H. Stöcker, A.A. Levin, T. Weißbach, M. Zschornak, E. Gutmann, K. Rickers, S. Gemming, D.C. Meyer, "Switching Ti valence in $SrTiO_3$ by a dc Electric field", Phys. Rev. Lett., 102 (2009) 087601.

[43] R.D. Leapman, L.A. Grunes, P.L. Fejes, "Study of L_{23} edges in the 3d transition metals and their oxides by electron-energy-loss spectroscopy with comparisons to theory", Phys. Rev. B, 26 (1982) 614 – 635.

[44] W.C. Oliver, G.M. Pharr, "An improved technique for determining hardness and elastic modulus using load and displacement sensing indentation experiments", J. Mater. Res., 7 (1992) 1564 – 1583.

[45] I.N. Sneddon, "The relation between load and penetration in the axisymmetric boussinesq problem for a punch of arbitrary profile", Inter. J. Eng. Sci., 3 (1965) 47 – 57.

[46] J. Hay, "Introduction to instrumented indentation testing", Experimental Techniques, 33 (2009) 66 – 72.

[47] C. Tromas, J. Colin, C. Coupeau, J.C. Girard, J. Woirgard and J. Grilhé, "Pop-in phenomenon during nanoindentation in MgO", The European Physical J. Appl. phys., 8 (1999) 123 – 128.

[48] T.T. Zhu, A.J. Bushby, D.J. Dunstan, "Size effects in initiation of plasticity for ceramics in Nanoindentation", J. Mech. and Phys. of Solids, 56 (2008) 1170 – 1185.

[49] D. Lorenz, A. Zeckzer, U. Hilpert, P. Grau, H. Johansen, H.S. Leipner, "Pop-in effect as homogeneous nucleation of dislocations during Nanoindentation", Phys. Rev. B, 67 (2003) 172101.

[50] M. Göken, M. Kempf, "Pop-ins in nanoindentations – the initial yield point", Zeitschrift für Metallkunde, 92 (2001) 1061 – 1067.

[51] C.L. Kelchner, S.J. Plimpton, J.C. Hamilton, "Dislocation nucleation and defect structure during surface indentation" Phys. Rev., B 58 (1998) 11085.

[52] H. Hertz, Hertz's miscellaneous papers; Ch. 5 and 6., Macmillan, London, U.K., 1896.

[53] M. Göken, M. Kempf, "Microstructural properties of super-alloys investigated by nanoindentations in an atomic force microscope", Acta. Mater., 47 (1999) 1043 – 1052.

[54] S. Shim, H. Bei, E.P. George, G.M. Pharr, "A different type of indentation size effect", Scr. Mater., 59 (2008) 1095 – 1098.

[55] M.A. Lodes, A. Hartmaier, M. Göken, K. Durst, "Influence of dislocation density on pop-in behavior and indentation size effect in CaF_2 single crystal: Experiments and molecular dynamics simulations", Acta Mater., 59 (2011) 4264 – 4273.

[56] P.S. Phani, K.E. Johanns, G. Duscher, A. Gali, E.P. George, G.M. Pharr, "Scanning transmission electron microscope observations of defects in as-grown and pre-strained Mo alloy fiber", Acta Mater., 59 (2011) 2172 – 2179.

[57] H. Bei, S. Shim, G.M. Pharr, E.P. George, "Effects of pre-strain on the compressive stress-strain response of Mo-alloy single crystal micro-pillars", Acta Mater., 56 (2008) 4762 – 4770.

[58] M.G. Wang, A.H.W. Ngan, "Indentation strain burst induced by grain boundaries in niobium", J. Mater. Res., 19 (2004) 2478 – 2486.

[59] J. E. Bradby, S. O. Kucheyev, J. S. Williams, J. Wong-Leung, M. V. Swain, P. Munroe, G. Li, M. R. Phillips, "Indentation induced damage in GaN epilayers", Appl. Phys. Lett., 80 (2002) 383 – 85.

[60] N. Rosa-Fox, V.M. Flórez, J.A.T. Fernández, M. Piñero, R.M. Serna, L. Esquivias, "Nanoindentation on hybrid organic / inorganic silica aerogels", J. Euro. Ceram. Soc., 27 (2007) 3311 – 3316.

[61] L. Chang, L. Zhang, "Mechanical behavior characterization of silicon and effect of loading rate on pop-in: A nanoindentation study under ultra-low loads", Mater. Sc. Eng. A, 506 (2009) 125 – 129.

[62] T.H. Ahn, C.S. Oh, D.H. Kim, K.H. Oh, H. Bei, E.P. George, H.N. Han, "Investigation of strain-induced martensitic transformation in metastable austenite using Nanoindentation", Scr. Mater., 63 (2010) 540 – 543.

[63] T.B. Britton, D. Randman, A.J. Wilkinson, "Nanoindentation study of slip transfer phenomenon at grain boundaries", J. Mater. Res., 24 (2009) 607 – 615.

[64] E.C. Packard, C.A. Schuh, "Initiation of shear bands near a stress concentration in metallic glass", Acta Mater., 55 (2007) 5348 – 5358.

[65] N.K. Mukhopadhyay, P. Paufler, "Micro and nanoindentation techniques for mechanical characterization of materials", Int. Mater. Rev., 51 (2006) 209 – 45.

[66] G.M. Pharr, E.G. Herbert, Y. Gao, "The indentation size effect: A critical examination of experimental observations and mechanistic interpretations", Annu. Rev. Mater., Res., 40 (2010) 271 – 292.

[67] K.W. McElhaney, J.J. Vlassak, W.D. Nix, "Determination of indenter tip geometry and indentation contact area for depth-sensing indentation experiments", J. Mater. Res., 13 (1998) 1300 – 1306.

[68] Y. Liu, A.H.W. Ngan, "Depth dependence of hardness in copper single crystals measured by nanoindentation", Scr. Mater., 44 (2001) 237 – 241.

[69] J.G. Swadener, E.P. George, G.M. Pharr, "The correlation of the indentation size effect measured with indenters of various shapes", J. Mech. Phys. Solids, 50 (2002) 681 – 94.

[70] Y. Huang, S. Qu, K.C. Hwang, M. Li, H. Gao, “A conventional theory of mechanism-based strain gradient plasticity”, Int. J. Plast., 20 (2004) 753–782.

[71] S. Qu, Y. Huang, G.M. Pharr, K.C. Hwang, “The indentation size effect in spherical indentation of iridium: a study via conventional theory of mechanism-based strain gradient plasticity”, Int. J. Plast., 22 (2006) 1265–1286.

[72] Y. Huang, F. Zhang, K.C. Hwang, W.D. Nix, G.M. Pharr, G. Feng, “A model for size effects in nanoindentation”, J. Mech. Phys. Solids, 54 (2006) 1668 – 1686.

[73] D. Tabor, “The hardness of metals”, Oxford, UK: Clarendon Press (1951).

[74] G. Feng, W.D. Nix, “Indentation size effect in MgO”, Scr. Mater., 51 (2004) 599 – 603.

[75] K. Durst, B. Backes, M. Göken, “Indentation size effect in metallic materials: Correcting for the size of the plastic zone”, Scr. Mater., 52 (2005)1093 – 1097.

[76] K. Durst, O. Franke, A. Böhner, M. Göken, “Indentation size effect in Ni–Fe solid solutions”, Acta Mater., 55 (2007) 6825 – 6833.

[77] K. Durst, M. Göken, G.M. Pharr, “Indentation size effect in spherical and pyramidal indentations”, J. Phy. D: Appl. Phys., 41 (2008) 074005.

[78] K. Durst, B. Backes, O. Franke, M. Göken, “Indentation size effect in metallic materials: modelling strength from pop-in to macroscopic hardness using geometrically necessary dislocations”, Acta Mater., 54 (2006) 2457 – 2555.

[79] G.M. Pharr, J.H. Strader, W.C. Oliver, “Critical issues in making small-depth mechanical property measurement by nanoindentation with continuous stiffness measurement”, J. Mater. Res., 24 (2009) 653 – 666.

[80] O. Franke, J.C. Trenkle, C.A. Schuh, “Temperature dependence of the indentation size effect”, J. Mater. Res., 25 (2010) 1225 – 1229.

[81] X. Kong, F. Sun, M. Yang, “The indentation size effect in SnAGCu lead-free BGS solder joints at elevated temperature”, 16th Int. Conf. Elect. Pack. Tech., (2015) 1207– 1210.

[82] S.W. Lee, L. Meza, J. R. Greer, “Cryogenic nanoindentation size effect in [001] oriented face-centred cubic and body-centred cubic single crystals”, Appl. Phys. Lett., 103 (2013) 101906.

[83] W. Yang, B.C. Larson, G.M. Pharr, G.E. Ice, J.D. Budai, "Deformation microstructure under micro-indent in single crystal Cu using 3D X-ray structural microscopy", J. Mater. Res., 19 (2004) 66 – 72.

[84] G. Feng, A.S. Budiman, W.D. Nix, N. Tamura, J.R. Patel, "Indentation size effect in single crystal copper as revealed by synchrotron X-ray micro-diffraction", J. Appl. Phys., 104 (2008) 043501.

[85] S. Amelinckx, "The direct observation of dislocation nets in rock salt single crystal", Phil. Mag., 1 (1956) 269 – 290.

[86] J.J. Gilman, W.G. Johnston, G.W. Sears, "Dislocation etch-pit formation in lithium fluoride", J. Appl. Phys., 29 (1958) 747 – 754.

[87] S. Mendelson, "Dislocation etch-pit formation in sodium chloride", J. Appl. Phys., 32 (1961) 1571 – 1583.

[88] E.M. Nadgornyi, A.V. Stepanov, Fiz. Tverd. Tela, 5 (1963) 998.

[89] K. Sangwal, "Dissolution kinetics of MgO crystals in aqueous acidic salt solutions", J. Mater. Sci., 17 (1982) 3598 – 361.

[90] A.R. Patel, J. Koshy, "Etching of synthetic barite ($BaSO_4$) single crystal", J. Appl. Cryst., 1 (1968) 172 – 175.

[91] L. Lu, Z.Y. Gao, B. Shen, F.J. Xu, S. Huang, Z.L. Miao, Y. Hao, Z.J. Yang, G.Y. Zhang, X.P. Zhang, J. Xu, D.P. Yu, "Microstructure and origin of dislocation etch-pits in GaN epilayers grown by metal organic chemical vapor deposition", J. Appl. Phys., 104 (2008) 123525.

[92] M. M. Chaudhri, "Dislocations and Indentations"; pp. 447–550 in Dislocations in Solids, Vol. 12, Ch. 70, Edited by F. R. N. Nabarro and J. P. Hirth., Elsevier, Netherland, 2004.

[93] Y. Gaillard, C. Tromas, J. Woirgard, "Quantitative analysis of dislocation pile-ups nucleated during nanoindentation in MgO", Acta Mater., 54, (2006) 1409 – 1417.

[94] J. Weertman, J.R. Weertman, ''Elementary dislocation theory', Oxford University Press, (1992) 127.

[95] M.T. Hanson, T. Johnson, “The elastic field for spherical Hertzian contact of isotropic bodies revisited: some alternative expressions”, J. Tribol., 115 (1993) 327 – 332.

[96] S. Nishikawa, S. Kikuchi, “The diffraction of cathode rays by calcite”, Proc. Imp. Acad., 4 (1928) 475−477.

[97] N.C.K. Lassen, D.J. Jensen, K. Conradsen, “Image processing procedures for analysis of electron back scattering patterns”, Scanning Microscopy, 6 (1992) 115−121.

[98] P.V.C. Hough, US patent 3069654 (1962).

[99] G. Nolze, “Image distortion in SEM and their influences on EBSD measurements”, Ultramicroscopy, 107 (2007) 172−183.

[100] http://www.ebsd.com/ebsd-explained/basics-of-automated-indexing (Last visited on 2nd February 2017).

[101] N. Zaafarani, D. Raabe, R.N. Sigh, F. Roster, S. Zaefferer, “Three-dimensional investigation of texture and microstructure below a nano-indent in a Cu single crystal using 3D EBSD and crystal plasticity finite element simulations”, Acta Mater., 54 (206) 1863 – 1876.

[102] A.J. Wilkinson, E.E. Clarke, T.B. Britton, P. Littlewood, P.S. Karamched, “High-resolution electron backscatter diffraction: An emerging tool for studying the local deformation”, J. Strain Analysis, 45 (2010) 365 – 376.

[103] F.J. Humphreys, “Review – grain and sub-grain characterization by electron backscatter diffraction”, J. Mater. Sc., 36 (2001) 3833 – 3854.

[104] S. Villert, C. Maurice, C. Wyon, R. Fortunier, “Accuracy assessment of elastic strain measurements by EBSD”, J. Microscopy, 233 (2009) 290 – 301.

[105] M.D. Vaudin, Y.B. Gerbig, S.J. Stranick, R.F. Cook, “Comparison of nanoscale measurements of strain and stress using electron back scattered diffraction and confocal Raman microscopy”, Appl. Phys. Lett., 93 (2008) 193116.

[106] T.B. Britton, H. Liang, F.P.E. Dunne, A.J. Wilkinson, “The effect of crystal orientation on the indentation response of commercially pure titanium: experiments and simulations”, Proc. R. Soc. A, 466 (2010) 695 – 719.

[107] A.J. Wilkinson, D. Randman, “Determination of elastic strain fields and geometrically necessary dislocation distributions near nano-indents using electron backscatter diffraction”, Phil. Mag., 90 (2010) 1159 – 1177.

[108] D. He, J.C. Zhu, Z.H. Lai, Y. Lium X.W. Yang, Z.S. Nong, “Residual elastic stress-strain field and geometrically necessary dislocation density distribution around nanoindentation in TA15 titanium alloy”, Trans. Nonferrous Met. Soc. China, 23 (2013) 7 – 13.

[109] M.D. Vaudin, G. Stan, Y.B. Gerbig, R.F. Cook, “High resolution surface morphology measurements using EBSD cross-correlation techniques and AFM”, Ultramicroscopy, 111 (2011) 1206−1213.

[110] Z. Zhang, W. Sigle, W. Kurtz, M. Rühle, “Electronic and atomic structure of a dissociated dislocation in $SrTiO_3$”, Phys. Rev. B, 66 (2002) 214112.

[111] M. Castillo-Rodríguez, W. Sigle, “Dislocation dissociation and stacking-fault energy calculation in strontium titanate”, Scr. Mater. 62, (2010) 270 – 273.

[112] Z. Mao, K. Knowles, “Dissociation of lattice dislocations in $SrTiO_3$”, Phil. Mag. A, 73 (1996) 699 – 708.

[113] D. Ferré, P. Carrez, P. Cordier, “Modeling dislocation cores in $SrTiO_3$ using the Peierls-Nabarro model”, Phys. Rev. B, 77 (2008) 014106.

[114] P. Hirel, P. Marton, M. Mroves, C. Elsässer, “Theoretical investigation of {1 1 0} generalized stacking faults and their relation to dislocation behavior in perovskite oxides”, Acta Mater., 58 (2010) 6072 – 6079.

[115] P. Hirel, M. Mrovec, C. Elsässer, “Atomistic simulation study of <110> dislocations in strontium titanate”, Acta Mater., 60 (2012) 329 – 338.

[116] J. Nishigaki, K. Kuroda, H. Saka, “Electron microscopy of dislocation structures in $SrTiO_3$ deformed at High Temperature”, Phys. Stat. Sol., 128 (1991) 319 – 336.

[117] G.R. Anstis, P. Chantikul, B.R. Lawn, D.B. Marshall, “A critical evaluation of indentation techniques for measuring fracture toughness: I, direct crack measurement”, J. Am. Ceram. Soc., 64 (1981) 533 – 538.

[118] S. Plimpton, “Fast Parallel Algorithms for Short-Range Molecular Dynamics”, J. Comput. Phys. 117 (1995) 1–19.

[119] A. Stukowski, “Visualization and analysis of atomistic simulation data with OVITO–the Open Visualization Tool”, Model. Simul. Mater. Sci. Eng., 18 (2010) 015012.

[120] Stukowski A. “Structure identification methods for atomistic simulations of crystalline materials”, Model Simul. Mater. Sci. Eng., 20 (2012) 1 – 15.

[121] A. Stukowski, K. Albe, “Extracting dislocations and non-dislocation crystal defects from atomistic simulation data”, Model. Simul. Mater. Sci. Eng., 18 (2010) 1 – 13.

[122] A. Stukowski, V. V. Bulatov, A. Arsenlis, “Automated identification and indexing of dislocations in crystal interfaces”, Model. Simul. Mater. Sci. Eng. 20 (2012) 085007.

[123] J.E. Hilliard, Stereology: An experimental viewpoint, Adv. Appl. Probab. 4 (1972) 92–111

[124] C. Maurice, R. Quey, R. Fortunier, J.H. Driver, High-angular resolution EBSD and its materials applications, in: D.A. Molodov, Microstructural design of advanced engineering materials, Wiley-VCH Verlag GmbH & Co., Germany, 2013, pp. 356–59.

[125] R. Hill, “The Mathematical Theory of Plasticity”, Clarendon Press Oxford, (1950) 97 – 105.

[126] R.O. Bell, G. Rupprecht, “Elastic constants of strontium titanate”, Phys. Rev., 129, (1963) 90 – 94.

Publications

Paper A:

Farhan Javaid, Alexander Stukowski and Karsten Durst

3D Dislocation Structure Evolution in Strontium Titanate: Spherical Indentation Experiments and MD Simulations

J. Am. Ceram. Soc., 100 (2017) 1134 – 1145, (DOI: 10.1111/jace.14626)

Paper B:

Farhan Javaid, Enrico Bruder and Karsten Durst

Indentation Size Effect and Dislocation Structure Evolution in (001) oriented $SrTiO_3$ Berkovich Indentations: HR-EBSD and Etch-pit Analysis

Acta. Mater., 139 (2017) 1 – 10, (DOI: 10.1016/j.actamat.2017.07.055)

Paper C:

Farhan Javaid, Kurt E. Johanns, Eric A. Patterson and Karsten Durst

Temperature Dependence of Indentation Size Effect, Dislocation Pile-ups and Lattice Friction in Single Crystalline Strontium Titanate

J. Am. Ceram. Soc., (2017) In Press (DOI: 10.1111/jace.15182)

Curriculum Vitae

Personal	
Name	Farhan Javaid
Place of Birth	Lahore, Pakistan

University Education:	
2002 – 2006	**B.Sc. – hons.,** Metallurgical and Materials Engineering, UET Lahore, Pakistan. *Thesis: Origin of longitudinal cracking in continuously cast billets.*
2007 – 2009	**M.Sc. –hons.,** Materials and Surface Engineering, NUST, Islamabad, Pakistan. *Thesis: Processing and characterization of Lead Zirconate Titanate (PZT) thin films via Sol-Gel Processing.*
10 / 2012 – 09 / 2013	**Ph.D.,** Materials Science and Engineering, Institute I: General Materials Properties (WW1), FAU Erlangen – Nürenberg, Germany. *Thesis: Indentation size effect: Analysis of underlying mechanisms using EBSD and TEM analysis.*
10 / 2013 – Present	**Ph.D.,** Materials Science and Engineering, Department of Physical Metallurgy (PhM), TU Darmstadt, Germany. *Thesis: Indentation size effect: Analysis of underlying mechanisms in (001) oriented strontium titanate single crystal via chemical Etching and EBSD.*

Work Experience	
01 / 2010 – 01 / 2012	**Lecturer** School of Chemical and Materials Engineering (SCME), National University of Science & Technology (NUST), Islamabad, Pakistan.